CLEARANCE OF CAPILLARY OCCLUSIONS IMPROVES CORTICAL BLOOD FLOW AND COGNITIVE FUNCTION IN ALZHEIMER'S MOUSE MODELS

A Dissertation

Presented to the Faculty of the Graduate School

of Cornell University

In Partial Fulfillment of the Requirements for the Degree of

Doctor of Philosophy

by

Jean Carlos Cruz Hernández

June 2017

CLEARANCE OF CAPILLARY OCCLUSIONS IMPROVES CORTICAL BLOOD FLOW AND COGNITIVE FUNCTION IN ALZHEIMER'S MOUSE MODELS

Jean Carlos Cruz Hernández, Ph. D.

Cornell University 2017

Alzheimer disease (AD) is characterized by a loss of cognitive function caused by the dysfunction and death of neurons and other cells in the brain. This cell injury is largely due to the toxic effects of aggregates of amyloid-beta (Aβ), which accumulates into dense plaques in the brain. Research in humans and in animals suggests that brain blood flow is reduced in AD by ~30%. Although it likely contributes to cognitive impairment and disease progression, no physiological explanation for this hypoperfusion has emerged.

In part, studies of cerebral blood flow pathology have been limited by the inability to perform *in vivo* imaging of vascular function at cellular resolution. The focus of this thesis is to present the underlying cellular mechanism responsible for this hypoperfusion phenomena and Aβ clearance in AD mouse models. Chronic cranial windows and *in vivo* two-photon excited fluorescence microscopy were used to study cerebrovascular blood flow.

While no blood flow disruption in cortical arterioles or venules were observed, blood flow was found to be stalled in an average of 1.8% of cortical capillaries in mouse

models of AD, as compared to 0.25% in wild type controls. These capillary stalls appeared early in disease progression, before any amyloid deposition. We found that the majority of the occlusions were caused by leukocytes, which adhered tightly to the endothelium. Indeed, blocking neutrophil adhesion in AD mouse models led to the fraction of capillary stalls decrease by 70 %, causing brain blood flow to increase by ~30% and cognitive function to improve.

These data suggest a working model to explain the origin of hypoperfusion in AD: Aβ accumulation leads to increased production of ROS that stresses endothelial cells and leads to increases in inflammatory receptors on the vessel lumen. This vascular inflammation causes leukocytes to adhere and plug capillaries, resulting in decreases in perfusion. This blood flow deficit could contribute to dementia independently of the direct effects of Aβ and could also accelerate Aβ aggregation by decreasing clearance of Aβ monomers.

This research provides for the first time an explanation for the long known phenomenon of reduced blood flow in Alzheimer's disease, one which has an early and significant impact on the development of pathological phenotypes. Brief reviews of multi-photon microscopy (MPM) and Brain blood flow in AD are also presented.

BIOGRAPHICAL SKETCH

Jean Carlos Cruz Hernández was born in Arecibo, Puerto Rico on January 23, 1989. He grew up in Utuado, Puerto Rico where he received his primary education. He graduated from Luis Muñoz Rivera High School in 2006 and was awarded the Governor General's Medal, awarded to the student in highest academic standing within the graduating class. He attends University of Puerto Rico at Mayagüez Campus (UPRM) majoring in Industrial Biotechnology. During his tenure at UPRM, he worked in the research group of Dr. Carlos Ríos Velázquez, in where he developed metagenomic libraries and performed biochemical screenings for the discovery of new antibiotics and molecules with biotechnological applications. In 2011, he graduated summa cum laude with his Hons. BSc. in Industrial Biotechnology, and was awarded the Barbara McClintock Medal, awarded to the top in the graduating class, university-wide. He came to Cornell University in August 2011, where he began his doctoral dissertation. He joined Dr. Chris B. Schaffer's laboratory where he has spent the past six years studying the cellular mechanism responsible of hypoperfusion in Alzheimer's disease using nonlinear optical methods. Having successfully passed his admission to candidacy exam, he was awarded a MS in Biomedical Engineering in Fall of 2014. After he graduates, his plans are to pursue postdoctoral research in the lab of Brian J. Bacskai in the Mass General Institute for Neurodegenerative Disease (MIND).

I dedicate this work to those who were lost along the way. To Iris Corraliza and Julia Maestre, whose losses were premature. To those family members who came to know Alzheimer's disease far too intimately: Dynnel Pérez, Ramón Andújar, and Lorna Andújar. Finally to Leinyn Hernández and to Carlos Cruz, who simply love their families.

ACKNOWLEDGMENTS

During the course of my graduate work in the Department of Biomedical Engineering I received support, encouragement, and guidance from numerous individuals, who made my success possible. My experience has been enlightening and educational, and I would like to specifically acknowledge those to whom I am indebted.

I first acknowledge my committee comprised of Dr. Chris B. Schaffer, Dr. Chris Xu and Dr. Andrew Bass. It has been an honor to work with each of them. I am extraordinarily grateful to my advisor Dr. Chris B Schaffer whom support and guidance have shaped this work and greatly impacted me as a scientist. Chris has taught me not only how to think critically (so critically, in fact, that we basically don't believe anything), but also how to write cleverly, manage failure gracefully, and see the future hopefully. His door was always open, whether it was to discuss scientific questions, manuscript revisions, or have a casual conversation while drinking exquisite whiskeys. I'm so grateful to have been a part of his group, where we did great science and enjoyed luxurious alcohol to celebrate our success.

In addition of having Chris guidance, I was fortunately enough to have Dr. Nozomi Nishimura as a second advisor and mentor. Since my first year as a PhD student, Nozomi have been an essential pillar in the SN lab. During this early stage of my PhD, Nozomi was my main mentor who though me the basics of instrumentation and the use of advanced optical imaging tools, such as multi-photon microscopy, for the study of rodent models of neurodegenerative disease. Throughout all this years Nozomi have

been always willing to teach and mentor new members of the lab, sharing her knowledge in optics and *in vivo* systems. Both of them, Chris and Nozomi have been a strong support through various challenges during my Ph.D. Special thanks for their great patience and guidance as thesis mentors and for the opportunity to work in their laboratories.

Words cannot describe the benefit I have derived as a scientist from knowing and working with Oliver Bracko (Oli). He has spent innumerable hours with me helping me designing experiments, perform analyses and write papers. His incredibly high standards and rigor both at the small and large scale have improved my work significantly. During this year, Oli has never been too busy to work through a problem with me. His dedication to students and their development is unparalleled.

Several undergraduate students were also incredibly helpful, and it was an honor to work with them throughout my time as a student. I particularly acknowledge Victorine Muse (Torie) and Calvin Kersbergen who contributed substantially to the work presented in this dissertation. I wish them all the best for their future endeavors.

I also want to thank to all members from SN lab their collaborative, friendly, fun-loving spirit. In particular to Jason S. Jones and Elizabeth Wayne (Liz) as my perfect grad school companions in good times and in bad times.... Jason is one of the most thoughtful and practical individuals I've ever met in research so far, and Liz is easily the most supportive and encouraging colleague one could imagine. With these two

brilliant, caring mentors I was able to identify my own weaknesses and strengths, make the most out of a research project that was at times confounding, and enjoy the journey during the PhD. Amanda Bares, thank you for teaching me proper english during these past 5 years, for been an altruistic colleague and class partner. Sung Ji, thank you for keeping me laughing with your comments, thinking and actions.

I am honored to have met and worked with so many brilliant thinkers and scientists during my PhD. I fully understand that this work would not have been possible without contributions from many, many people and will never forget those that helped me along that path. To my dear friend Dr. Carlos Ríos Velázquez who introduced me to science research, I am grateful for his patient training and encouragement to pursue science as a career.

Special thanks to my friends: Thong M. Cao, Jose L. Rios, Jason S. Jones and Joseph Miller, for the amazing moments and adventures shared during our PhDs. When Thong, Jose and Joe graduated or left Ithaca, I was sad for months. I understood it was time for me to leave as well because my best friends who were very close to me and would do anything for me had left Cornell. The time has come for our departure, with new adventures ahead. However I know for sure that we will meet again in the near future - Looking forward to it!

No one deserves as much praise and acknowledgement as Yashira Negron. She is an amazing person and has stood at my side through my last years in graduate school.

She provided a refreshing scenery change and helped direct my focus to aspects of life outside of science. I thank her for providing the much-needed balance in my life and providing a long-term vision of the future that does not necessarily involve work and career aspirations. I cannot wait for the next chapter in our lives to begin and am excited to share many more experiences together.

Finally, I would like to thank my family. First, my parents for providing me with the education that I needed to get to this point, the drive to pursue graduate studies, and their support, endurance, and encouragement along this long and difficult path. While I have acknowledged the following before, I must do so again: years ago while I was in high school, my mother wondered whether she would ever get me through high school successfully, since my educational interests were somewhat lacking. Throughout those unsettling years, my parents showed extraordinary patience by continually encouraging me to perform my best and not to settle for less.

TABLE OF CONTENTS

LIST OF FIGURES

LIST OF TABLES

CHAPTER 1

INTRODUCTION AND ORGANIZATION OF DISSERTATION

Introduction

Recently, reductions of volumetric blood flow have been identified as a common pathology in the majority of the dementias, including in Alzheimer's disease (AD) [1,2]. However, the exact causes of this cerebral blood flow deficit remain unclear, mainly due to the technical challenges presented in the study of cell dynamics in cerebral microvessels. Some of these challenges are the following: first, in order to study the cell dynamics in the brain microvessels during disease progression at physiological conditions it is necessary to perform the experiments *in vivo.* Also, while advances in neurovascular imaging techniques such as BOLD-fMRI, laser doppler flowmetry, and arterial spin labeling allow for measurements of homogenous global blood flow changes, quantification of flow changes in individual vessels as small as capillaries *in vivo* requires much higher spatial resolution. Two-photon excited fluorescence microscopy (2PEF) is an ideal tool to visualize changes in cerebral blood flow with cellular resolution and minimal invasiveness. By being able to observe vessel flow dynamics *in vivo* using 2PEF, we may be able to better understand the mechanisms at work behind cerebrovascular pathology in AD.

The work presented in this dissertation is focused on the cellular mechanism responsible for a new phenomena (capillary occlusions) that occurs in AD animal models and might explain the significant reduction of cerebral blood flow in AD and other dementias. The identification of this novel mechanism allowed us to manipulate the cell–cell interaction

and study the downstream effects of the occlusions in the cerebral microvessels. Our results of cerebral blood flow recovery and improvement in cognitive abilities in AD mouse models after reductions of these capillary stalls, suggest that the full elucidation of the cellular and molecular pathways that triggers this phenomena could open new window for alternative treatments in order to stop or ameliorate the progression of AD.

Organization of Dissertation

This thesis summarizes the techniques developed, results observed, and insights obtained over the last 6 years. This thesis is comprised of 10 chapters, including this introduction. The first two chapters provide background material, which provide context and serve as a reference for the rest of the thesis.

Chapter 2: This chapter takes a look at the current state of AD and cerebral blood flow (CBF) impairment, including clinical outcomes, pathogenesis and genetics and pre-clinical animal studies, with a spotlight on *in vivo* imaging and what it offers AD and vascular research.

Chapter 3: This chapter provides an introduction to multi-photon microscopy, basic experimental techniques and the achievement of optical sectioning, as well as a more detailed look at the individual processes of 2-photon excited fluorescence (2PEF), 3-photon excited fluorescence (3PEF) and second and third harmonic generation (SHG and THG, respectively).

Chapters 4-7 are formatted papers, whether they are published as of yet or whether they contain work in progress, including supplementary files and information.

Chapter 4: This chapter provides a re-formatted unpublished manuscript of our paper on

elucidation of the cellular mechanism responsible of hypoperfusion phenomena in AD. This chapter includes work on blood flow and the microvascular network of cortical region in AD, consisting of theoretical modeling, blood flow measurements, topographical mapping of the occlusion and Aβ, and the effects stalls release on CBF and cognitive behavior.

Chapter 5: This chapter provides a re-formatted published manuscript of our paper on "Cerebral Microbleeds, CSF p-Tau, and Cognitive Decline: Significance of Anatomic Distribution". This chapter includes work on how the anatomical distribution of microbleeds in the human brain affect the concentrations of CSF beta-amyloid and CSF p-tau, and longitudinal cognitive decline.

Chapter 6: This chapter provides a re-formatted published manuscript of our paper on "Use of Tethered Enzymes as a Platform Technology for Rapid Analyte Detection". This chapter includes work on the design and construction of a new diagnostic platform (biosensor), which achieve rapid and sensitive detection of neuron-specific enolase (NSE), a clinically relevant biomarker for multiple diseases ranging from acute brain injuries to lung cancer.

Chapter 7: This chapter discusses the development of a curriculum for high school science students. The curriculum centers around the concept of blood flow in the brain during normal and disease states. Two laboratory exercises are discussed which are analogous to flow in the brain. This chapter also includes an assessment of the curriculum from the students and a resulted manuscript.

Chapter 8: This chapter summarizes what has been successfully completed in the results of this thesis. It also discusses impacts in the clinical setting and future project directions

for whomever picks this project up where I must inevitably leave off.

References

1. Farkas, E. & Luiten, P. Cerebral microvascular pathology in aging and Alzheimer's disease. *Progress in Neurobiology* **64**: 575–611 (2001).
2. de la Torre, J. C. Alzheimer's disease: a neurodegenerative or a vascular disorder? Data, dogma, and dialectics. *Lancet Neurology* **3**, 184-190 (2004).

CHAPTER 2

Alzheimer's Disease: an Overview

In this chapter, we review the current outlook on Alzheimer's disease (AD) from a demographic, scientific and clinical perspective. This chapter is divided into three sections. In the first section, we review the current state of demographics of AD (prevalence and mortality). In the second section, we consider the changes in the cellular and molecular key components through the disease progression, and the different hypothesis that explains the pathogenesis and neuropathology of AD. Finally, we examine the clinical implications of the targeting these key cellular players and how the discovery of a new cellular mechanism provides a new target approach to ameliorate the disease progression.

2.1 INTRODUCTION

Alzheimer's disease (AD) is the most common cause of dementia, a neurodegenerative disease that is characterized by the decline of memory and cognitive abilities [1,2]. The pathogenesis of AD is defined by soluble cerebral amyloid-β (Aβ) accumulation and aggregation into dense senile plaques throughout the brain, as well as neurofibrillary tangle formation within axon microtubules of individual neurons, composed of hyperphosphorylated tau protein [3]. Independently these two different pathways affect the normal state of the neuron cells and triggers the cognitive disabilities in AD patients.

In addition to these main proteins abnormalities, clinical and experimental evidence strongly suggests that AD and vascular pathology are interrelated, and that reduced brain blood flow may play a significant role in exacerbation of AD. In both humans and in mouse models of AD, disease progression has been accompanied by decreased cortical blood flow (CBF) and impaired blood flow responses during functional hyperemia [4,5]. Human patients [6,7] with, as well as mouse models [8,9] of, Alzheimer's disease (AD) exhibit reductions in cortical CBF of ~20-30% early in disease development, and are therefore not due visible to accumulation of cerebral amyloid angiopathy [10]. However, the exact cause of this blood flow deficit in AD remains unclear.

One difficultly in understanding reduced CBF in AD is the ability to measure physiological flow within microvessels in the brain. While advances in neurovascular imaging techniques such as BOLD-fMRI, laser doppler flowmetry, and arterial spin label MRI allow for measurements of homogenous global blood flow changes, quantification of flow changes in individual vessels as small as capillaries *in vivo* requires much higher spatial resolution. Two-photon excited fluorescence microscopy (2PEF) is an ideal tool to visualize changes in CBF with cellular resolution and minimal invasiveness. By being able to observe vessel flow dynamics *in vivo* using 2PEF, we may be able to better understand the mechanisms at work behind cerebrovascular pathology in AD.

2.2 DEMOGRAPHICS OF ALZEIMER'S DISEASE

2.2.1 Prevalence

Longitudinal studies using the most recent census (2010) has estimated a population of

5.5 millions AD patients living in United States in 2017 [11]. Of this population 5.3 million people represent the late-onset of AD (65 and older) and approximately 200,000 individuals the younger-onset AD (under age 65), though there is greater uncertainty about the younger-onset estimate [12]. An approximation of the age distribution between the AD patients is shown in Fig.2.1. Based on this census 1 in 10 people age 65 and older (10%) developed Alzheimer's dementia, but AD begins many years before the onset of dementia. Due to the nature of the disease Alzheimer's dementia is under-diagnosed and underreported, a large portion of Americans with Alzheimer's may not know they have it. However, if AD could be accurately detected before dementia develops, the number of people reported to have AD expand to include more than just people who have been diagnosed with fully Alzheimer's dementia.

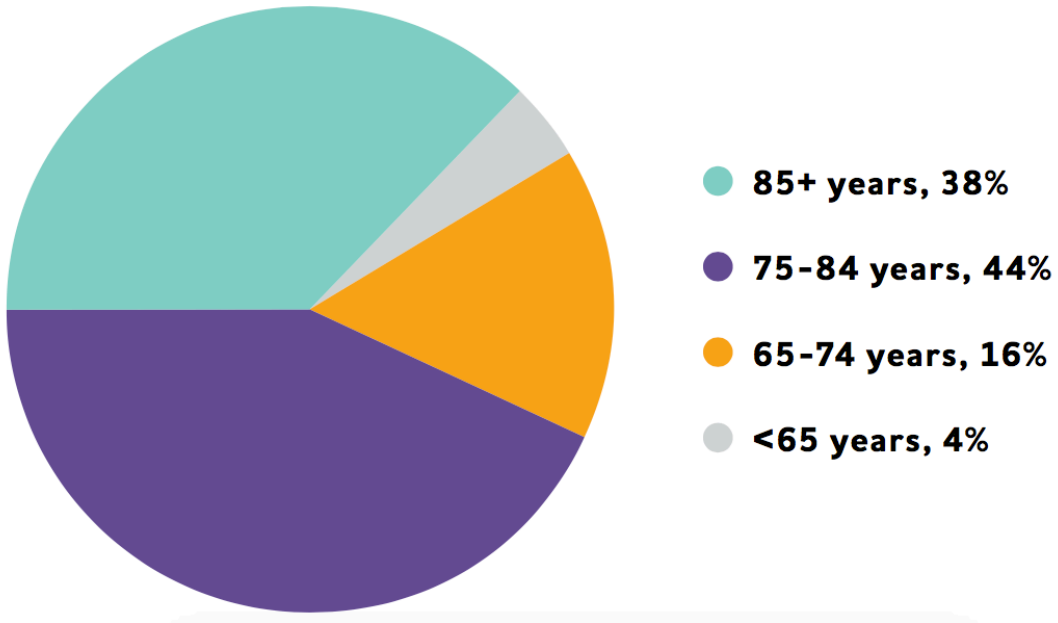

Figure 2.1 Age of People with Alzheimer's Dementia in the United States, 2017. Percentages do not total 100 because of rounding. Created from data from Hebert et al. [11]

On the other hand, due to medical advances, as well as social and environmental conditions the life expectancy is expected to grow dramatically[13]. One of the largest segments of the American population, "the baby boom generation," have begun to reach age 65 and older, in which risk for Alzheimer's is more prominent. By 2030, it is projected that 74 million Americans (65 and older) will make up over 20 % of the total population (up from 14 percent in 2012) [13]. As the number of older Americans grows rapidly, so too will the numbers of new and existing cases of Alzheimer's dementia, as shown in Fig. 2.2 [A1,11].

Based on the 2000 and 2010 census and the predictions for 2050:

- 454,000 new cases of Alzheimer's dementia were identified, just in 2010. The projection of AD population by 2030 is around 615,000 (a 35 percent increase), and by 2050, 959,000 (a 110 percent increase from 2010) [14].
- In 2017, the number of people age 65 and older with Alzheimer's dementia is 5.3 millions, and is estimated to increase 35 percent by 2025 reaching an estimated population of 7.1 million of AD patients [A2,11].
- By 2050, the number of people age 65 and older with Alzheimer's dementia may nearly triple, from 5.3 million to a projected 13.8 million, barring the development of medical breakthroughs to prevent or cure AD [A1,11]. Previous estimates based on high-range projections of population growth provided by the U.S. Census suggest that this number may be as high as 16 million [A3, 15].

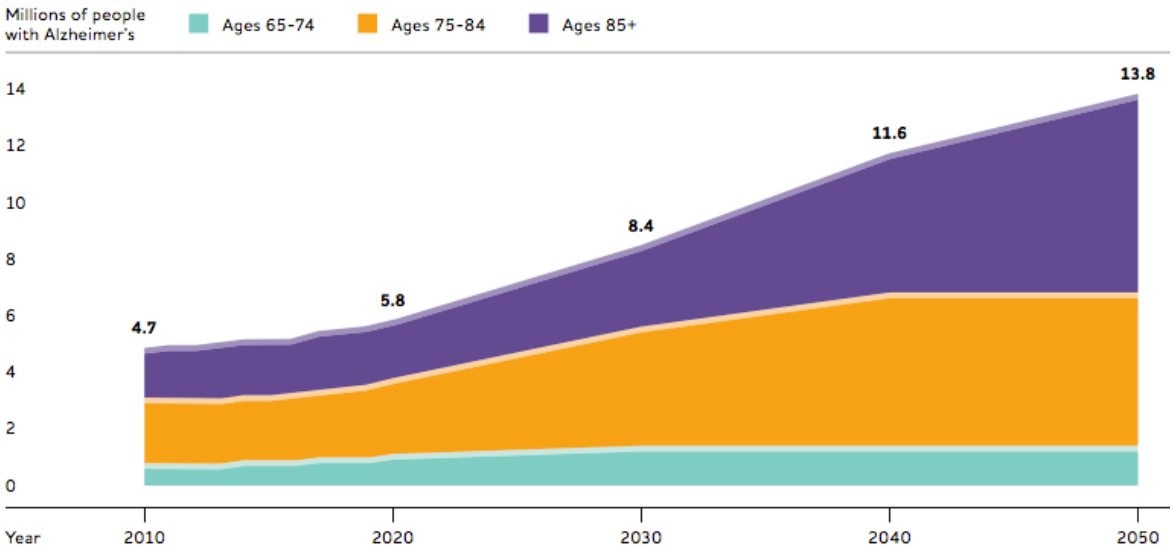

Figure 2.2 Projected Number of People Age 65 and Older (Total and by Age Group) in the U.S. Population with Alzheimer's Dementia, 2010 to 2050. Created from data from Hebert et al [11].

2.2.2 Mortality and Morbidity

As the population of the United States ages, Alzheimer's is becoming a more common cause of death, and of the top 10 leading causes of death, it is the only one that cannot be prevented, cured, or even slowed. It is difficult to determine how many deaths are caused by AD each year because of non-standardized medical documentation. AD patients who die due to these acute conditions may not be counted among the number of people who died from AD according to the World Health Organization definition, even though AD may well have caused the acute condition listed on the death certificate. Although deaths from other major causes have decreased significantly, official records indicate that deaths from AD have increased significantly [16].

Between 2000 and 2014, deaths from AD as recorded on death certificates increased 89 percent, while deaths from the number one cause of death (heart disease) decreased 14 percent (Fig. 2.3) [16]. The increase in the number of death certificates listing Alzheimer's as the underlying cause of death reflects both changes in patterns of reporting deaths on death certificates over time as well as an increase in the actual number of deaths attributable to AD.

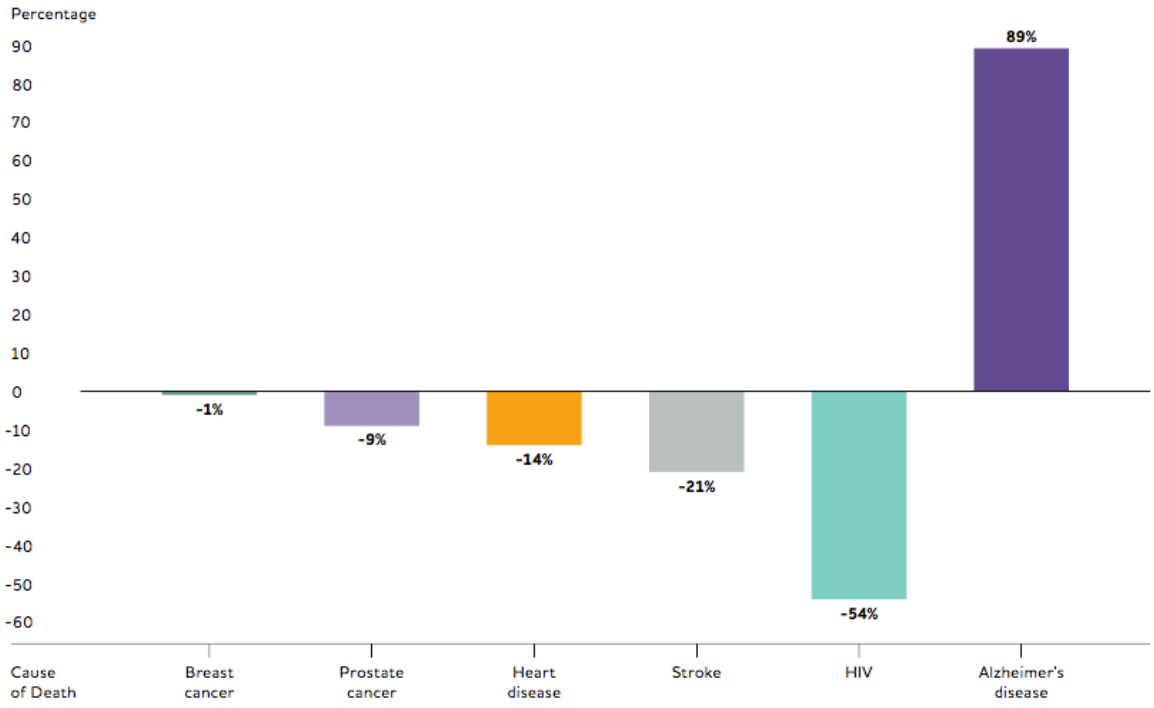

Figure 2.3 Percentages changes in selected causes of death (all ages) between 2000 and 2014. Created from data from the national center for health statistics [16].

A1. Projected number of people with Alzheimer's dementia: This figure comes from the CHAP study [11]. Other projections are somewhat lower (see, for example, Brookmeyer et al. [17]) because they relied on more conservative methods for counting people who currently have Alzheimer's dementia.

A2. Projected number of people age 65 and older with Alzheimer's dementia in 2025: The number 7.1 million is based on a linear extrapolation from the projections of prevalence of Alzheimer's for the years 2020 (5.8 million) and 2030 (8.4 million) from CHAP data [11].

A3. Previous high and low projections of Alzheimer's dementia prevalence in 2050: High and low prevalence projections for 2050 from the U.S. Census were not available for the most recent analysis of CHAP data [11]. The previous high and low projections indicate that the projected number of Americans with Alzheimer's in 2050 age 65 and older will range from 11 to 16 million [14].

2.3 PATHOGENESIS AND NEUROPATHOLOGY

2.3.1 The amyloid cascade model

The core hypothesis of the amyloid cascade model, which forms the backbone of the current understanding of the pathogenesis of AD, is that accumulation of β-amyloid is an early event leading to neuro-degeneration [18].

APP is a cell surface receptor that is expressed in many cell types, in particular in neuronal synapses, as a part of normal metabolism. Although its primary function remains unclear, amyloid precursor protein (APP) is believed to be implicated in synaptic formation and repair, signaling, and cell adhesion [19]. Several isoforms of the cleaved APP gene existing ranging in length between 365 and 770 amino acids exist, some of which appear more closely associated with the pathogenesis of AD than others [20].

As depicted in Fig. 2.4, APP is cleaved by α-secretase and beta-site amyloid precursor protein–cleaving enzyme 1 (BACE-1), a β-secretase, both of which release a soluble extracellular fragment (sAPP α and sAPP β). Cleavage by β-secretase leaves the Aβ region attached to the C-terminus fragment (α-CTF), while α-secretase cleavage takes place within the Aβ region, thereby preventing release of the full-length Aβ polypeptide. The α-CTF and β-CTF are subsequently cleaved by a ϒ-secretase in the transmembrane region releasing, respectively, either a harmless p3 fragment or the Aβ polypeptide [21].

Based on the chemical composition of the peptide the Aβ is able to self-aggregates into multiple coexisting physical forms. One form consists of oligomers (2 to 6 peptides), which coalesce into intermediate assemblies [22,23] (Fig. 2.4). Also the β-amyloid peptides can self-ensemble into fibrils, organized in β-pleated sheets to form the insoluble fibers of advanced amyloid plaques.

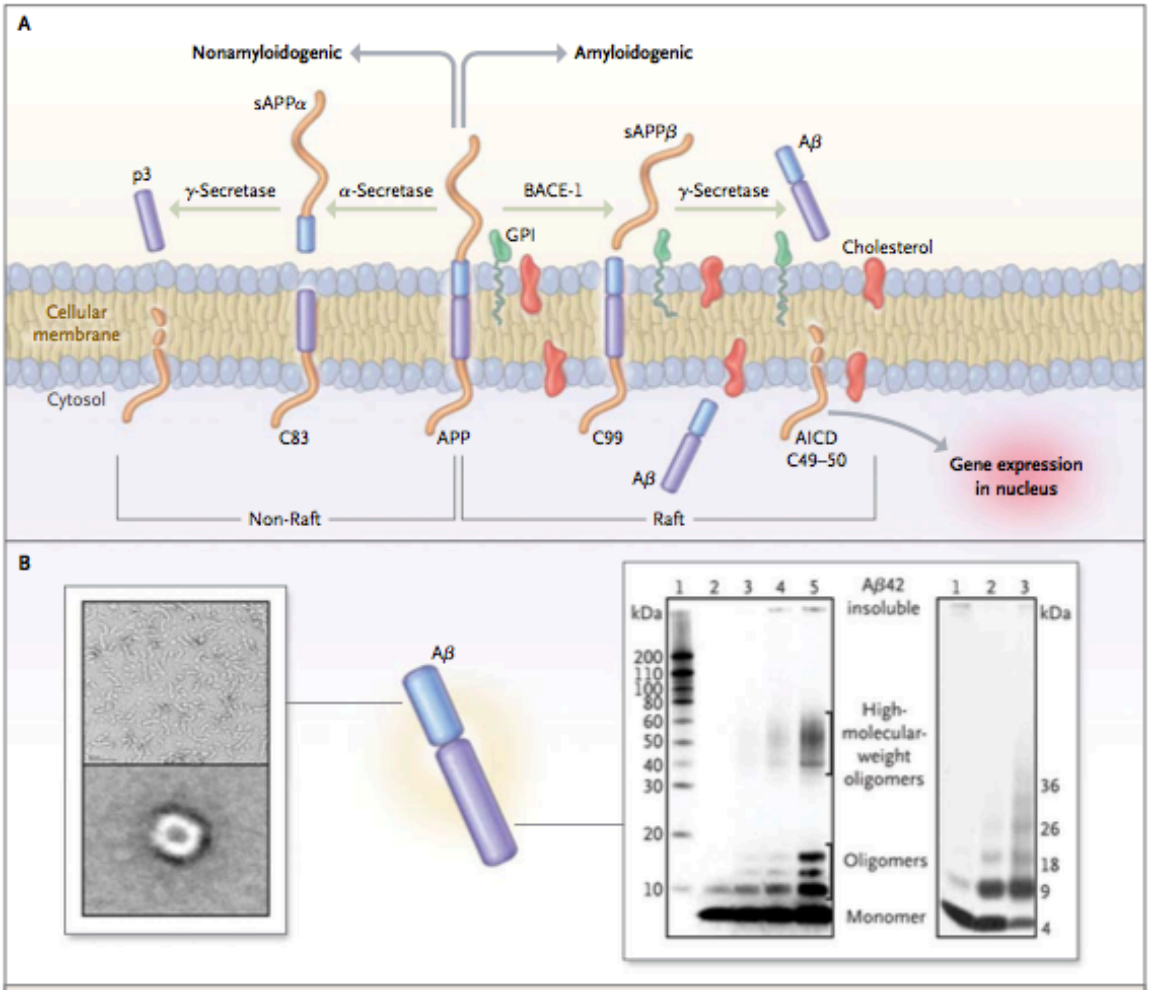

Figure 2.4 Processing of the Amyloid Precursor Protein. In Panel A, cleavage by α-secretase interior to the β-amyloid peptide (Aβ) sequence initiates nonamyloidogenic processing. The amyloid precursor protein (sAPPα) ectodomain is released, leaving behind an 83-residue carboxy-terminal fragment. C83 is then digested by γ-secretase, liberating extracellular p3 and the amyloid intracellular domain (AICD). Amyloidogenic processing is initiated by β-secretase beta-site amyloid precursor protein–cleaving enzyme 1 (BACE-1), releasing a shortened sAPPα. The retained C99 is also a γ-secretase substrate, generating Aβ and AICD. γ-Secretase cleavage occurs within the cell membrane in a unique process termed "regulated intramembranous proteolysis." sAPPα

and sAPPβ are secreted APP fragments after α-secretase and β-secretase cleavages, respectively. AICD is a short tail (approximately 50 amino acids) that is released into the cytoplasm after progressive ε-to-γ cleavages by γ-secretase. AICD is targeted to the nucleus, signaling transcription activation. Lipid rafts are tightly packed membrane microenvironments enriched in sphingomylelin, cholesterol, and glycophosphatidylinositol (GPI)–anchored proteins. Soluble Aβ is prone to aggregation. In Panel B, left inset, protofibrils (upper) and annular or pore like profiles (lower) are intermediate aggregates. In the right inset, self-association of 2 to 14 Aβ monomers into oligomers is dependent on concentration (left immunoblot). In the right immunoblot, oligomerization is promoted by oxidizing conditions (lane 2) and divalent metal conditions (lane 3).

Despite the fact that the amyloid plaques are the main hallmark of AD, the most neurotoxic form of the Aβ is the soluble oligomers, monomers and intermediate amyloids [24]. *In vitro* studies have been shown, that in brain slices preparations, dimers and trimers of Aβ are toxic to synapses [25,26]. In Human and mouse models of AD, the severity of the cognitive impairments correlates with levels of oligomers and monomers in the brain, not the total Aβ burden [24,27].

In order to reduce the Aβ burden, some enzymes and peptides have been tested as potential therapeutic targets. The proteases neprilysin and insulin-degrading enzyme was one of the first therapeutic for AD, based on their enzymatic activity on regulate steady-state levels of Aβ. Neprilysin-deficient knockout mice show both Alzheimer's-like

behavioral impairment and amyloid-beta deposition in the brain [28,29] providing strong evidence for the protein's association with the Alzheimer's disease process. In AD mouse models, deletion of insulin-degrading enzyme reduces Aβ degradation by more than 50% [30]. Conversely, overexpression of neprilysin or insulin-degrading enzyme prevents plaque formation [31]. However, prevention or reduction of plaques formation is not correlated with improvements on cognition.

On the other hand, clinical trials of a γ-secretase inhibitor [32], aggregation blockers, vaccination with Aβ, and monoclonal antibodies against various Aβ epitopes are in progress. The antibodies targeting the Aβ induce or trigger phagocytosis by microglia, or enhance clearance of Aβ, or both [33]. Vaccination in a phase 2 trial (NCT00021723) [34] resulted in encephalitis [35], and follow-up of immunized patients showed no cognitive or survival benefit despite diminution of plaques [36]. A phase 2 trial of passive immunization resulted in vasogenic cerebral edema in some patients (NCT00112073). Phase 3 trials of two monoclonal antibodies against Aβ (bapineuzumab and solanezumab) and of 10% intravenous immune globulin are under way (NCT00818662).

2.3.2 The Tau model

Neurofibrillary tangles, is considered the second hallmark of AD. They are filamentous inclusions of abnormally phosphorylated tau protein, which in their normal state binds to the microtubules and promotes their assembly and stability, facilitating vesicle transport. This hyper-phosphorylated anomaly occurs in AD and other neurodegenerative disorders termed tauopathies [37]. The major component of the tangles is an abnormally hyper-

phosphorylated and aggregated form of tau. Hyper-phosphorylated tau is insoluble, lacks affinity for microtubules, and self-associates into paired helical filament structures (Fig. 2.5). In contrast to amyloid plaques, the number of neurofibrillary tangles is a pathologic marker of the severity of AD.

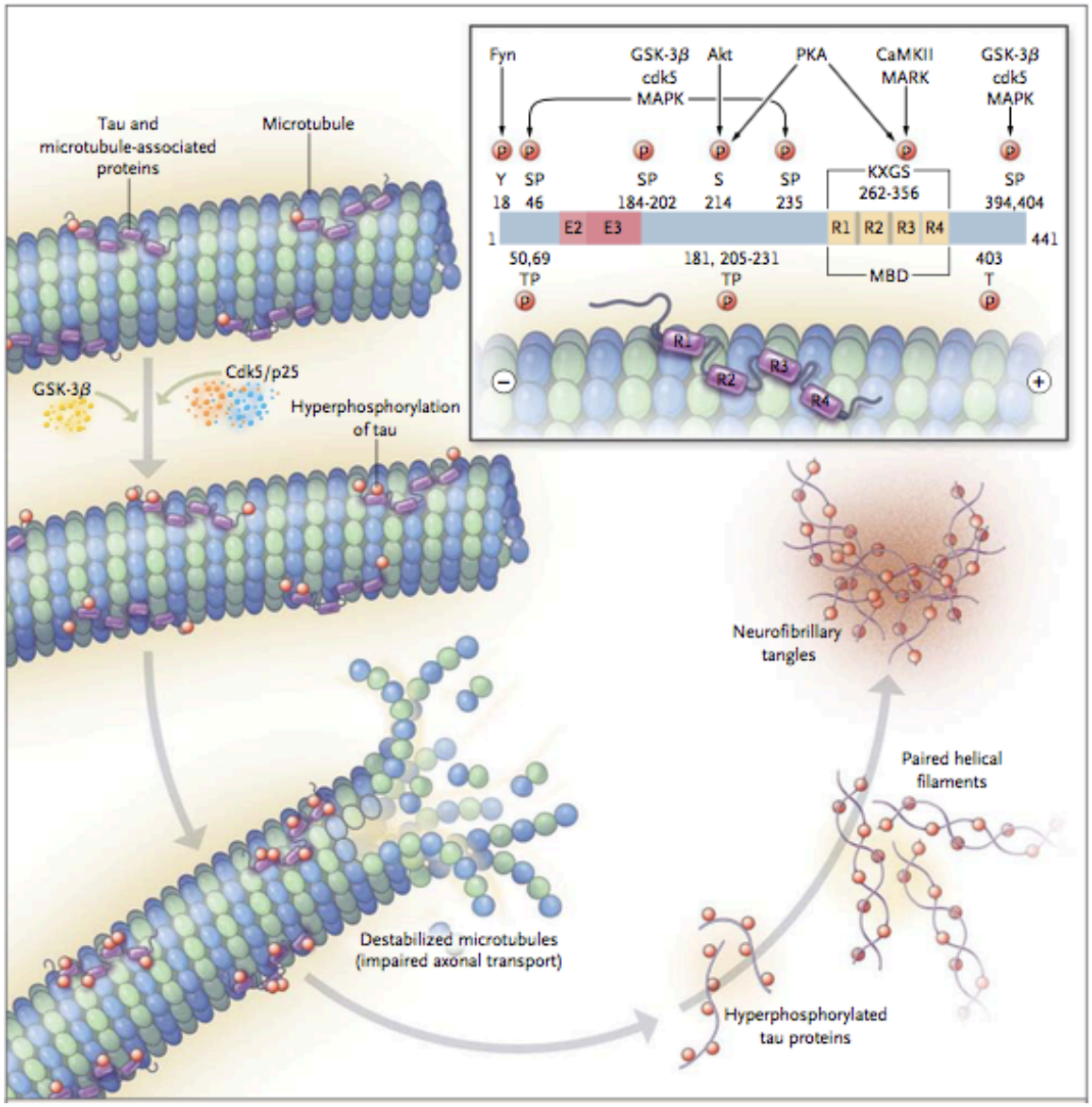

Figure 2.5 Tau Structure and Function. Four repeat sequences (R1-R4) make up the microtubule-binding domain (MBD) of tau. Normal phosphorylation of tau occurs on

serine (S; inset, above horizontal bar) and threonine (T; inset, below horizontal bar) residues, numbered according to their position in the full tau sequence. When followed by proline (P), these amino acids are phosphorylated by glycogen synthase kinase 3 (GSK-3β), cyclin-dependent kinase (cdk5) and its activator subunit p25, or mitogen-activated protein kinase (MAPK). Nonproline-directed kinases — Akt, Fyn, protein kinase A (PKA), calcium–calmodulin protein kinase 2 (CaMKII), and microtubule affinity-regulating kinase (MARK) — are also shown. KXGS (denoting lysine, an unknown or other amino acid, glycine, and serine) is a target motif. Hyperphosphorylated sites specific to paired helical filament tau in Alzheimer's disease tend to flank the MBD. Tau binding promotes microtubule assembly and stability. Excessive kinase, reduced phosphatase activities, or both cause hyperphosphorylated tau to detach and self-aggregate and microtubules to destabilize.

Like amyloid plaques, insoluble helical filament of tau may be inert, since increase on neuronal death is independent of the burden of neurofibrillary tangles [38]. Nevertheless the oligomers, intermediate aggregates of abnormal tau molecules are considered as the cytotoxic [39] component, which influence significantly on impairment of cognition [40,41]. Experimental evidence in mouse models of AD suggests that Aβ accumulation precedes and drives tau aggregation [42]. However, the elevated levels of phosphotau amino acids T181, T231, and total tau in the cerebrospinal fluid together, which constitute a biomarker, test with good accuracy for predicting incipient AD in patients with mild cognitive impairment [43].

Given the difficulties presented in order to validate a potential therapy against Aβ with significant improvement in cognition, new therapies against phosphorylated tau are under trial phases. Some new agents with significant potential to reduce the neurofibrillary tangle are small-molecule inhibitors of β-amyloid (e.g., scylloinositol) (NCT00568776) and tau oxidation and aggregation (e.g., methylene blue) (NCT00568776) [44]. A more general agent that also show promise as therapeutic is poly-phenolic extracts from grape seeds (e.g., resveratrol), which stimulate aging-suppressor genes [45].

2.3.3 The vascular model

The core hypothesis of the vascular model gives a new insight into the current understanding of the pathogenesis of AD. This hypothesis postulates that vascular abnormalities are considered early events, suggesting that pathology starts with hypoperfusion, or decreased blood flow to the brain. This, in turn, leads to a crisis among glia and neurons, eventually culminating in Aβ accumulation, neurofibrillary tangles formation, neurodegeneration and cognitive impairment [46].

In addition to disruption of the vascular network present in AD, local and systemic inflammation triggers the cycle of protein aggregation and oxidative stress in the brain, leading to strokes and white-matter lesions, which contribute to cognitive decline. Ischemic components affect 60 to 90% of patients with AD, with major infarctions representing 30% of vascular lesions in autopsy cases. Conversely, 30% of putative cases of vascular dementia also present pathological features of AD. Despite the fact that pure cases of vascular dementia are recognized clinically via imaging [47,48], most cases of

dementia are in fact mixed. The most common pathological changes include cerebral amyloid angiopathy (CAA), [49] affecting more than 90% of patients with AD, capillary abnormalities, disruption of the blood–brain barrier [50]. All this pathological changes explain the local reduction of brain blood flow, nevertheless none of them explain the global hypoperfusion presented in AD patients [51,52].

Another main component of the vascular hypothesis is that the accumulation of Aβ is due to disruptions of the Aβ clearance pathways due to loss of function of the vascular unit. The main sources of vascular Aβ and CAA are neurons, myocytes and the Aβ on circulation. *Ex vivo* experiments have been shown that vascular AB could contribute to blood flow reduction by inducing vasoconstriction [53], cytotocixity to the endothelium [54] and smooth muscle cells [55], conferring a predisposition to microhemorages. The "neurovascular uncoupling" hypothesis proposes that deregulation of Aβ transport across the capillary blood–brain barrier is caused by the imbalanced expression of low-density lipoprotein receptor–related proteins and receptors for advanced glycation end products, which mediate Aβ efflux and influx, respectively [56] (Fig. 2.6).

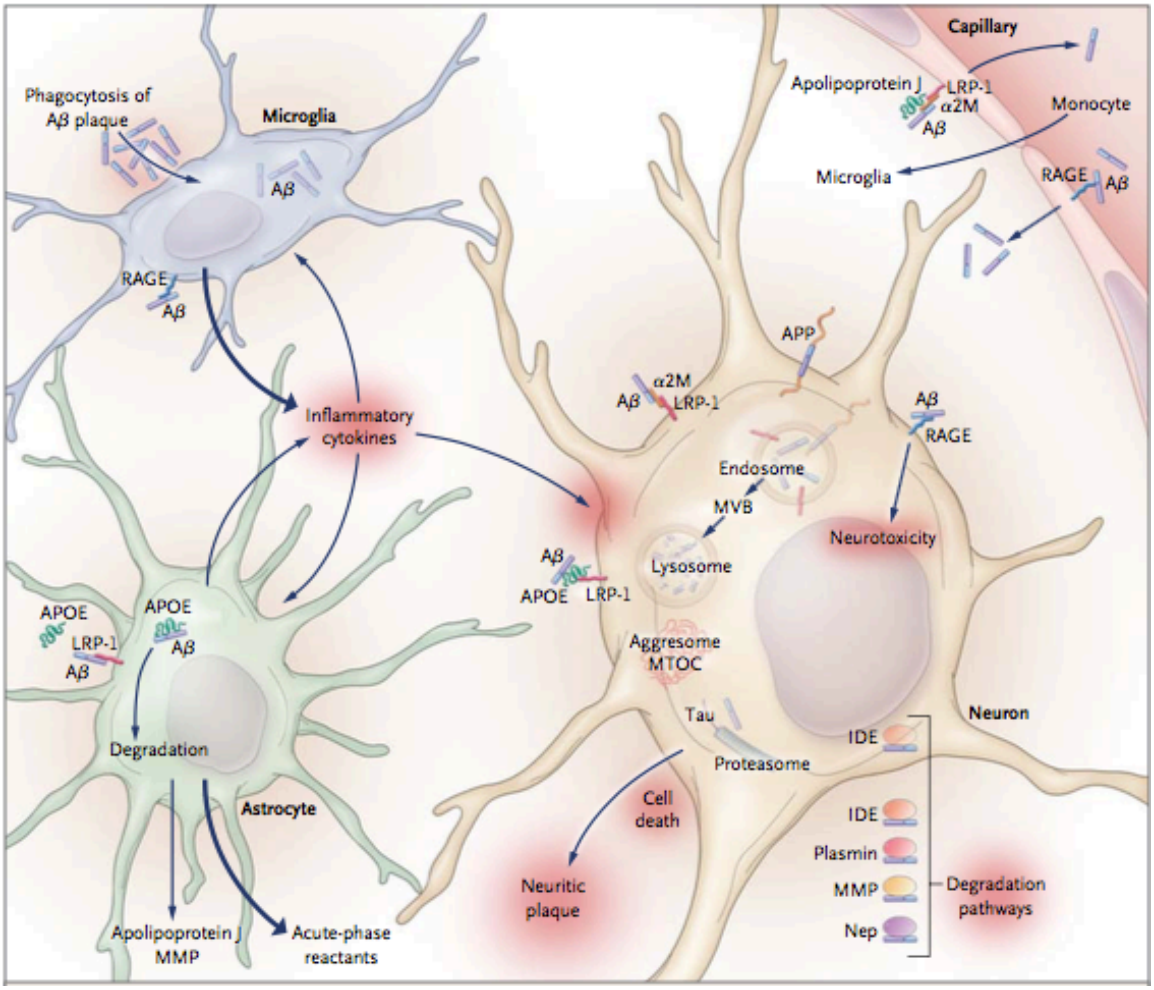

Figure 2.6 Inflammation and Mechanisms of Aβ Clearance. β-amyloid peptide (Aβ) is formed within intracellular compartments (the endoplasmic reticulum, Golgi apparatus, and endosomes) or it can enter multiple cell types through the low-density lipoprotein receptor–related protein. The ubiquitous apolipoprotein E (APOE) and α2-macroglobulins (α2M) are chaperones in this process and in the genesis of extracellular plaques. Microglia directly engulf Aβ through phagocytosis. Astrocytes also participate in Aβ clearance through receptor-mediated internalization and facilitation of its transfer out of the central nervous system and into the circulation. Microglia and astrocytes are recruited and stimulated in Alzheimer's disease to release proinflammatory cytokines and

acute-phase reactants. Receptors for advanced glycation end products (RAGE) molecules transduce extra- cellular Aβ toxic and inflammatory effects and mediate influx of vascular Aβ. The inflammatory milieu provokes neuritic changes and break- down of the vascular blood–brain barrier. In addition to cell-mediated reactions, Aβ clearance occurs through enzymatic proteolysis, mainly through neprilysin (Nep) and insulin-degrading enzyme (IDE). Aβ oligomers block proteasome function, facilitating the buildup of intracellular tau and accumulation of Aβ into "aggresomes." APP denotes amyloid precursor protein, MMP matrix metalloproteinase, MOTC microtubule-organizing center, and MVB multivesicular body.

2.3.4 A new key component to the vascular model

The previous model presented, could explain the local hypoperfusion phenomena but not the global blood flow reduction presented in AD patients and mouse models. In order to explain the local and global perfusion, we propose a new model based on the obstruction of small capillaries. In this model we considered the interaction of the circulatory system (mostly leukocytes), the cerebral vascular unit, and the influence of inflammation presented in AD brains.

Cerebral vascular Unit

Neuronal and brain vascular network are characterized by their complexity on specialization, structural and functionality hierarchy and constant metabolic demands. The importance of the vascular network in the brain reside on the fact that even though the brain represents 20-25% of the metabolic demand in the entire body, the brain has a

limited capacity to store energy [57]. To highlight this point, small alterations in the brain vascular network affecting blood supply have significant metabolic consequences [58] resulting in different brain pathologies [59].

In order to regulate the constant supply of oxygen and nutrients at different levels of metabolic demands, the vascular network is able to perform two different mechanisms: autoregulation and hyperemia. Autoregulation is the mechanism that regulates the supply of oxygen and nutrients through changes in cerebral vascular tone. Autoregulation is the mechanism that protects the cerebral blood flow (CBF) in physiological situations, such as exercise, and in pathological conditions, such as cardiogenic shock [60]. On the other hand, hyperemia is the mechanism that regulates CBF locally, ensuring that the supply of oxygen and nutrients matches the changes in activity of specific brain regions [61]. The hyperemia mechanism is activated, for example, in physiological situations, such as reading, calculating, or any other mental exercise [62].

The changes in cerebral blood supply to match the metabolic demands in controlled by a group of cells of both vascular and neural origin, called the neurovascular unit (NVU). The NVU comprises vascular cells (that is, endothelium, pericytes, vascular smooth muscle cells), glial cells (that is, astrocytes, microglia, and oliogodendroglia) and neurons (Fig. 2.7) [63].

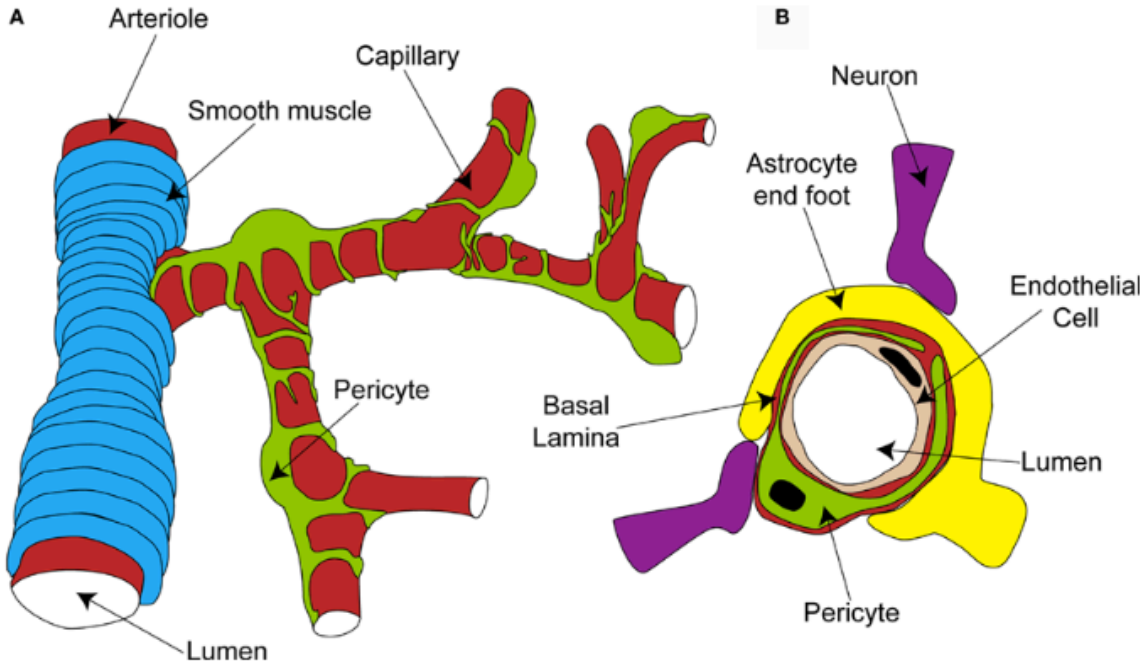

Figure 2.7 Organization of the capillary neurovascular unit. (A) Rings of smooth muscle encircle arterioles, while pericytes send processes along and around capillaries, without fully covering the vessel. (B) Pericytes are located outside the endothelial cells and are separated from them and the parenchyma by a layer of basal lamina. In the parenchyma, astrocyte end-feet and neuronal terminals are closely associated with the capillary.

Each of these cell components are intimately and reciprocally linked to each other, establishing an anatomical and functional unit, which results in a highly efficient system to regulate CBF. From these components, the endothelial cells are connected by tight and adherens junctions which acts as filters that regulate the transport of oxygen, nutrients and metabolic residues from in and out of the blood brain barrier.

Importantly, another critical role for endothelial cells is regulating leukocyte adhesion and eventual infiltration into the tissues during inflammation. Adhesion is a well-characterized response, which leads to activation of the endothelium as well as eventual extravasation of immune cells [64]. Usually endothelial cells change their phenotypes based on the stimuli, where the inflammation cascade driven by pathogens or cytokines leads to their active phenotype. In their active phenotype, the endothelial cells express numerous adhesive molecules including the selectins, ICAM, VCAM, chemoattractant molecules, and cytokines (MCP-1, IL-lp\ IL-8, and TGF-p) [65-67]. These molecules act to attract and provide anchor sites for leukocytes recruitment, adhesion and extravasation.

Chronic stimulation of the endothelial cells leads to endothelial dysfunction [68,69]. It is likely that endothelial dysfunction is a common pathology in AD due to the constitutive and systemic inflammation presented in the brain. This state of dysfunction induces a proinflammatory state, which promotes the activation and migration of leukocytes. Chronic endothelial dysfunction can lead to vasoconstriction, decreased blood flow and weakening of the vessels [68,69].

Leukocytes

Leukocytes are the cells of the immune system, which help, protect the body from foreign invaders as well as respond to injury and infectious diseases. There are several types of immune cells. The most relevant for our discussion are: blood-derived monocytes, blood-derived neutrophils, tissue-derived macrophages and microglia. Monocytes are circulating leukocytes, which function primarily as phagocytes, cytokines production and

antigen presenting cells. Neutrophils are the most abundant circulating leukocytes, which function primarily as phagocytes, degranulation (release of anti-microbial agents) and generation of neutrophil extracellular traps (NET's). Macrophages are monocytes which have migrated into the tissues and become tissue resident phagocytic cells. Microglia is a glial cell, which is considered the resident macrophage in the Central Nervous System (CNS), which function primarily as phagocytes, scavengers, cytokines producers, antigen presenting cells, and a promoter of tissue repair.

Predominantly, monocytes, neutrophils, macrophage and microglia are key cell types involved in the development and progression of atherosclerosis, vascular dementia and AD, respectively. Based on specific stimulations, monocytes, neutrophils, macrophages, and microglia can go through multiple changes to adopt a active phenotype. Activated cells alter expression of a variety of genes, including cell adhesion molecules, cytokines, chemokines and co-stimulatory molecules [70,71]. Monocytes, neutrophils, macrophages, and microglia utilize these proteins to increase their adhesion and migration ability, restructure their cytoskeleton to assist in phagocytosis and migration, and to stimulate surrounding cells via secretion of chemokines [72].

The hypothesis that brain hypoperfusion in AD is due to leukocyte plugging in capillaries and that this reduced blood flow contributes significantly to the cognitive impact of the disease is both novel and supported by our recent results (see chapter 4). Taken together, our data suggest a working model to explain the origin and consequences of brain hypoperfusion in AD: Aβ monomers accumulation leads to increased expression of

inflammatory receptors on the vessel lumen. This vascular inflammation causes leukocytes (mostly neutrophils) to adhere and block blood flow in capillaries, resulting in decreases in brain perfusion. This blood flow deficit directly contributes to cognitive dysfunction and also accelerates Aβ aggregation by decreasing clearance of Aβ monomers.

Because one stalled capillary causes decreased flow in several downstream vessels, the impact on total brain blood flow is significant. We found that these stalls were caused by adhered neutrophils and when we blocked this adhesion, the capillary stalls got released, leading to an immediate ~30% increase in cortical CBF. Hypoperfusion likely contributes to cognitive deficits in AD patients and recent work has shown that flow reductions increase the rate of amyloid beta (Aβ) deposition [73-76], suggesting a positive feedback mechanism between Aβ aggregation and brain blood flow decreases, with each impacting neural function [77]. In addition, inflammation is a persistent and well-recognized feature of AD. A significant contributor to this inflammation is increased reactive oxygen species (ROS) induced by brain exposure to Aβ monomers aggregates. These ROS cause a loss of cerebrovascular flow regulation [78,79] and result in an increase in inflammatory adhesion receptors on endothelial cells [80-82]. We suggest that Aβ-induced endothelial ROS could drive the vascular inflammation that likely underlies leukocyte plugging of capillaries.

In addition, there is a mutually reinforcing cascade of injury where AD pathophysiology drives vascular dysfunction and vice versa (Fig. 2.8). Indeed, microvascular strokes [73]

and brain hypoperfusion [74,83,84] have been shown to increase the rate of Aβ deposition. This vicious cycle of damage suggests a need to treat vascular dysfunction as well as Aβ aggregation and toxicity in AD patients. Reducing the blood flow deficit in AD could directly improve cognition and slow AD progression, but first the cause of this hypoperfusion must be identified. Our data in AD mouse models suggest that leukocyte plugging of brain capillaries, likely caused by increased vascular inflammation, could account for the decreased brain blood flow in AD.

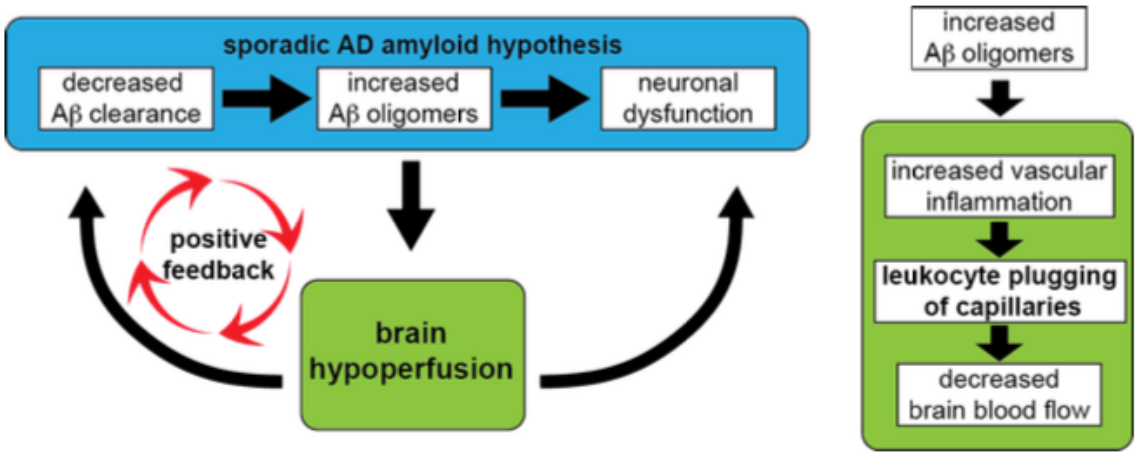

Figure 2.8 Brain hypoperfusion in the progression of AD and the role of leukocyte plugging of brain capillaries. (left) In sporadic AD, decreased clearance of Aβ with age (and other risk factors) is thought to lead to an increase in Aβ oligomers in the brain, which, through a variety of mechanisms, leads to neural dysfunction. Our data suggests that the brain hypoperfusion present in AD is also be caused by Aβ oligomer toxicity. This hypoperfusion likely contributes directly to neural dysfunction and also decreases clearance of Aβ from the brain, forming a positive feedback loop that may drive disease

progression. (right) We propose that Aβ oligomers lead to increased inflammation in capillary endothelial cells. Leukocytes then adhere to these inflamed capillary segments, blocking flow and reducing overall brain blood perfusion.

2.4 CONCLUSIONS AND CLINICAL IMPLICATIONS

Current treatment strategies for AD are focused on ameliorating the progression of the disease, maintain cognitive ability and reduce the phenotypic behavior related to the disease. However, there are no known treatments to prevent or cure AD. As some major key components for AD are still unknown, targeted treatments that effectively combat the development of the disease have proven to be elusive (Aβ amyloids and Tau vaccines).

The major limitation in recent efforts to treat the disease is the lack of preclinical detection. There is an urgent need to identify cellular, molecular, and functional phenotypes associated with defined stages of the disease progression. Clinically, many types of AD-related dementias (i.e., frontotemporal, vascular, mixed, and Lewy-body dementias) in addition to normal aging exhibit both amyloid accumulation and vascular dysfunction. Though amyloid changes occur during preclinical stages of AD, measures of amyloid (CSF levels of Aβ42 and Pittsburgh compound B PET) and tau do not appear to be sensitive enough to predict the early onset of cognitive impairment and AD clinical diagnosis. Elucidating the precise mechanism through which vascular insults influence AD development would be beneficial and might help identify new biomarkers associated with preclinical stages of the disease in addition to identify novel biologic targets for drug development and aid in patient-directed treatment efforts.

References:

1. Morris, J. C. Dementia Update 2003. Alzheimer Dis. Assoc. Disord. **17**, 245–258 (2003).
2. Ferri CP, Prince M, Brayne C, et al. Global prevalence of dementia: a Delphi consensus study. Lancet **366:** 2112–17 (2005).
3. Blennow, K., de Leon, M. J., & Zetterberg, H. Alzheimer's disease.The Lancet **368,** 387-403 (2006).
4. Iadecola, C. Neurovascular regulation in the normal brain and in Alzheimer's disease. *Nature Reviews Neuroscience*, **5**, 347-360 (2004).
5. Niwa K, Kazama K, Younkin S.G, Carlson G.A, & Iadecola C. Alterations in cerebral blood flow and glucose utilization in mice overexpressing the amyloid precursor protein. *Neurobiol Dis* **9**:61-68 (2002) 25
6. Iturria-Medina, Y. *et al.* Early role of vascular dysregulation on late-onset Alzheimer's disease based on multifactorial data-driven analysis. *Nature communications* **7**, 11934, doi:10.1038/ncomms11934 (**2016**).
7. Wardlaw, J. M. & Horsburgh, K. Small vessels, dementia and chronic diseases-molecular mechanisms and pathophysiology. *Clinical science* **130**, 1875-1879, doi:10.1042/CS20160376 (2016).
8. Dai, W. *et al.* Mild cognitive impairment and alzheimer disease: patterns of altered cerebral blood flow at MR imaging. *Radiology* **250**, 856-866, doi:10.1148/radiol.2503080751 (2009).
9. Roher, A. E. *et al.* Cerebral blood flow in Alzheimer's disease. *Vascular health and risk management* **8**, 599-611, doi:10.2147/VHRM.S34874 (2012).

10. Park L, Koizumi K, El Jamal S, Zhou P, Previti ML, Van Nostrand WE, Carlson G, Iadecola C. Stroke. **2014** Jun;45(6):1815-21. doi: 10.1161/STROKEAHA.114.005179. Epub **2014** Apr 29.
11. Hebert LE, Weuve J, Scherr PA, Evans DA. Alzheimer disease in the United States (2010-2050) estimated using the 2010 Census. Neurology 2013;80(19):1778-83.
12. Alzheimer's Association. Early-Onset Dementia: A National Challenge, a Future Crisis. Washington, D.C.: Alzheimer's Association; 2006.
13. Ortman JM, Velko VA, Hogan H. An Aging Nation: The Older Population in the United States, Current Population Reports, P25-1140. U.S. Census Bureau, Washington, D.C. 2014. Available at: census.gov/content/dam/Census/library/publications/2014/ demo/p25-1140.pdf. Accessed November 24, 2016.
14. Hebert LE, Beckett LA, Scherr PA, Evans DA. Annual incidence of Alzheimer disease in the United States projected to the years 2000 through 2050. Alzheimer Dis Assoc Disord 2001;15(4):169-73.
15. Hebert LE, Scherr PA, Bienias JL, Bennett DA, Evans DA. Alzheimer's disease in the U.S. population: Prevalence estimates using the 2000 Census. Arch Neurol 2003;60:1119-22.
16. Kochanek KD, Murphy SL, Xu JQ, Tejada-Vera B. Deaths: Final Data for 2014. National Vital Statistics Reports; vol 65, no 4. Hyattsville, Md.: National Center for Health Statistics: 2016.

17. Brookmeyer R, Gray S, Kawas C. Projections of Alzheimer's disease in the United States and the public health impact of delaying disease onset. Am J Public Health 1998;88:1337-42.

18. Hardy J, Selkoe DJ. The amyloid hypothesis of Alzheimer's disease: progress and problems on the road to therapeutics. Science. 2002;297:353-356.

19. Nathalie P, Jean-Noe¨ l O. Processing of amyloid precursor protein and amyloid peptide neurotoxicity. Curr Alzheimer Res. 2008;5:92-99.

20. Matsui T, Ingelsson M, Fukumoto H, et al. Expression of APP pathway mRNAs and proteins in Alzheimer's disease. Brain Res. 2007;1161:116-123.

21. Minati, L., et al. (2009). "Current concepts in Alzheimer's disease: a multidisciplinary review." Am J Alzheimers Dis Other Demen **24**(2): 95-121.

22. Kayed R, Head E, Thompson JL, et al. Common structure of soluble amyloid oligomers implies common mechanism of pathogenesis. Science 2003;300:486-9.

23. Klein WL, Krafft GA, Finch CE. Tar- geting small Abeta oligomers: the solu- tion to an Alzheimer's disease conundrum? Trends Neurosci 2001;24:219-24.

24. Hong S, Beja-Glasser VF, Nfonoyim BM, Frouin A, Li S, Ramakrishnan S, Merry KM, Shi Q, Rosenthal A, Barres BA, Lemere CA, Selkoe DJ, Stevens B. (2016). Complement and microglia mediate early synapse loss in Alzheimer mouse models. Science. 2016 May 6;352(6286):712-6. doi: 10.1126/science.aad8373.

25. Walsh DM, Townsend M, Podlisny MB, et al. Certain inhibitors of synthetic amyloid beta-peptide (Abeta) fibrillogen- esis block oligomerization of natural Abeta and thereby rescue long-term poten- tiation. J Neurosci 2005;25:2455-62.

26. Klyubin I, Betts V, Welzel AT, et al. Amyloid beta protein dimer-containing human

CSF disrupts synaptic plasticity: prevention by systemic passive immuni- zation. J Neurosci 2008;28:4231-7.

27. Lue LF, Kuo YM, Roher AE, et al. Sol- uble amyloid beta peptide concentration as a predictor of synaptic change in Alz- heimer's disease. Am J Pathol 1999;155: 853-62.
28. Iwata N, Tsubuki S, Takaki Y, et al. Metabolic regulation of brain Abeta by neprilysin. Science 2001;292:1550-2.
29. Madani, R., et al. (2006). "Lack of neprilysin suffices to generate murine amyloid-like deposits in the brain and behavioral deficit in vivo." J Neurosci Res 84(8): 1871-1878.
30. Farris W, Mansourian S, Chang Y, et al. Insulin-degrading enzyme regulates the levels of insulin, amyloid beta-protein, and the beta-amyloid precursor protein intra-cellular domain in vivo. Proc Natl Acad Sci U S A 2003;100:4162-7.
31. Leissring MA, Farris W, Chang AY, et al. Enhanced proteolysis of beta-amyloid in APP transgenic mice prevents plaque formation, secondary pathology, and pre-mature death. Neuron 2003;40:1087-93.
32. Siemers ER, Quinn JF, Kaye J, et al. Effects of a gamma-secretase inhibitor in a randomized study of patients with Alz- heimer disease. Neurology 2006;66:602-4.
33. McGeer PL, McGeer E. Is there a fu- ture for vaccination as a treatment for Alz-heimer's disease? Neurobiol Aging 2003; 24:391-5.
34. Hock C, Konietzko U, Streffer JR, et al. Antibodies against beta-amyloid slow cog-nitive decline in Alzheimer's disease. Neuron 2003;38:547-54.
35. Gilman S, Koller M, Black RS, et al. Clinical effects of Abeta immunization (AN1792) in patients with AD in an inter- rupted trial. Neurology 2005;64:1553-62.

36. Holmes C, Boche D, Wilkinson D, et al. Long-term effects of Abeta42 immunisation in Alzheimer's disease: follow-up of a randomised, placebo-controlled phase I trial. Lancet 2008;372:216-23.

37. Lee VM, Goedert M, Trojanowski JQ. Neurodegenerative tauopathies. Annu Rev Neurosci 2001;24:1121-59.

38. Andorfer C, Kress Y, Espinoza M, et al. Hyperphosphorylation and aggregation of tau in mice expressing normal human tau isoforms. J Neurochem 2003;86:582-90.

39. Khlistunova I, Biernat J, Wang Y, et al. Inducible expression of Tau repeat domain in cell models of tauopathy: aggregation is toxic to cells but can be reversed by inhibitor drugs. J Biol Chem 2006;281:1205- 14.

40. Santacruz K, Lewis J, Spires T, et al. Tau suppression in a neurodegenerative mouse model improves memory function. Science 2005;309:476-81.

41. Oddo S, Vasilevko V, Caccamo A, Kita- zawa M, Cribbs DH, LaFerla FM. Reduction of soluble Abeta and tau, but not soluble Abeta alone, ameliorates cognitive decline in transgenic mice with plaques and tangles. J Biol Chem 2006;281:39413-23.

42. Lewis J, Dickson DW, Lin WL, et al. Enhanced neurofibrillary degeneration in transgenic mice expressing mutant tau and APP. Science 2001;293:1487-91.

43. Mattsson N, Zetterberg H, Hansson O, et al. CSF biomarkers and incipient Alzheimer disease in patients with mild cognitive impairment. JAMA 2009;302: 385-93.

44. McLaurin J, Kierstead ME, Brown ME, et al. Cyclohexanehexol inhibitors of Abeta aggregation prevent and reverse Alzhei- mer phenotype in a mouse model. Nat Med 2006;12:801-8.

45. Ono K, Condron MM, Ho L, et al. Ef- fects of grape seed-derived polyphenols on amyloid beta-protein self-assembly and cytotoxicity. J Biol Chem 2008;283:32176-87.

46. de la Torre JC. Is Alzheimer's disease a neurodegenerative or a vascular disorder? Data, dogma, and dialectics. *Lancet Neurol*. 2004 Mar;3(3):184-90

47. O'Brien JT, Erkinjuntti T, Reisberg B, et al. Vascular cognitive impairment. Lancet Neurol 2003;2:89-98.

48. Hachinski V, Iadecola C, Petersen RC, et al. National Institute of Neurological Disorders and Stroke–Canadian Stroke Network vascular cognitive impairment harmonization standards. Stroke 2006;37: 2220-41.

49. Greenberg SM, Gurol ME, Rosand J, Smith EE. Amyloid angiopathy-related vascular cognitive impairment. Stroke 2004; 35:Suppl 1:2616-9.

50. Roher AE, Esh C, Rahman A, Kokjohn TA, Beach TG. Atherosclerosis of cerebral arteries in Alzheimer disease. Stroke 2004;35:Suppl 1:2623-7.

51. Ruitenberg A, den Heijer T, Bakker SL, et al. Cerebral hypoperfusion and clinical onset of dementia: the Rotterdam Study. Ann Neurol 2005;57:789-94.

52. Jagust WJ. Neuroimaging in dementia. Neurol Clin 2000;18:885-902.

53. Price JM, Chi X, Hellermann G, Sutton ET. Physiological levels of beta-amyloid induce cerebral vessel dysfunction and reduce endothelial nitric oxide production. Neurol Res 2001;23:506-12.

54. Paris D, Patel N, DelleDonne A, Quadros A, Smeed R, Mullan M. Impaired angiogenesis in a transgenic mouse mod- el of cerebral amyloidosis. Neurosci Lett 2004;366:80-5.

55. Van Nostrand WE, Melchor JP, Ruffini L. Pathologic amyloid beta-pro- tein cell surface fibril assembly on cultured human cerebrovascular smooth muscle cells. J Neurochem 1998;70:216-23.

56. Deane R, Zlokovic BV. Role of the blood-brain barrier in the pathogenesis of Alzheimer's disease. Curr Alzheimer Res 2007;4:191-7.

57. Zlokovic B. V. The blood-brain barrier in health and chronic neurodegenerative disorders. *Neuron*. 2008;57(2):178–201. doi: 10.1016/j.neuron.2008.01.003.

58. Moore, C.I. & Cao, R. 2008. The hemo-neural hypothesis: on the role of blood flow in information processing. J Neu- rophysiol 99, 2035–2047.

59. Moskowitz MA, Lo EH, Iadecola C. The science of stroke: mechanisms in search of treatments. Neuron. 2010;67(2):181–198.

60. Iadecola, C., Zhang, F. & Xu, X. 1993. Role of nitric oxide synthase-containing vascular nerves in cerebrovasodilation elicited from cerebellum. Am J Physiol 264, R738–R746.

61. Filosa, J.A. 2010. Vascular tone and neurovascular coupling: considerations toward an improved in vitro model. Front Neuroenergetics 2, 305, H609-H619.

62. Gordon, G.R.J., Mulligan, S.J. & MacVicar, B.A. 2007. Astrocyte control of the cerebrovasculature. Glia 55, 1214–1221.

63. Abbott, N.J. & Friedman, A. 2012. Overview and introduction: the blood-brain barrier in health and disease. Epilepsia 53, 1–6.

64. Gerrity, R. G. "The Role of the Monocyte in Atherogenesis: I. Transition of Blood-Borne Monocytes into Foam Cells in Fatty Lesions." *The American Journal of Pathology* 103.2 (1981): 181–190. Print.

65. Gebuhrer V, Murphy JF, Bordet JC, Reck MP, McGregor JL. Oxidized low-density lipoprotein induces the expression of P-selectin (GMP140/PADGEM/CD62) on human endothelial cells. Biochem J 1995;306(Pt 1):293–8.

66. Khan BV, Parthasarathy SS, Alexander RW, Medford RM. Modified low density lipoprotein and its constituents augment cytokine-activated vascular cell adhesion molecule-1 gene expression in human vascular endothelial cells. J Clin Invest 1995;95:1262–70

67. Rajavashisth T, Qiao JH, Tripathi S, Tripathi J, Mishra N, Hua M, et al. Heterozygous osteopetrotic (op) mutation reduces atherosclerosis in LDL receptor-deficient mice. J Clin Invest 1998;101:2702–10.

68. Rensink, A. A., de Waal, R. M., Kremer, B. & Verbeek, M. M. Pathogenesis of cerebral amyloid angiopathy. *Brain Res Brain Res Rev* **43**, 207-223 (2003).

69. Zlokovic, B. V., Deane, R., Sallstrom, J., Chow, N., and Miano, J. M. (2005). Neurovascular pathways and Alzheimer amyloid beta-peptide. *Brain Pathol.* 15, 78–83.

70. Frohman, E. M., Frohman, T. C., Gupta, S., de Fougerolles, A., and van den Noort, S. Expression of intercellular adhesion molecule 1 (ICAM-1) in Alzheimer's disease. *Journal of the Neurological Sciences* **106**, 105-11, (1991).

71. McGeer PL, McGeer EG. Inflammation, autotoxicity and Alzheimer disease. Neurobiol Aging (2001) 22:799–809.10.1016/S0197-4580(01)00289-5

72. Thomas, W. E. (1999). Brain macro- phages: on the role of pericytes and perivascular cells. *Brain Res. Brain Res. Rev.* 31, 42–57.

73. Garcia-Alloza, M. *et al.* Cerebrovascular lesions induce transient beta-amyloid deposition. *Brain : a journal of neurology* **134**, 3697-3707, doi:10.1093/brain/awr300 (2011).

74. Koike, M. A., Green, K. N., Blurton-Jones, M. & Laferla, F. M. Oligemic hypoperfusion differentially affects tau and amyloid-{beta}. *The American journal of pathology* **177**, 300-310, doi:10.2353/ajpath.2010.090750 (2010).

75. van Groen, T., Puurunen, K., Maki, H. M., Sivenius, J. & Jolkkonen, J. Transformation of diffuse beta- amyloid precursor protein and beta-amyloid deposits to plaques in the thalamus after transient occlusion of the middle cerebral artery in rats. *Stroke; a journal of cerebral circulation* **36**, 1551-1556 (2005).

76. Li, L. *et al.* Hypoxia increases Abeta generation by altering beta- and gamma-cleavage of APP. *Neurobiology of aging* **30**, 1091-1098, doi:10.1016/j.neurobiolaging.2007.10.011 (2009).

77. Iadecola, C. *et al.* SOD1 rescues cerebral endothelial dysfunction in mice overexpressing amyloid precursor protein. *Nature neuroscience* **2**, 157-161 (1999).

78. Iadecola, C. Neurovascular regulation in the normal brain and in Alzheimer's disease. *Nature Reviews Neuroscience* **5**, 347-360 (2004).

79. Vromman, A. *et al.* beta-Amyloid context intensifies vascular smooth muscle cells induced inflammatory response and de-differentiation. *Aging cell* **12**, 358-369, doi:10.1111/acel.12056 (2013).

80. Fonseca, A. C., Ferreiro, E., Oliveira, C. R., Cardoso, S. M. & Pereira, C. F. Activation of the endoplasmic reticulum stress response by the amyloid-beta 1-40

peptide in brain endothelial cells. *Biochimica et biophysica acta* **1832**, 2191-2203, doi:10.1016/j.bbadis.2013.08.007 (2013).

81. Gonzalez-Velasquez, F. *et al.* Activation of brain endothelium by soluble aggregates of the amyloid- beta protein involves nuclear factor-kappaB. *Current Alzheimer research* **8**, 81-94 (2011).
82. Nicolakakis, N. & Hamel, E. Neurovascular function in Alzheimer's disease patients and experimental models. *Journal of cerebral blood flow and metabolism : official journal of the International Society of Cerebral Blood Flow and Metabolism* **31**, 1354-1370, doi:10.1038/jcbfm.2011.43 (2011).
83. Okamoto, Y. *et al.* Cerebral hypoperfusion accelerates cerebral amyloid angiopathy and promotes cortical microinfarcts. *Acta neuropathologica* **123**, 381-394, doi:10.1007/s00401-011-0925-9 (2012).
84. Koike, M. A., Garcia, F. G., Kitazawa, M., Green, K. N. & Laferla, F. M. Long term changes in phospho- APP and tau aggregation in the 3xTg-AD mice following cerebral ischemia. *Neuroscience letters* **495**, 55-59, doi:10.1016/j.neulet.2011.03.034 (2011).

CHAPTER 3

NONLINEAR OPTICAL MICROSCOPY

In this introductory chapter we discuss the use of nonlinear optics for visualization and manipulation of biological systems. An overview of two- and three- photon microscopy (2PM and 3PM, respectively) and its advantages for in vivo work are presented. We then consider the processes of second and third harmonic generation (SHG and THG, respectively), and how these techniques share a common platform but a different mechanism than 2PM. Finally, we round out the chapter with a discussion of the significance of non-linear optics imaging and the description of our 2PM experimental setup.

The advantages of nonlinear optical techniques such as 2PM and 3PM allowed me to perform *in vivo* imaging in the mouse cortex and hippocampus and investigate and characterized a new cellular phenomena in Alzheimer's mouse model (Chapter 4) and record neuronal in hippocampus region (Chapter 6).

In vivo imaging is critical for understanding systems networks, tissue structure and function, cellular dynamics, etc. as it occurs within an intact organism. Recent advances in non-linear optical imaging such as two-photon excited fluorescence microscopy (2PM) and three-photon microscopy (3PM) allow us to study the progression of diseases in complex biological systems as the brain, the heart, the spinal cord, etc. during *in vivo* experiments [1,2]. 2PM provides the best optical system to perform *in vivo* imaging at

subcellular level within 1 mm volume inside the brain without causing damage to the surrounding tissue [3,4]. However, the maximum imaging depth for 2PM is limited by the signal-to-background ratio (SBR). On the other hand, 3PM is an improvement over two-photon imaging because the SBR is orders of magnitude higher within the mouse brain [2]. In this chapter we provide an overview of 2PM and 3PM, second and third harmonic generation processes, the use of non-linear microscopy for *in vivo* imaging and the experimental setup. The imaging techniques discussed in this chapter are used primarily in Chapters 4 and 6.

3.1 Two-Photon Excited Fluorescence

2PM was first demonstrated by Denk, Strickler, and Webb in 1990 and revolutionized the field of tissue imaging in *vivo*, becoming the most widely used multiphoton imaging modality [5]. The non-linear nature of 2-photon absorption required the simultaneous interaction (10^{-16} s) between two-photons and the fluorophore in a determined focal region in order to reach the higher energy state [6] (Fig. 3.1). Because the generated fluorescence signal is quadratically dependent on the light intensity, fluorescence is generated only at the focal volume of a pulsed femtosecond laser, where the photon density is the highest and is able to drive nonlinear absorption of photons [7]. This provides intrinsic optical sectioning, in where scattered excitation light cannot effectively generate fluorescence (Fig 3.2). Based on this principle, any emission signal can be attributed to the location of the laser focus. Therefore, the laser focus is the scanned in three dimensional raster fashion creating an image volume generated voxel-by-voxel.

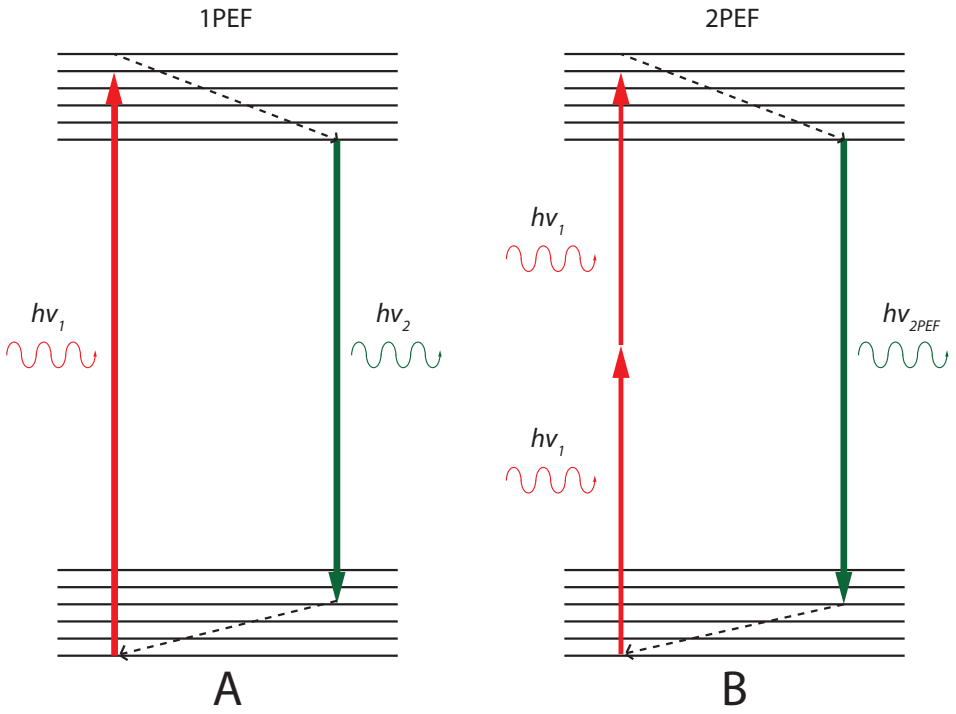

Figure 3.1 Jablonski diagram showing the interaction of multiple infrared photons with the electronic and vibrational energy levels of a molecule.

(A) Schematic of the linear excitation of a fluorescent molecule. In this case, one photon is absorbed and the fluorescent molecule is driven to an excited state. The molecule then relaxes and loses energy in the form of an emitted photon. (B) In two-photon excitation fluorescence (2PEF), the molecule absorbs two infrared photons that promote it to the excited electronic state. After relaxation to a lower vibrational level, the molecule emits a lower energy (red-shifted) photon.

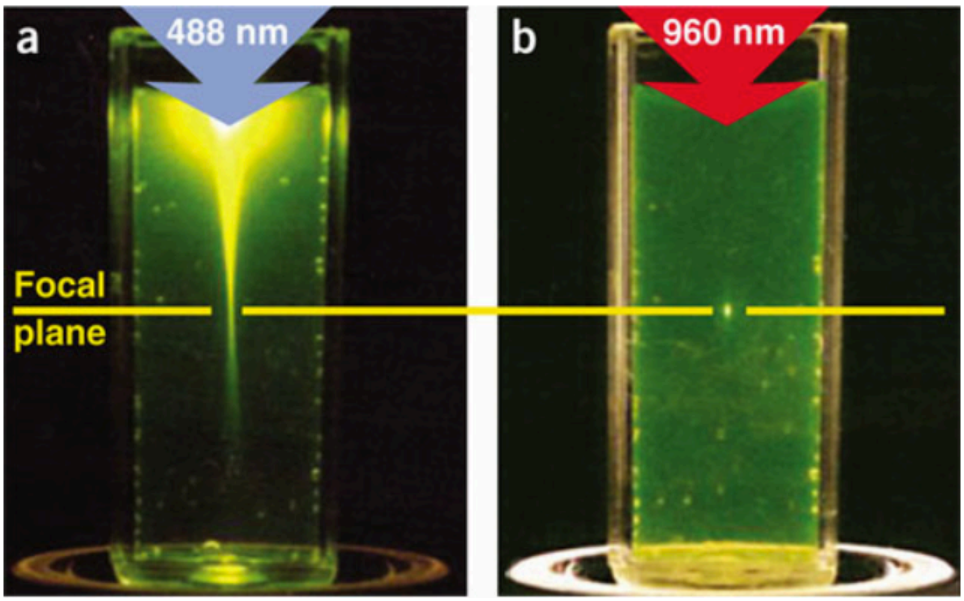

Figure 3.2 Localization of Excitation by Two-Photon Excitation.

(a) Single-photon excitation of fluorescein by focused 488-nm light. (b) Two-photon excitation using focused femtosecond pulses of 960-nm light. Reprinted by permission from Nature Publishing Group: Nature Biotechnology, Zipfel,W.R., Williams R.M., and Webb W.W. Nonlinear magic: multiphoton microscopy in the biosciences, 21, 1369 – 1377, Copyright 2003. [7]

3.2 Three-Photon Microscopy (3PM)

The first demonstration of 3PM was in the 1990s, with the purpose of extend the spectral range of the excitation source (e.g., access the transition band from 230 to 300 nm using a mode-locked Titanium:Sapphire laser) [8-10] . One of the main advantages of 3PM is the significant improvement in the overall excitation localization [8]. The fluorescence of 2PEF falls off as ~ $1/z^2$ while in the 3PM falls off as ~ $1/z^4$ (where z is the distance away from the focal plane). Therefore, improves the SBR by orders of magnitude when

compared to 2PEF (Fig 3.3) [2]. In conclusion, 3PM is an improve of the 2PM system, by reducing the SBR allowing us to penetrate deeper in to the scattered sample.

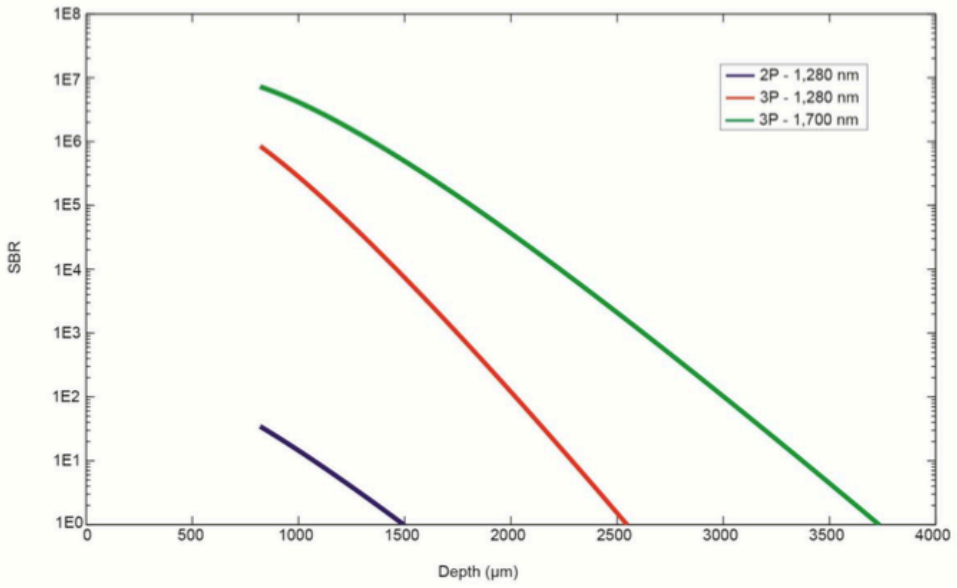

Figure 3.3 Comparing SBRs in 2PM and 3PM. Calculated SBRs of 2PM and 3PM at *NA*=. The effective attenuation lengths are 285 μm and 400 μm for excitation at 1,280nm and 1,7000 nm, respectively. Reprinted by permission from Nature Publishing Group: Nature Photonics, Horton, N.G., *et al*. In vivo three-photon microscopy of subcortical structures within an intact mouse brain, **7**, 205-209, Copyright 2013. [2]

3.3 Harmonic Generation

Another properties from the nonlinear imaging systems include second and third harmonic generation (SHG and THG), which produce detectable signals without the introduction of fluorescence dyes. During this process the molecules are not excited to a higher energy state by the absorption of photons. Instead, photons with the same

frequency are combined once they interact with the sample, generating new photons with twice energy, twice the frequency and half the wavelength on the initial photons [11,12] (Fig. 3.4). In order to generate SHG signal the molecules should maintain two physical properties: lack of inversion symmetry and be regularly oriented. One such structure is collage, which is present in most load-bearing tissue. This modality has been used for studies of the cornea, lamina cribrosa sclerae, or extracellular matrix, which consist primarily of collagen [13-15].

Unlike SHG, in order to generate the THG signal the molecules does not require the need for lack of inversion symmetry. Instead the THG is generated at the interface between materials of different excitability. THG microscopy has been used for studies of the myelin sheets, cell embryos, cardiomyocytes and lipids bodies in plants, where the lipid layer are separated by water [16-21].

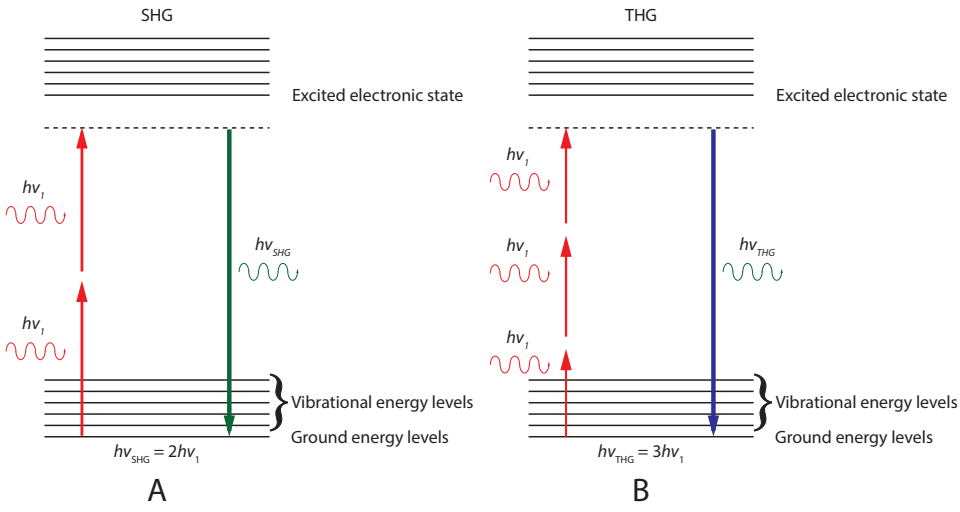

Figure 3.4 Jablonski diagram showing the interaction of multiple infrared photons with the electronic and vibrational energy levels of a molecule. (A) In second

harmonic generation (SHG), two infrared photons are instantaneously upconverted to a single photon of twice the energy. (B) In third harmonic generation (THG), three infrared photons are instantaneously upconverted to a single photon of thrice the energy.

3.4 The significance of Non-Linear Optical Imaging

Over the last two decades laser scanning microscopy (NLSM) or multi-photon microscopy (MPM) has become the most popular optical imaging modality to perform *in vivo* experiments, based on its advantages for three-dimensional imaging. In particular, 2PM and 3PM excitation excels at imaging of living cells, especially within scatter tissues such as brain, spinal cord, heart, whole organs, and even entire animals. They are a number of advantages that MPM offers in comparison with the usual one photon microscopy for conduct *in vivo* experiments. First, the near-infrared excitation light employed in MPM suffer less scattering by the sample when compared with the UV or blue-green light used in one-photon imaging system. Biological tissue is considered as non-uniform medium having multiple indexes of refraction. Whereby, longer scattering length allows reaching deeper imaging volume, before the path of signal photons from the sample toward the detector get disrupted. The narrow localization of MPM to the illumination focal point is the basis for the technique's most significant advantages over linear microscopy. In confocal microscopy, confocality is achieves with the implementation of a pinhole aperture, which reject the out-of focus light. However, under deep volumes scattering of the emitted photons is inevitable, resulting in significant loss of signal at the pinhole aperture. By contrast, MPM only excites the sample at the focal plane, and since no background fluorescence is produced, providing an optical sectioning

without the needs of spatial filters [22]. A third factor is based on the nature of MPM which eliminate the out-of-focus absorption reducing the photo-bleaching and photo-damage of the sample, given that the conditions for absorption are not met outside of the focal plane in comparison with linear microscopy which illuminates the sample with a double inverted cone of light.

3.5 2PM Experimental Setup

The overall microscope can be broken down into excitation optics, detection optics, and detection electronics. Each of these categories can be broken down further into components. Below we address the important components. The microscope design for the 3PM is presented in Chapter 6. This section was adapted from Steve Tilley honor thesis.

Laser

In order to achieve the intensity necessary for 2-photon absorption, we need relatively high peak intensity laser (Fig 3.5, a). In order to maintain a relatively low average power so as not to damage our sample, a pulse laser is used. We use the Chameleon from Coherent. With this laser, it is exceptionally easy to change excitation wavelength, which is non-trivial on older lasers.

Beam expanding telescope

This is a simple telescope used to expand the beam of the laser (Fig 3.5, b-c). The beam is expanded so that 80% of the power is clipped on the scan mirrors. This ensures that the objective is being properly filled without clipping too much light.

Power Control

The excitation laser power is controlled using a half wave plate and a beamsplitter cube[23]

(Fid 3.5, d-e). The half wave plate can be rotated to change the polarization of the laser light. The beamsplitter cube reflects light of one polarization and transmits light of an orthogonal polarization. Therefore, rotating the beamsplitter cube changes the fraction of the light that is transmitted through the cube, and thus the power of the excitation light that reaches the sample. The half wave plate is mounted on a rotatable mount from Newport, which is rotated using a servo [23].

Scan Mirrors

The laser must be aligned so the beam hits the scan mirrors straight and level (Fig 3.5, f). The control boards for the scan mirrors were mounted in an aluminum box and wired to a power supply. The control boards take an input voltage and convert it to a mirror position. To prevent the mirrors from overheating, they were mounted on a block that was constantly cooled with water. The scan mirrors we used were from Cambridge Technology (6215HM40B).

Scan and Tube Lens

The purpose of the scan and tube lens is to image the scan mirrors on to the back aperture of the objective (Fig 3.5, g-h). This ensures that the angle of light caused by the mirrors directly maps to the angle entering the objective, without causing the beam location on the back aperture to shift. The scan and tube lenses have two other functions: they expand the beam to alter the fraction of the back aperture that is filled, and they alter the ratio of the angle of light at the scan mirror to the angle of light at the back aperture. The focal lengths of the scan and tube lenses are 75 and 300 mm, respectively.

Detection Optics

The basic detection setup (Fig 3.6). A primary dichroic, with a cutoff wavelength of 705

nm, splits the emitted light from the excitation light, and is the first optic after the objective (Fig 3.6, b). A 2 inches lens with a focal length of 200 mm is then used to limit the spreading of the light from the optical axis (Fig 3.6, c). This allows there to be enough room to add the dichroics (Fig 3.6, d-e) before the condenser focuses the light onto the PMT. The condenser is a 3 pieces compound lens, made from 75 mm diameter optics. The first is a spherical lens with focal length of 75 mm (Fig 3.6, f), the second is an asphere with a focal length of 60 mm (Fig 3.6, g), and the third is a flat piece of glass, which serves to delay the refraction at the glass/air interface by an inch (Fig 3.6, h). In front of the PMT is a bandpass filter (Fig 3.6, i) to select the wavelength of that channel.

Preamplifier

The purpose of the preamplifier is to convert the current signal coming from the PMT to a voltage signal, while also amplifying and low pass filtering the signal. The circuit used was designed in the Kleinfeld Lab [23]. For this microscope, the circuit was placed on custom printed circuit boards. This allowed for easier construction, and should allow for easier maintenance in the future.

Stage

We used the following stages.

X/Y: Newport ILS100CC

Z: Newport GTS30V

In our microscopes, image translation was achieved by moving the sample, not the objective. These stages allow for a resolution of 0.5 μm in X/Y and 0.05 μm in Z.

Data acquisition board

All of our microscopes use the National Instruments PCI 6110 data acquisition board.

This board acquires all four analog imputs, controls the two analog outputs for the scan mirrors, controls the power control with a counter [23] and controls the shutter with a digital I/O port.

Power Box

The power box takes inputs from a power supply and routes it to the preamplifiers and PMTs. The power to the preamplifiers is just passed through, as both take ±15 volts. The PMTs, on the other hand, take an input of 15 volts, ground, and gain, where gain is between 0 and 0.9 volt. The PMTs output a reference voltage of 1.2 volts. A variable voltage divider using a potentiometer (pot) is used to drop these 1.2 volts down to anywhere between 0 and 0.9 volts by adjusting the pot. The system was designed so that dangerous voltages (>1) could not be reached. The 15 volts to the PMT is controlled by a switch, which illuminates when power is being supplied, so that a user can easily tell when the PMTs are on. This is important to help minimize the risk of someone exposing a powered PMT to excessive light.

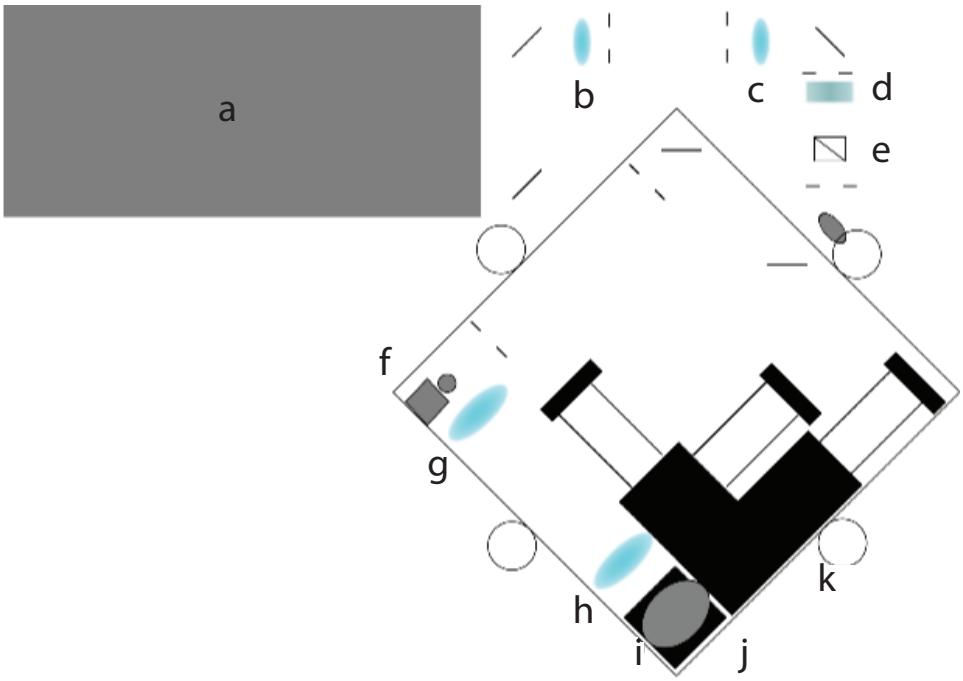

Figure 3.5 Representative schematic of microscope from above.

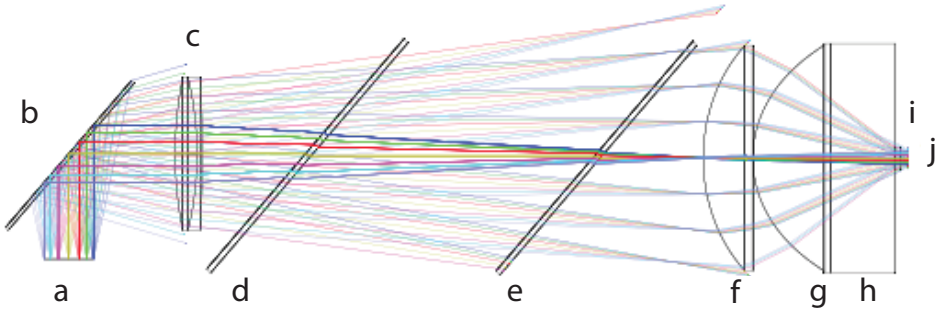

Figure 3.6 ZEMAX ray trace of optics design.

References

1. J. N. D. Kerr, W. Denk, Imaging in vivo: watching the brain in action. Nat Rev Neurosci 9, 195 (Mar 1, 2008).
2. N. G. Horton, K. Wang, D. Kobat, C. G. Clark, F. W. Wise, C. B. Schaffer, and C. Xu, "In vivo three-photon microscopy of subcortical structures within an intact mouse brain," Nat. Photon. **7**, 205-209 (2013).
3. D. Kobat et al., Deep tissue multiphoton microscopy using longer wavelength excitation. Opt Express 17, 13354 (Aug 3, 2009).
4. M. Garcia-Alloza, B. J. Bacskai, Techniques for brain imaging in vivo. Neuromolecular Med 6, 65 (Jan 1, 2004).
5. W. Denk, J. H. Strickler, and W. W. Webb, "Two-photon laser scanning fluorescence microscopy," Science 248, 73-76 (1990).
6. Emily A. Gibson, Omid Masihzadeh, Tim C. Lei, David A. Ammar, and Malik Y. Kahook, "Multiphoton Microscopy for Ophthalmic Imaging," *Journal of Ophthalmology*, vol. 2011, Article ID 870879, 11 pages, 2011. doi:10.1155/2011/870879
7. W. Zipfel, R. Williams, W. Webb, Nonlinear magic: multiphoton microscopy in the biosciences. Nat Biotechnol 21, 1369 (Nov 1, 2003).
8. Xu, C., Zipfel, W., Shear, J.B., Williams, R.M. & Webb, W.W. Multiphoton fluorescence excitation: new spectral windows for biological nonlinear microscopy. Proc. Natl. Acad. Sci. U. S. A. 93, 10763-10768 (1996).
9. Hell, S.W. et al. Three-photon excitation in fluorescence microscopy. J. Biomed. Opt. 1, 71-74 (1996).

10. Wokosin, D.L., Centonze, V.E., Crittenden, S. & White, J. Three-photon excitation fluorescence imaging of biological specimens using an all-solid-state laser. Bioimaging 4, 208-214 (1996).
11. Zipfel WR, Williams RM, Christie R, Nikitin AY, Hyman BT, Webb WW. Live tissue intrinsic emission microscopy using multiphoton-excited native fluorescence and second harmonic generation. P Natl Acad Sci USA 2003; 100(12):7075-7080.
12. Barad Y, Eisenberg H, Horowitz M, Silberberg Y. Nonlinear scanning laser microscopy by third harmonic generation. Appl Phys Lett 1997; 70(8):922-924.
13. Han, M; Giese, G; Bille, J (2005). "Second harmonic generation imaging of collagen fibrils in cornea and sclera". Optics Express. 13 (15): 5791–7.
14. Brown, Donald J.; Morishige, Naoyuki; Neekhra, Aneesh; Minckler, Don S.; Jester, James V. (2007). "Application of second harmonic imaging microscopy to assess structural changes in optic nerve head structure ex vivo". Journal of Biomedical Optics. 12 (2): 024029.
15. Williams RM, Zipfel WR, Webb WW. Interpreting second-harmonic generation images of collagen I fibrils. Biophys J 2005; 88(2):1377-1386.
16. M. J. Farrar, F. W. Wise, J. R. Fetcho, and C. B. Schaffer, “In vivo imaging of myelin in the vertebrate central nervous system using third harmonic generation microscopy,” Biophys. J. **100**, 1362-1371 (2011).
17. SW Chu, SY Chen, TH Tsai, TM Liu, CY Lin, HJ Tsai, and CK Sun. In vivo developmental biology study using noninvasive multi-harmonic generation microscopy. *Opt Express*, 11:3093–3099, 2003.
18. CK Sun, SW Chu, SY Chen, TH Tsai, TM Liu, CY Lin, and HJ Tsai. Higher

harmonic generation microscopy for developmental biology. *Journal of structural biology*, 147(1):19–30, 2004.

19. V Barzda, C Greenhalgh, JA der Au, S Elmore, JHGM van Beek, and J Squier. Visualization of mitochondria in cardiomyocytes by simultaneous harmonic generation and fluorescence microscopy. *Appl Phys Lett*, 79(24):4045–4047, 2001.
20. D De´barre, W Supatto, AM Pena, A Fabre, T Tordjmann, L Combettes, MC Schanne-Klein, and E Beaurepaire. Imaging lipid bodies in cells and tissues using third-harmonic generation microscopy. *Nat Meth*, 3(1):47–53, 2005.
21. M Müller, I Squier, KR Wilson, and GI Brakenhoff. 3D microscopy of transparent objects using third-harmonic generation. *Journal of Microscopy*, 191:266–274, 1998.
22. Centonze VE, White JG (1998) Multiphoton Excitation Provides Optical Sections from Deeper within Scattering Specimens than Confocal Imaging. *Biophysical Journal* 75(4):2015–2024.
23. Quoc-Thang Nguyen, Philbert S. Tsai, and David Kleinfeld. Mpscope: A versatile software suite for multiphoton microscopy. *Journal of Neuroscience Methods*, 156(1-2):351 – 359, 2006.

CHAPTER 4

CAPILLARY OCCLUSIONS REDUCE CORTICAL BLOOD FLOW AND IMPAIR MEMORY IN ALZHEIMER'S MOUSE MODELS

4.1 ABSTRACT

Cerebral blood flow (CBF) is reduced in Alzheimer's disease (AD) patients and related mouse models, but the underlying mechanisms and the resulting impacts on cognitive function and AD pathogenesis remain poorly understood. In the APP/PS1 mouse model of AD we found that an increased number of cortical capillaries were stalled as compared to wild type animals, largely due to leukocytes that adhered in capillary segments and blocked blood flow. Administration of antibodies against the neutrophil marker Ly6G reduced the number of stalled capillaries, leading to an immediate increase in CBF and to rapidly improved performance in spatial and working memory tasks. Increasing CBF by preventing the leukocyte adhesion that plugs capillaries may provide a novel strategy for improving cognition in AD.

4.2 MAIN TEXT

Patients with Alzheimer's disease (AD) *(1-3)* and mice expressing mutated forms of amyloid precursor protein (APP) *(4-6)* exhibit cortical cerebral blood flow (cCBF) reductions of ~25% early in disease development. Cognitive function was impaired by CBF reductions of ~20% in healthy humans *(7)* and wild type (wt) mice *(8),* suggesting that the decreased CBF in AD likely contributes to cognitive dysfunction. To investigate cortical hypoperfusion in AD, we used *in vivo* two-photon excited fluorescence (2PEF)

microscopy to image the cortical vasculature in APP/PS1 mice *(9)* (Fig. 4.1A) and looked for occluded vessels (Fig. 4.1B). We observed no obstructions in arterioles or venules, but APP/PS1 mice had a 4-fold elevation in the number of capillaries with stalled blood flow as compared to age- and sex-matched, wt littermates (Fig. 4.1C, movie S1 and S2). The number of stalled capillaries was elevated by 12 weeks of age in APP/PS1 mice, and remained elevated throughout disease progression (Fig. 4.1D). Flowing and stalled capillaries (Fig. 4.1E) had about the same distance distribution relative to the nearest penetrating arteriole (Fig. 4.1F) or ascending venule (Fig. 4.1G). The incidence of capillary stalling did not increase with Aβ plaque density (fig. 4.S1), and was the same in awake and anesthetized animals (movie 3 and S4; fig. 4.S2). Capillary stalling was similarly elevated in TgCRND8 mice, a different mouse model of APP overexpression (fig. 4.S3) *(10)*.

Because each occluded capillary decreases blood flow in downstream vessels *(11)*, a small number of stalled capillaries could have an outsized impact on CBF. We simulated blood flow in vascular networks from a 1 mm^3 volume of mouse parietal cortex (Fig. 4.1H) *(12)*, a 6 mm^3 volume of human cortex (Fig. 4.1I) *(13)*, and a synthetic periodic network of order three (fig. 4.S4) using a non-linear model of microvascular blood flow *(14)* (see Supplementary Text). cCBF decreased linearly with an increasing fraction of stalled capillaries, with the same slope and without any threshold effect, across all three networks (Fig. 4.1J), suggesting that capillary stalling may impact CBF in humans and mice similarly. These simulations predicted a ~5 % deficit in cCBF due to 2% of capillaries stalled.

Using labeling strategies to distinguish leukocytes, platelets, and RBCs (Fig. 4.2A), we found the majority of stalled capillary segments contained a leukocyte (Fig. 4.2B). Stalled capillaries had a modestly smaller average diameter than flowing capillaries (Fig. 4.2C), but no difference in the density of nearby Aβ deposits (Fig. 4.2D). Most plugged capillaries were transiently stalled with a half-life of less than 5 min, while one-third remained stalled for 15 min and 10% began flowing and then re-stalled within 15 min (Fig. 4.2E; fig. 4.S5). We also observed that some capillary segments alternated between flowing and stalled in repeated imaging sessions over weeks (Fig. 4.2F). The same capillaries were stalled across multiple imaging sessions about ten times as frequently as predicted by a model that assumed each capillary had an equal probability of being stalled at any time point (Fig. 4.2G). Taken together, these data suggest that the capillary stalls were caused by leukocytes adhering in a distinct subset of capillary segments.

To determine the class of leukocyte causing the capillary stalls, we injected fluorescently-labeled antibodies against Ly6G (α-Ly6G; 4 mg/kg animal weight), a neutrophil surface marker, and serendipitously found that this reduced the number of stalled capillaries within 10 min (Fig. 4.3A and fig. 4.S6). Isotype control (Iso-Ctr) antibodies did not impact capillary stalling. The rapid resolution of the capillary stalls suggests that α-Ly6G interfered with leukocyte adhesion. Median volumetric blood flow in penetrating arterioles, measured using 2PEF (Fig. 4.3B), increased by 26% in young (3-4 months) and 32% in aged (11-14 months) APP/PS1 mice one hour after α-Ly6G administration (Fig. 4.3C). This increase in blood flow was due to an increase in RBC speed and not an

increase in vessel diameter (fig. 4.S7). Penetrating arterioles with lower baseline flow tended to show larger flow increases (fig. 4.S8). Iso-Ctr antibodies did not change blood flow in APP/PS1 mice, nor did α-Ly6G in wt animals (Fig. 4.3C). Further, capillary stalling decreased and penetrating arteriole flow increased one day after administration of antibodies against LFA-1, which depleted circulating leukocytes (fig. 4.S9). Across all antibody and control treatments, penetrating arteriole flows increased (decreased) when the number of stalled capillaries decreased (increased) (fig. 4.S10). We also used arterial spin labeled MRI (ASL-MRI) to measure cCBF in 7-9-month old animals (Fig 4.3D). At baseline, average cCBF in APP/PS1 mice was 17% lower than in wt animals (Fig. 4.3E). cCBF increased by 13% in APP/PS1 mice at ~5 hr after α-Ly6G administration, recovering about two-thirds of the deficit relative to wt animals, but was unchanged in APP/PS1 mice given Iso-Ctr antibodies or wt mice given α-Ly6G (Fig. 4.3E). Thus, administration of α-Ly6G led to a rapid increase in cCBF in APP/PS1 mice that exceeded the flow improvement predicted by our simulations after elimination of capillary stalls.

We next tested whether α-Ly6G administration improves cognitive function in APP/PS1 mice (Fig. 4.4A). In the object replacement (OR) test of spatial short-term memory (Fig. 4.4B), a single dose of α-Ly6G in ~11-month old APP/PS1 mice improved performance to the level of wt animals at 3 and 24 hours after administration (Fig. 4.4C; fig. 4.S11). APP/PS1 mice treated with Iso-Ctr antibodies showed no change, nor did wt animals with α-Ly6G (Fig. 4C). Similarly, α-Ly6G improved performance of APP/PS1 mice in the Y-maze test of working memory (Fig. 4.4D; fig. 4.S12). We detected no improvement in sensory-motor function (balance beam walk, fig. 4.S13) and a trend toward reduced depression- and anxiety-like behavior (forced swim, fig. 4.S14) in APP/PS1 mice with α-

Ly6G. We continued to treat these animals with α-Ly6G every three days for a month, resulting in depletion of neutrophils (fig. 4.S15). After this regimen, APP/PS1 mice exhibited short-term memory performance that matched wt animals in OR (Fig. 4.4C), Y-maze (Fig. 4.4D), and novel object recognition (NOR) (Fig. 4.4E; fig. 4.S16). We saw no improvement in sensory-motor function (fig. 4.S13) and a trend toward decreased depression- and anxiety-like behavior (fig. 4.S14).

Because one of the clearance pathways for Aβ is through the vasculature *(15)* we assessed whether improving cCBF with α-Ly6G decreases the concentration of Aβ monomers and aggregates. Using enzyme-linked immunosorbent assays (ELISAs) of brain extracts from the animals that received one month of antibody treatment, we found that α-Ly6G reduced the concentration of $A\beta_{1\text{-}40}$ compared to Iso-Ctr antibodies (Fig. 4.4F), while the concentration of $A\beta_{1\text{-}42}$ (Fig. 4.4F) and aggregates of Aβ (fig. 4.S17D) remained unchanged. We saw no difference in the number and density of Aβ plaques between α-Ly6G and Iso-Ctr treated animals (fig. 4.S17).

Brain blood flow reductions occur early in disease development for both AD patients *(1, 16)* and for mouse models that express mutant APP *(4-6)*. Proposed mechanisms for this hypoperfusion include constriction of brain arterioles (*17*), loss of vascular density *(18)*, and changes in neural activity patterns *(19)* or in neurovascular coupling *(20, 21)*. Our data reveal that neutrophil adhesion to the capillary endothelium may be previously-unrecognized mechanism for the flow reduction. Capillary obstructions, often linked to tissue inflammation, have been observed in a variety of organ systems (typically at higher

incidence than observed here) and contribute to pathology *(22-28)*. Indeed, Aβ-induced vascular inflammation *(29, 30)* is a likely cause of the capillary stalling we observed. The rapid resolution of the capillary stalls after α-Ly6G treatment suggests the stalls are caused by receptor-mediated interactions of neutrophils with the capillary endothelium *(31)*. Our observation that some capillary segments were more likely to stall suggests that the vascular inflammation is not uniform. Increased leukocyte adherence likely causes not only stalls, but also slowed flow in some capillary segments, which was not taken into account in our simulations and likely contributes the model's underestimation of the increase in CBF after α-Ly6G administration. However, the simulations predicted a similar sensitivity of brain blood flow to capillary stalling in humans and mice, suggesting that, if capillary stalling occurs in AD patients, significant blood flow improvements could be achieved. Spatial and working memory improved after increasing blood flow in APP/PS1 mice on a time scale that was too fast for significant neuronal plasticity or synaptic remodeling, suggesting that a mismatch between neuronal energy metabolism and delivery of energy substrates through blood flow contributes to the cognitive deficit. We, and others *(32)*, have also observed improved cognitive function after extended treatment with antibodies that deplete neutrophils. The previous study used different AD mouse models (3xTg and 5xFAD) and different antibodies (α-GR-1, α-LFA-1) than used here and suggested that inhibition of neutrophil trafficking into the brain contributed to the cognitive benefits *(32)*. We have shown that such neutrophil depletion also increases brain blood flow, which may also have contributed to the cognitive improvements in this previous work. Improving CBF by interfering with neutrophil adhesion may be a novel therapeutic approach for AD.

4.3 RESULTS

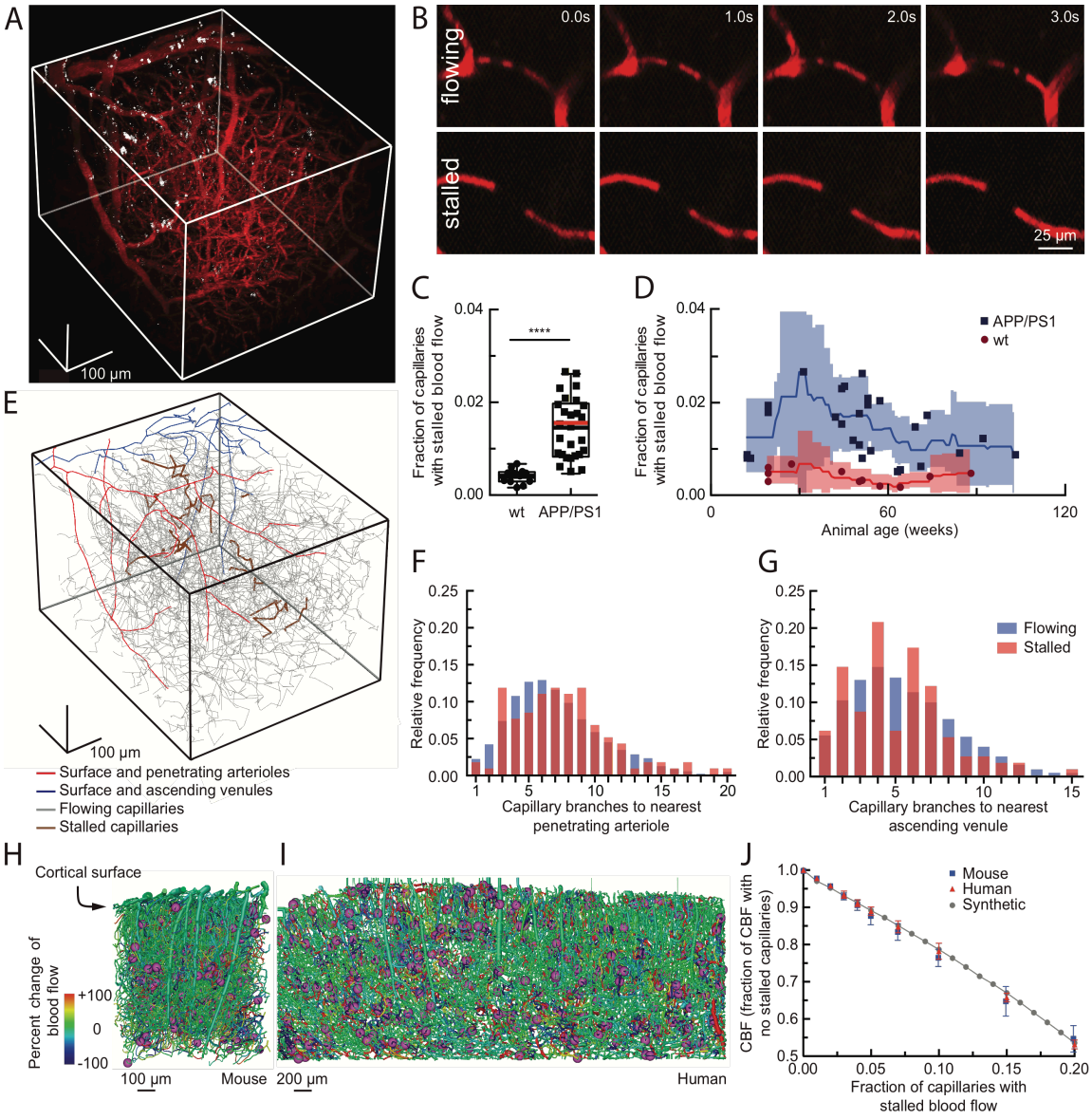

Fig. 4.1 2PEF imaging of mouse cortical vasculature revealed a higher fraction of plugged capillaries in APP/PS1 mice, which simulations predicted would decrease cCBF. (A) Rendering of 2PEF image stack of cortical vasculature (red; Texas Red dextran) and amyloid deposits (white; methoxy-X04). (B) Individual brain capillaries were scored as flowing or stalled based on the motion of unlabeled blood cells (black)

within the fluorescently labeled blood plasma (red). (C) Fraction of capillaries with stalled blood flow in APP/PS1 and wt mice; (D) same data as a function of age. One outlier not shown: APP/PS1, 42 weeks, 4.4% stalled. (E) Tracing of the vascular network in panel A, with stalled capillaries indicated in brown. (F) and (G) Histograms showing the topological location of flowing and stalled capillaries relative to the nearest penetrating arteriole and ascending venule, respectively. (H) and (I) Spatial maps of simulated blood flow changes caused by stalling of 2% of capillaries (indicated by purple spheres) in an mouse cortical vascular network (H, from *(33)*), and a human network (I, from *(13)*) (J) Normalized cortical perfusion as a function of the fraction of capillaries that were occluded, expressed as a fraction of the perfusion with no occlusions, in mouse, human, and synthetic networks.

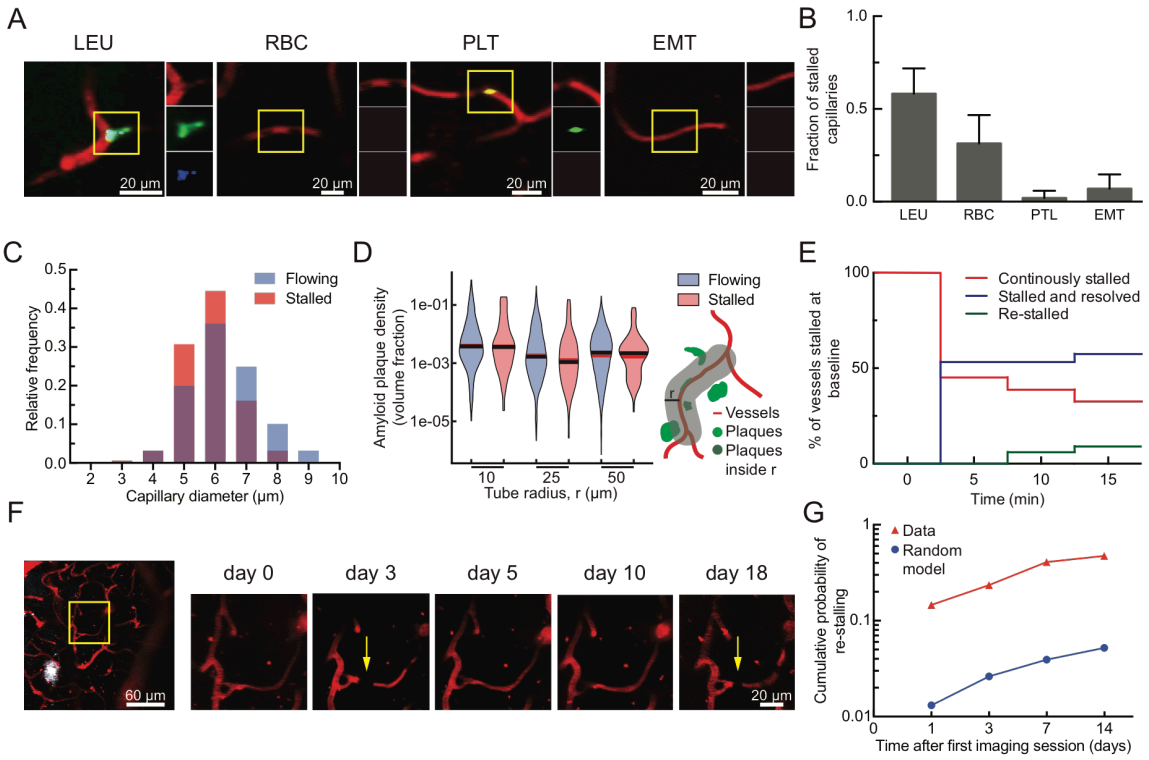

Fig. 4.2 Characterization of the cause, location, and dynamics of capillary occlusions in APP/PS1 mice. (A) 2PEF images of capillaries stalled by a leukocyte (LEU), RBCs, and platelet aggregates (PLT), or found empty of blood cells (EMT), distinguished by fluorescent labels (red: Texas Red-labeled blood plasma; green: rhodamine 6G-labeled leukocytes and platelets; blue: Hoechst-labeled leukocyte nuclei). (B) Fraction of stalled capillaries stalled by LEU, RBC, PLT, or EMT. (C) Histogram of the diameter of flowing and stalled capillaries (Averages: 5.8±0.05 µm (stalled), 6.3±1.1 µm (flowing); $p<0.0001$). (D) Violin plot of the density of amyloid deposits within tubes of different radii that followed the capillary centerline for flowing and stalled capillary segments. (E) Fraction of stalled capillaries that remained stalled (red), resumed flowing (green), or resumed flowing and then re-stalled (blue) over 15 minutes. (F) 2PEF images of the same capillary alternately stalled (arrows) and flowing (white: methoxy-X04). (G) Cumulative

probability of an initially stalled capillary to be observed stalled again at any subsequent imaging time point, showing both real observations and predictions from a model that assumed each capillary had an equal probability of stalling at each time point.

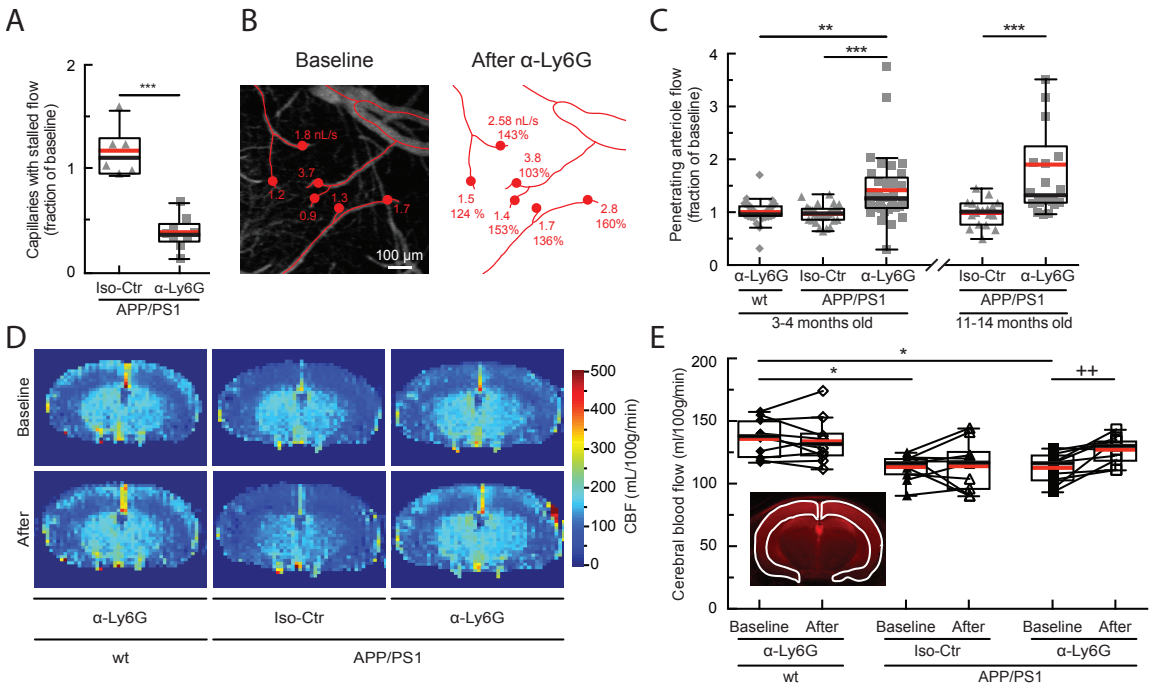

Fig. 4.3 Administration of antibodies against Ly6G reduced the number of stalled capillaries and increased cCBF in APP/PS1 mice. (A) Number of capillaries with stalled blood flow ~1 hr after α-Ly6G or Iso-Ctr antibody administration shown as a fraction of the number of stalled capillaries at baseline. (B) Projection of 2PEF image stack of brain surface vasculature, with surface (red lines) and penetrating (red dots) arterioles identified. For each penetrating arteriole, volumetric blood flow is indicated at baseline (left) and after α-Ly6G administration (right), along with the percentage of baseline flow. (C) Volumetric blood flow in penetrating arterioles measured 60-90 min

after α-Ly6G or Iso-Ctr antibody administration in young and old APP/PS1 mice and wt control animals shown as a fraction of baseline arteriole flow. (D) CBF map measured using ASL-MRI at baseline and ~5 hr after administration of α-Ly6G or Iso-Ctr antibodies in APP/PS1 and wt mice. (E) cCBF measurements (ASL-MRI, inset indicates ROI on T2 MRI image) at baseline and ~5 hr after administration of α-Ly6G or Iso-Ctr antibodies in APP/PS1 and wt mice.

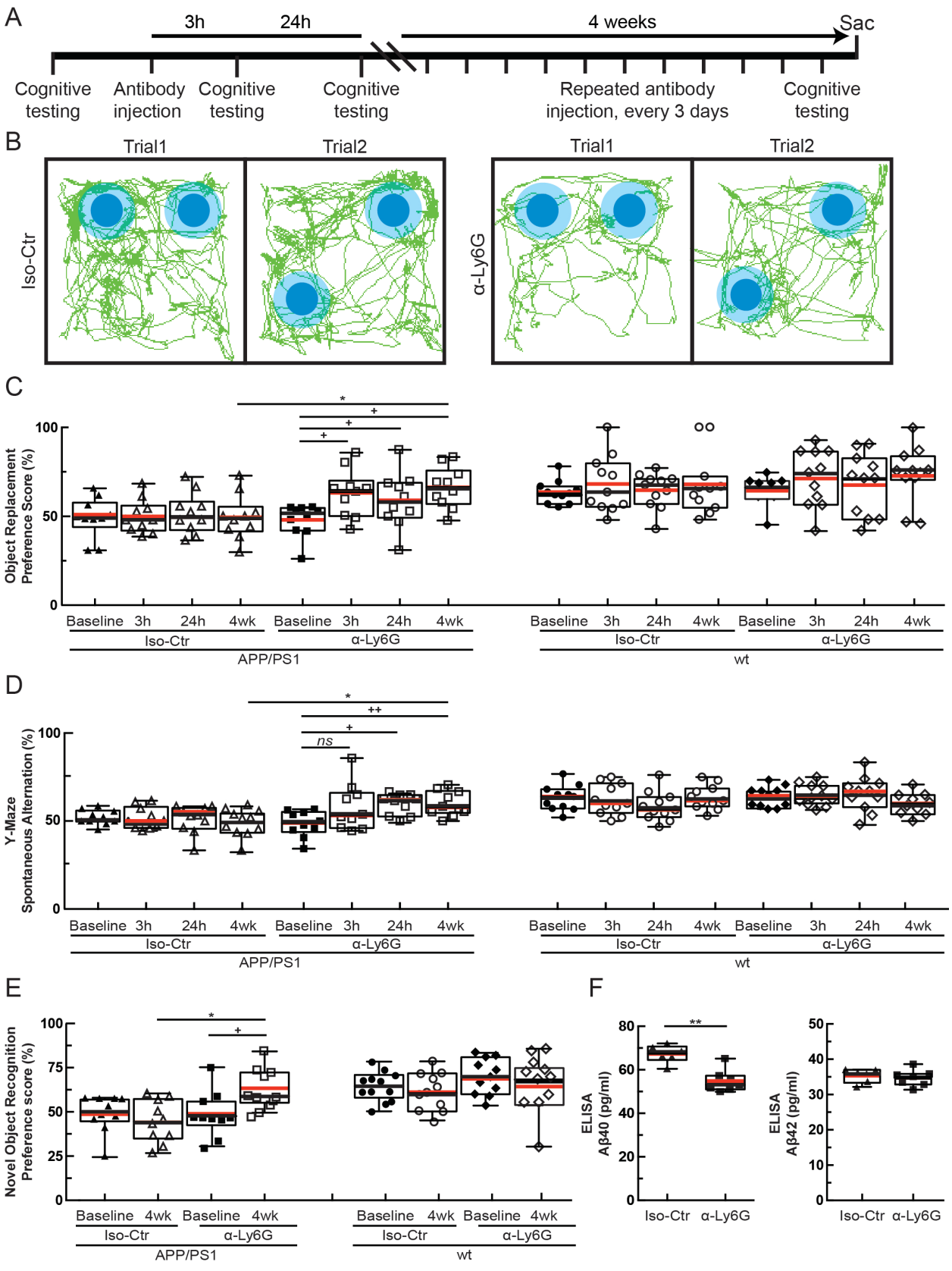
A
3h
24h
4 weeks
Sac
Cognitive testing
Antibody injection
Cognitive testing
Cognitive testing
Repeated antibody injection, every 3 days
Cognitive testing
B
Trial1
Trial2
Trial1
Trial2
Iso-Ctr
α-Ly6G
C
Object Replacement Preference Score (%)
100
50
0
Baseline 3h 24h 4wk Baseline 3h 24h 4wk
Iso-Ctr
α-Ly6G
APP/PS1
Baseline 3h 24h 4wk Baseline 3h 24h 4wk
Iso-Ctr
α-Ly6G
wt
D
Y-Maze Spontaneous Alternation (%)
100
50
0
ns
Baseline 3h 24h 4wk Baseline 3h 24h 4wk
Iso-Ctr
α-Ly6G
APP/PS1
Baseline 3h 24h 4wk Baseline 3h 24h 4wk
Iso-Ctr
α-Ly6G
wt
E
Novel Object Recognition Preference score (%)
100
75
50
25
0
Baseline 4wk Baseline 4wk
Iso-Ctr
α-Ly6G
APP/PS1
Baseline 4wk Baseline 4wk
Iso-Ctr
α-Ly6G
wt
F
ELISA Aβ40 (pg/ml)
80
60
40
20
0
Iso-Ctr α-Ly6G
ELISA Aβ42 (pg/ml)
50
40
30
20
10
0
Iso-Ctr α-Ly6G

Fig. 4.4 Administration of α-Ly6G improved short-term memory and decreased the concentration of Aβ1-40 in APP/PS1 mice. (A) Experimental timeline for behavioral studies. (B) Tracking of mouse nose location from video recording during training and trial phases of OR task taken 3-5 hr after administration of α-Ly6G or Iso-Ctr antibodies in APP/PS1 mice. (C) Preference score in OR task and (D) spontaneous alternation in Y-maze task for APP/PS1 and wt mice at baseline and at 3 hr and 24 hr after a single administration of α-Ly6G or Iso-Ctr antibodies, and after 4 weeks of treatment every three days. (E) Preference score in NOR task for APP/PS1 and wt mice at baseline and after 4 weeks of treatment every three days. (F) ELISA measurements of Aβ1-40 (left) and Aβ1-42 (right) monomer concentrations after 4 weeks of treatment every three days.

4.4 ACKNOWLEDGEMENTS

This work was supported by the National Institutes of Health grants AG049952 (CS), NS37853 (CI), and AG031620 (NN), the Alzheimer's Drug Discovery Foundation (CS), the Alzheimer's Art Quilt Initiative (CS), European Research Council grant 615102 (SL), the DFG German Research Foundation (OB), a National Science Foundation Graduate Research Fellowship (JCH), the L'Oréal Fellowship for Women in Science (NN), and used computing resources at CALMIP (SL). We thank Frédéric Lauwers for the human vascular data, Philibert Tsai, Pablo Blinder and David Kleinfeld for the mouse vascular data, and Maria Gulinello for guidance on behavior experiments. Finally, we thank Joseph R. Fetcho, Jesse H. Goldberg, and Michael I. Kotlikoff for commenting on the manuscript. The data reported in this manuscript are archived at **all data underlying these findings will be made publicly available at Cornell's eCommons online archive**

JCCH, OB, SL, NN, and CBS conceived the study. JCCH and CJK performed the *in vivo* imaging experiments. MHJ, GO and YK developed custom software for data analysis. OB conducted the behavioral studies. LP and CI conducted the ALS-MRI experiments. MB, MP, VD, AS, YD and SL performed the blood flow simulations. MCC and SS did the stall analyses in the TgCNRD8 mouse model. JCCH, OB, CJK, VM, LKV, II, YK, JZ, JDB, and ED contributed to the analysis of *in vivo* imaging experiments. JCCH, OB, NN and CBS wrote the paper with contributions from MHJ, MCC, LP, CI, and SL. All authors edited and commented on the manuscript.

4.5 MATERIALS AND METHODS

4.5.1 Animals and surgical preparation

All animal procedures were approved by the Cornell Institutional Animal Care and Use Committee and were performed under the guidance of the Cornell Center for Animal Resources and Education. We used adult transgenic mice (B6.Cg-Tg (APPswe, PSEN1dE9) 85Dbo/J) as a mouse model of AD *(34)* and littermate wild-type mice (C57BL/6) as controls (APP/PS1: RRID:MMRRC_034832-JAX, The Jackson Laboratory). Animals were of both sexes and ranged in age from 12 to 100 weeks.

For cranial window implantation, mice were anesthetized under 3% isoflurane on a custom-built stereotactic surgery frame and then maintained on ~1.5% isoflurane in 100% oxygen. Once unresponsive to a toe pinch, mice were given 0.05 mg per 100 g of mouse weight of glycopyrrolate (Baxter Inc.) or 0.005 mg/100 g of atropine (54925-063-10, Med-Pharmex Inc.) to prevent lung secretions, 0.025 mg/100 g of dexamethasone

(07-808-8194, Phoenix Pharm Inc.) to reduce post-surgical inflammation, and 0.5 mg/100 g of ketoprofen (Zoetis Inc.) to reduce post-surgical inflammation and provide post-surgical analgesia. Glycopyrrolate and ketoprofen were injected intramuscularly, while atropine and dexamethasone were injected subcutaneously. Bupivacaine (0.1 ml, 0.125%) (Hospira Inc.) was subcutaneously administered at the incision site to provide a local nerve block. Animals were provided 1 ml per 100 g of mouse weight of 5% (w/v) glucose in normal saline subcutaneously every hour during the procedure. We used a thermometer and feedback-controlled heating blanket (40-90-8D DC, FHC) to maintain body temperature at 37 °C. The head was shaved and washed 3 times with alternating 70% (v/v) ethanol and iodine solutions (AgriLabs). A 6-mm diameter craniotomy was performed over the cerebral cortex using a high-speed drill (HP4-917-21, Fordom) using bits with diameters of 1.4, 0.9, 0.7, and 0.5 mm (Fine Science Tools) for different steps in the craniotomy procedure. The craniotomy was then covered with a sterile 8-mm diameter glass coverslip (11986309, Thermo Scientific), glued onto the remaining skull with cyanoacrylate adhesive (Loctite) and dental cement (Co-Oral-Ite Dental). All procedures were done using sterile technique.

Once the craniotomy was completed, mice were returned to their cages and given injections of 0.025 mg/100 g of dexamethasone and 0.5 mg/100 g of ketoprofen subcutaneously 1 and 2 days after surgery, and all cages were placed over a heating pad during this period. Animals were given at least two weeks to recover from cranial window implantation before experimentation to minimize inflammation from the surgical procedure.

Cranial window implantations were also performed in TgCRND8 mice *(10)*. These animals were housed at The Rockefeller University's Comparative Biosciences Center and treated in accordance with IACUC-approved protocols. The window implantation followed the same protocol as described above, except that mice were anaesthetized using avertin (50 mg/100 g, intraperitoneal) and were given atropine (0.004 mg/100 g).

4.5.2 *In vivo* two-photon microscopy

During imaging sessions, mice were anesthetized with 3% isoflurane, placed on a custom stereotactic frame, and were given glycopyrrolate or atropine and glucose as described above. During imaging, anesthesia was maintained with ~1.5% isoflurane in 100% oxygen, with small adjustments to the isoflurane made to maintain the respiratory rate at ~1 Hz. The mouse was kept at 37 °C with a feedback-controlled heating pad (40-90-8D DC, FHC).

To fluorescently label the microvasculature, Texas Red dextran (40 μl, 2.5%, MW = 70,000 kDA, Thermo Fisher Scientific) in saline was injected retro-orbitally just prior to imaging. In some animals, amyloid beta (Aβ) deposits were labeled using methoxy-X04 *(35)*. In early experiments using methoxy-X04 obtained directly from Prof. Klunk at the University of Pittsburgh, we retro-orbitally injected 40 μL of 1 mg/ml methoxy-X04 in 0.9% saline (adjusted to pH 12 with 0.1 N NaOH) just prior to imaging. In later experiments using methoxy-X04 available commercially from Tocris, we intraperitoneally injected methoxy-X04 (dissolved in DMSO at 100 mM) one day prior to imaging at a dose of 1 mg/100 g. We observed no obvious differences in the amyloid

labeling between these two administration approaches. In some animals, leukocytes and blood platelets were labeled with a retro-orbital injection of Rhodamine 6G (0.1 ml, 1 mg/ml in 0.9% saline, Acros Organics, Pure) *(27)*. Leukocytes were distinguished from blood platelets with a retro-orbital injection of Hoechst 33342 (50 µl, 4.8 mg/ml in 0.9% saline, Thermo Fisher Scientific). Texas Red (and methoxy-X04, when given retro-orbitally) were dosed in a single syringe, while Rhodamine 6G and Hoechst were dosed together in a second syringe.

Three-dimensional images of the cortical vasculature and measurement of red blood cell flow speeds in specific vessels were obtained via a custom-built two-photon excited fluorescence (2PEF) microscope. Imaging was done using 830-nm, 75-fs pulses from a Ti:Sapphire laser oscillator (MIRA HP pumped by a Verdi-V18 or Vision S, Coherent) and 900-nm, 75-fs pulses from a second Ti:Sapphire laser oscillator (Vision S, Coherent). Lasers were scanned by galvonometric scanners (1 frame/s) and focused into the sample using a 20× water-immersion objective lens for high-resolution imaging (numerical aperture (NA) = 1.0, Carl Zeiss Microscopy; or NA = 0.95, Olympus), or a 4× objective for mapping of the cortical surface vasculature (NA = 0.28, Olympus). The emitted fluorescence was detected on either a two-channel detection system or, for later data sets, on an upgraded four-channel detection system. On the two-channel system, the fluorescence was split by a 600-nm long pass dichroic and two successive image stacks were acquired first with 645/45 nm (center wavelength/bandwidth) and 575/25 nm bandpass filters to image Texas Red and Rhodamine 6G, respectively, and then with 645/65 nm and 460/50 nm filters to image Texas Red and both methoxy-X04 and

Hoescht (on the same channel), all under 830-nm excitation. On the four-channel system, a secondary long-pass dichroic at 520 nm was followed by tertiary long-pass dichroics at 458 nm and one at either 562 or 605 nm. Emission was detected on four photomultiplier tubes through the following emission filters: 417/60 nm for Hoechst, 494/41 nm for methoxy-X04, 550/49 nm for Rhodamine 6G, and 641/75 nm for Texas Red. Laser excitation was 830 nm except when trying to image deep cortical tissue in animals where only Texas Red was present in which case 900-nm excitation was used. Laser scanning and data acquisition was controlled by ScanImage software *(36)*. To visualize the cortical vasculature, stacks of images spaced by 1 μm axially were taken to a cortical depth of 300-500 μm.

For TgCRND8 mice, imaging was performed using a Fluoview 1000MPE two-photon laser scanning microscope (Olympus) equipped with a SpectraPhysics MaiTai DeepSee laser and a 25x/1.05 NA objective at The Rockefeller University Bio-Imaging Resource Center.

4.5.3 Awake imaging

A subset of mice was imaged with 2PEF without anesthesia. During the craniotomy surgery, a 3D-printed skull-attached mounting frame was secured on top of the cranial window to allow for head fixation during anesthesia-free imaging. The 3D-printed frame was flanked by 4 screws (TX000-1-1/2 self tapping screws, Small Parts Inc., Miami Lakes, FL) inserted into the skull. The screws and appropriate parts of the frame were glued to the skull using Loctite and dental cement to firmly attach the mounting frame.

We adapted and modified the awake imaging system from Dombeck et al. *(37)*, in which a large (8 inch diameter) Styrofoam ball (Floracraft) was levitated using a thin cushion of air between the ball and a custom made (3D printed) casting containing eight 0.25 inch diameter air jets, arranged symmetrically. The air pressure was adjusted to just float the ball when the mouse was on top of it.

We trained mice to remain in a calm state during awake, head-fixed imaging. During the first training session, mice were handled, with the room lights on, by a trainer wearing gloves for ~10 min or until the mice routinely ran from hand to hand. The mice were then transferred to the ball and allowed to move freely for ~10 min with the room lights on while the handler rotated the ball to keep the mice centered near the top. The second training session consisted of again allowing the mice to move freely on the ball for ~10–15 min, again with the room lights on. The third training session began by head restraining the mice on the ball in complete darkness for ~15–20 min. Typically it would take 5–10 min for the mouse to learn to balance and then begin to walk or run. Mice were then head-fixed and placed on the ball during imaging under the microscope. Awake imaging lasted less than 30 min. Following awake imaging, mice were anesthetized as described above and imaging was repeated over the same cortical area to compare capillary physiology between the awake and anesthetized states.

4.5.4 Quantification of capillary network topology and capillary segment stalling

The 2PEF images of vascular networks were manually traced in three-dimensions to create a vectorized skeleton that represents the cortical vasculature using custom-written

tracing software. The researchers producing these tracings were blinded to the genotype of the animal and any treatment it had received. Volumes of these image stacks where vessels could not be readily identified and traced were excluded from all analysis. These regions were typically deep and near the edges of the imaged volume, or occasionally directly underneath a large surface vessel. Vessel segments were classified as surface and penetrating arterioles, capillaries, or ascending and surface venules. All vessels smaller than 10 μm in diameter were classed as capillaries. Large surface arterioles were distinguished from large surface venules based on morphology (arterioles were smaller diameter, had smoother walls and less tortuosity, and tended to branch more symmetrically and in Y-shape junctions as compared to venules). Other arterioles or venules were classed by tracing their connectivity to these readily identifiable large vessels.

Each capillary segment in these images was then manually classed as either flowing or stalled based on the motion of RBCs during the entire time each capillary was visible in the 3D image stack. The Texas Red dextran labels the blood plasma, but not the blood cells, so RBCs and other blood cells show up as dark patches in the vessel lumen. The motion of these dark patches indicates flowing blood cells. Each capillary segment was visible in a minimum of ~5 successive frames in the 3D image stack, or for ~5 s (capillaries not oriented parallel to the cortical surface were observed for significantly more frames). We scored a capillary segment as stalled if we did not see motion of the RBCs and other cells in the capillary segment over this observation time. This manual scoring of capillaries as flowing or stalled was performed with the researcher blinded to

the genotype and treatment status of the animal. In addition, this scoring was performed using only the image data visible on the Texas Red imaging channel. All animals had at least 800 capillary segments scored as flowing or stalled.

Using the traced vascular network, the topologically shortest path from each flowing or stalled capillary to the nearest penetrating arteriole and ascending venule was calculated using Dijkstra's algorithm *(38)*.

4.5.5 Distinguishing causes of capillary stalls

In some animals, once capillary stalls were identified we used the additional fluorescent labels to determine what was blocking blood flow in the capillary segment. Stalled capillary segments with a cell-shaped object labeled with both Rhodamine 6G and Hoechst present were scored as being caused by a leukocyte. Stalled segments with punctate objects labeled with Rhodamine 6G alone were scored as being caused by platelet aggregates. Stalled capillary segments with only RBCs present were classed as RBC stalls (note that some stalls with leukocytes or platelets present also had RBCs present — these were scored as being caused by the leukoctye or platelet aggregate). A small fraction of capillaries had no moving blood cells in them at all. Because we define flowing vessels by the motion of blood cells, these vessels with no cells present at all were also scored as stalled and classed as "empty," although it is likely there was plasma flow in these vessel segments.

We assessed if the diameter of flowing and stalled capillaries was different, on average.

To reduce the salt and pepper noise in the vascular images, we filtered using a 3D 5 x 5 x 5 pixel Gaussian filter. We then corrected for unevenness in the image intensity by filtering the image (85 x 85 pixel sized mean filter) and subtracting this from the Gaussian filtered image. The resulting image was binarized using Otsu's method *(39)*. Finally, objects smaller than 1000 voxels were eliminated, where voxels were considered part of the same connected object whenever they shared at least a corner. We then used this binarized image to correct the manual tracing of the vasculature by shifting the centerline so it was equidistant from the vessel boundaries (done within a 10-μm neighborhood to avoid confusion between neighboring capillaries). Every 5 μm along the centerline of each capillary segment, we estimated the vessel radius by finding the closest distance from the centerline to the vessel boundary. Measurements of less than 2 μm or more than 10 μm were excluded as they likely reflected imaging artifacts, and we averaged across all measurements for each capillary segment.

4.5.6 Amyloid plaque segmentation and density analysis

2PEF images of methoxy-X04 labeled amyloid plaques were filtered and binarized. Briefly, we first reduced the background signal in a line-by-line fashion by subtracting the median of each line. Salt and pepper image noise was reduced using the adaptive Wiener method with a 3 x 3 pixel kernel *(40)*. The image was then binarized using a manually-determined threshold (99% of the intensity distribution), and smoothed with a 3 x 3 pixel median filter. Objects smaller than 25 voxels were then removed, with object connectivity here defined as voxels sharing a face. The volume fraction of amyloid either globally or in a tube that follows the centerline of each capillary segment was then calculated from this binarized image. The tube

volume was generated by swaying a sphere with a specified radius along the centerline of the capillary segment from one end to the other.

4.5.7 Kinetics of capillary stalling

To determine the short-term fate of capillaries that stalled, we repeatedly imaged the same capillary bed at baseline and at 5, 10, and 15 min later in APP/PS1 mice (n= 6 animals), and tracked the fate of all the capillaries that were stalled at baseline. If a vessel was observed as stalled at all subsequent imaging time points, it was scored as remaining stalled, and if flow had resumed the stall was scored to have resolved. If the originally stalled capillary resumed flow, then re-stalled at a later time point that was scored as re-stalled. In some animals, we further determined the cause of capillary stalls at each of these time points.

To evaluate the longer-term fate of capillaries that were stalled, we imaged APP/PS1 mice (n= 5 animals) at baseline and then 1, 3, 7, and 14 days later and determined what fraction of the capillaries stalled at baseline were stalled at any subsequent imaging session.

We estimated how frequently we would observe capillaries stalled at baseline to be stalled at any subsequent imaging session assuming that no stalls lasted long enough to stay stalled between imaging sessions and that each capillary segment was equally likely to stall. With this model, the cumulative probability, P_c, of the capillaries stalled at baseline to be stalled at any subsequent imaging session is:

$$P_c = 1 - (1 - r)^N \qquad \text{Eq. 1,}$$

where r is the fraction of capillaries with stalled blood flow and N is the number of observations after the baseline imaging.

4.5.8 Administration of antibodies against Ly6G and impact on neutrophil population

We treated APP/PS1 mice (n = 9, 12-25 weeks old) with intraperitoneal injections of monoclonal antibodies against lymphocyte antigen 6 complex, locus G (Ly6G) (α-Ly6G, clone 1A8, 4 mg/kg, BD Biosciences) or an isotype control antibody (n = 6, Rat IgG2a, κ, 4 mg/kg, BD Biosciences). The same cortical capillary bed was imaged in anesthetized mice immediately before and at 30-60 min and 60-90 min after treatment. Quantification of stalled capillaries was performed blinded to imaging time and treatment type.

To determine the impact of α-Ly6G on neutrophil number, we used flow cytometry to determine neutrophil counts 24 hr after a single treatment (4 mg/kg) and after one month of treatment every three days (2 mg/kg).

Mouse blood was collected from the submandibular vein and mixed with 1x RBC lysis buffer (00-4300-54, ThermoFisher Scientific). After incubation at room temperature for 10 min, the sample was centrifuged at 500 g for 5 min and the supernatant was removed. The cell pellet was re-suspended in 500 uL of Hank's balanced salt solution (HBSS) supplemented with 1% bovine serum albumin (BSA) and centrifuged again; this washing procedure was repeated 3 times. Following isolation, neutrophils were re-suspended at a

density of 10^7 cells per ml in HBSS supplemented with 1% BSA. The cell samples were labeled at room temperature for 45 min with the following anti-mouse antibodies: anti-CD45 (560695, BD Bioscience), anti-CD11b (557686, BD Bioscience) and anti-Ly6G (551460, BD Bioscience). After washing the samples with HBSS, the remaining leukocytes were analyzed by flow cytometry using a Guava easyCyte Flow Cytometer (EMD Millipore Corporation). Data were analyzed using FlowJo software (FlowJo LLC). The neutrophil population was identified based on the side and forward scatter and later gated for $CD45^{high}$ and $CD115^{low}$ and finally gated as $CD11b^{high}$ and $Ly6G^{high}$ using FlowJo.

4.5.9 Measurement of volumetric blood flow in penetrating arterioles

To quantify blood flow in cortical penetrating arterioles, we measured the vessel diameter from image stacks and the centerline RBC flow speed from line-scan measurements, as described in Santisakultarm *T.P.* et al. *(41)*. The volumetric blood flow, *F*, was calculated as:

$$F = \frac{\pi v r^2}{2} \qquad \text{Eq. 2,}$$

where *v* is the time-averaged centerline RBC speed and *r* is the vessel radius. To correlate the impact of the number of capillaries stalled on penetrating arteriole blood flow, we imaged the same capillaries and measured blood flow in the same six to eight penetrating arterioles in both young APP/PS1 and wt mice (ages 3-4 months) and older APP/PS1 mice (age 11-14 months) treated with antibodies against Ly6G or with isotype control antibodies. Images to determine capillary stalling and line scans to determine penetrating

arteriole blood flow speed were taken at baseline and at 30-60 and 60-90 min after treatment. All analysis was conducted blinded to the animal genotype, age, treatment, and imaging time point.

4.5.10 Measurement of global blood flow using ASL-MRI

Imaging was performed on a 7.0 Tesla small animal MRI system with 450 mT/m gradient amplitude and a 4500 T/m/s slew rate (Biospec 70/30, Bruker). The animals were anesthetized with isoflurane in oxygen and immobilized in the MRI using a nose cone and bite ring. A volume coil was used for transmission and a surface coil for reception. We imaged APP/PS1 and wt mice (age 7-9 months) at baseline. About 48 hrs later, animals were given an intraperiotenial injection of α-Ly6G or isotype control antibodies (4 mg/kg) and a second set of images were acquired between 2-6 hr after injection.

Anatomical images were acquired to find a coronal slice at a location approximately 1 mm caudal to Bregma *(42)*. This position was used for subsequent ASL imaging, which was based on a FAIR-RARE pulse sequence that labeled the inflowing blood by global inversion of the equilibrium magnetization *(43)*. In this method, inversion recovery data from the imaging slice are acquired after selective inversion of the slice and after inversion of both the slice and the surrounding tissue. The difference of the apparent R1 relaxation rate images then yields a measure of the CBF *(44)*. Three averages of one axial slice were acquired with a field of view of 15 × 15 mm, spatial resolution of 0.23 × 0.23 × 2 mm^3, echo time TE of 5.36 ms, effective TE of 26.84 ms, repeat time TR of 10 s, and a RARE factor of 36. This resulted in a total scan time for the CBF images of about 25

min. Turbo-RARE anatomical images were acquired with the following parameters: 10 averages of 14 slices with the same field-of-view and orientation as the ASL images, resolution = 0.078 × 0.078 × 1 mm^3, TE = 48 ms, TR = 2000 ms, and a RARE factor of 10. The total scan time was 6:20 min.

For computation of CBF, the Bruker ASL perfusion processing macro was used. It uses the model and includes steps to mask out the background and ventricles *(44)*. The masked CBF images were exported to Analyze format on the MRI console. We then used the anatomical image to create a mask that outlined the entire cortical region, excluding the sinus, and averaged the CBF measurement across this region for each animal at each imaging time point. Analysis of ASL-MRI data was conducted blinded to animal genotype and treatment.

4.5.11 Extraction of network topology and vessel diameters from mouse anatomical dataset

One large postmortem dataset from the vibrissa primary sensory (vS1) cortex in mouse previously obtained by Tsai et al. *(12)* and Blinder et al. *(33)*, was used for this study (~1 mm^3 and ~15,000 vessel segments). In brief, this dataset was obtained by filling the vessels with a fluorescent indicator, extracting the brain and imaging with 2PEF from the pial surface to near the bottom of cortex. In this dataset, penetrating arterioles and ascending venules that reached the pial surface were identified by following their connections to a large cerebral arteriole or venule. We further labeled subsurface vessels in three classes: arterioles, capillaries, and venules. Starting with the surface and

penetrating arterioles (venules) were defined by iteratively seeking all vessels with diameter above 6 μm connected to any previously labeled arteriole (venule). All remaining vessels were labeled as capillaries. The diameter threshold was manually chosen as the smallest integer diameter value which resulted in arteriolar and venular trees that exhibited no loops, in contrast to the very looped capillary network.

Due to post-mortem shrinkage, vessel diameters in this mouse dataset were smaller than those measured *in-vivo*, so required rescaling *(12, 41, 46)*. As blood flow is highly dependent on vessel diameters, two successive corrections were applied. First, a monotonically increasing function, which tends to one at large diameters, was applied to all vessels diameters:

$$d = d_0 + A\cos\left(\tan^{-1}\left(\frac{d_0}{B}\right)\right), \quad A > 0, \quad B > \frac{2}{3}A\sin\left(\tan^{-1}\left(\frac{1}{\sqrt{2}}\right)\right) \quad \text{Eq. 3}$$

where d is the corrected diameter and d_0 is the diameter extracted from the image stack. A and B are constrained parameters calculated so that the corrected vessel diameter distribution matched *in vivo* measurements from two photon microscopy *(12)*, as shown in Fig. 4.S18. This function ensures that the hierarchy of diameters in the network is preserved and the larger vessels are not rescaled. For the network represented in Fig. 4.1H, A=1.4 and B=10.3, so that the diameter threshold for capillary vessels becomes 7.2 μm. A second depth-dependent correction was then applied to the diameter of arterioles and venules:

$$d = d_0(az + b) \quad \text{Eq. 4}$$

where z is the depth below the cortical surface and a and b are parameters determined so

that the diameters of the trunks of the penetrating arterioles and ascending venules matched *in-vivo* measurements *(46)*. For the network represented in Fig. 4.1H, these parameters were a=-0.0014 μm^{-1} (-9.36e-4 μm^{-1}) and b=2.54 (2.02) for arterioles (venules).

4.5.12 Extraction of network topology and vessel diameters from human anatomical dataset

The dataset used was previously obtained by Cassot et al. *(47)* and Lauwers et al. *(13)* from thick sections (300 μm) of a human brain injected with India ink from the Duvernoy collection *(48)*. The brain came from a 60-year old female who died from an abdominal lymphoma with no known vascular or cerebral disease. It corresponds to a large volume (6.4 mm^3 of cerebral cortex) extending across 20.8 mm^2 along the lateral part of the collateral sulcus (fisiform gyrus) extracted from Section S2 in Lauwers et al. *(13),* and includes a total of 27,340 vessel segments. The mean radius and length of each segment were rescaled by a factor of 1.1 to account for the shrinkage of the anatomical preparation. The main vascular trunks were identified manually and divided into arterioles and venules according to their morphological features, following Duvernoy's classification *(48, 49)*. Following Lauwers et al. *(13)* and Lorthois et al. *(14)* as in the mouse data sets, arterioles (venules) were defined by iteratively seeking all vessels with diameter above 9.9 μm connected to any previously identified arteriole (venule), so that no loops were present. All remaining vessels were classified as capillaries.

4.5.13 Synthetic network generation

The synthetic periodic network of order three (i.e. three edges per node) was generated to match the mouse network parameters. A 1-mm^3 vascular network was constructed by replication of a simple periodic network (fig. 4.S4). Capillary diameters and lengths were uniform and were set to the averages for the mouse network. A single penetrating arteriole and ascending venule (with diameters set to the averages from the mouse network) served as inlet/outlet. The distance between the inlet and outlet corresponded to the average distance between penetrating arterioles and ascending venules from the mouse dataset.

4.5.14 Blood flow simulations

The methodology for simulating blood flow in these intra-cortical vascular networks has been presented in detail in Lorthois et al. *(14)*. Briefly, the network was represented by a graph in which edges represent vessel segments between branches that are characterized by an average diameter and length. We used a one-dimensional (analogous to electric circuit models) nonlinear network model that was slightly modified from Pries et al. *(50)* to handle large networks for the flow simulations. Using an iterative procedure, the model takes into account the complex rheological properties of blood flow in the microcirculation (Fåhræus, Fåhræus-Lindqvist, and phase separation effects). These effects are modeled using empirical descriptions *(51, 52)* deduced from experiments in rats. The model was used to calculate the flow and hematocrit in each vessel and the pressure at each intersection of vessels. For the human dataset, the parameters for the empirical descriptions of the Fåhræus, Fåhræus -Lindqvist and phase separation effects

were re-scaled in order to account for the difference in characteristic size between human and rat RBCs, as proposed by Lorthois et al. *(14)* and Roman et al. *(27)*. This simulation approach has no free parameters.

Boundary conditions: Physiologically realistic pressure drops of 60 mmHg, as measured in rats *(54)* and estimated in humans *(14)*, were imposed between all arteriolar and venular trunks feeding and draining the computational volume, while a no-flow condition was imposed on deeper arteriolar or venular vessels that intersected the lateral boundaries of the simulated volume. A constant discharge hematocrit of 0.45, corresponding to a typical value of the systemic hematocrit, was also imposed in arteriolar trunks. Moreover, a pseudo-periodic boundary condition was applied to all capillaries at the lateral boundaries, as illustrated in fig. 4.S19. Fictitious vessels were created that link capillaries intersecting opposing faces in a semi random fashion. A grid was created on the two faces and refined until, for a given cell, each capillary on one face was matched with at most 2 capillaries on the opposing face, allowing the creation of fictitious bifurcations. Once the optimal grid was found, the closest neighboring vessels from the opposing faces were connected together. The length of the resulting fictitious vessels was set to 50 μm and their diameters to the average diameters of the connected capillaries. This pseudo-periodic boundary condition is similar in spirit but simpler and more computationally effective than the one recently introduced by Schmid et al. *(55)*. Finally, a no-flow boundary condition was applied to all vessels intersecting the bottom face of the domain. We also compared the results with no-flow boundary conditions for all capillaries at the lateral boundaries.

Simulating stalls: In order to study the influence of capillary stalling on cerebral blood flow, a given proportion of capillaries in each network was randomly occluded. To simulate occlusion, the radius of the selected vessels was divided by 100. This resulted in a large increase of the hemodynamic resistance, of order 10^8, and a similar decrease of the computed flow through these vessels. At least five repetitions were performed for each proportion of stalled capillaries and each set of conditions considered. On the mouse data, 1000 simulations in total were run on a 32-core Intel(R) Xeon E5-2680 v2 @ 3.3 GHz for a total computational time of ~170 hours. For human data set, about 100 simulations were run on the same machine for a total computational time of ~50 hours.

4.5.15 Behavior experiments

All experiments were performed under red light in an isolated room. The position of the mouse's nose was automatically traced by Viewer III software (Biobserve, Bonn, Germany). In addition to the automatic results obtained by Viewer III software, a blinded experimenter independently scored mouse behavior manually. Animals were taken into the behavior room one-hour prior to the experiment. Behavioral analysis was conducted at baseline and at 3 and 24 h after injection with α-Ly6G or isotype control antibodies (IP 4 mg/kg). Animals were then treated every three days for four weeks (IP 2 mg/kg) and behavior experiments were repeated. The OR, Y-maze, balance beam walk, and forced swim tests were performed at all time points. The NOR task was performed only at baseline and the 4-week time point to avoid animals becoming accustomed to the objects. Animals were ~11 months of age at the start of the experiment (APP/PS1, α-Ly6G n=11;

APP/PS1 Iso-Ctl, n=9; wt α-Ly6G, n=10; and wt Iso-Ctl, n=10).

Object replacement test: The object replacement (OR) task evaluated spatial memory performance. All objects were validated in a separate cohort of mice to ensure that no intrinsic preference or aversion was observed and animals explored all objects similarly. Exploration time for the objects was defined as any time when there was physical contact with an object (whisking, sniffing, rearing on or touching the object) or when the animal was oriented toward the object and the head was within 2 cm of the object. In trial 1, mice were allowed to explore two identical objects for 10 min in the arena and then returned to their home cage for 60 min. Mice were then returned to the testing arena for 3 min with one object moved to a novel location (trial 2). Care was taken to ensure that the change of placement alters both the intrinsic relationship between objects (e.g. a rotation of the moved object) and the position relative to internal visual cues (e.g. new location in the arena; one wall of testing arena had a pattern). In addition to using the tracking software to determine the object exploration times, the time spent at each object was manually scored by an independent experimenter who was blinded to the genotype and treatment. The preference score (%) for OR tasks was calculated as ([exploration time of the novel object]/[exploration time of both objects]) × 100 from the data in trial 2. Automated tracking and manual scoring yielded similar results across groups, so we report the automated tracking results.

Y-Maze: The Y-Maze task was used to measure working memory by quantifying spontaneous alternation between arms of the maze. The Y-maze consisted of three arms

at 120° and was made of light grey plastic. Each arm was 6-cm wide and 36-cm long, and had 12.5-cm high walls. The maze was cleaned with 70% ethanol after each mouse. A mouse was placed in the Y-maze and allowed to explore for 6 min. Mouse behavior was monitored, recorded, and analyzed using the Viewer software. A mouse was considered to have entered an arm if the whole body (except for the tail) entered the arm and to have exited if the whole body (except for the tail) exited the arm. If an animal consecutively entered three different arms, it was counted as an alternating trial. Because the maximum number of triads is the total number of arm entries minus 2, the spontaneous alternation score was calculated as (the number of alternating triads)/(the total number of arm entries − 2).

Forced swim test: The forced swim test measured depression-like behavior. Mice were individually placed in a 4-L glass beaker filled with 2.5 L of 25°C water. Mice were allowed to adjust for 1 min and then were evaluated for 6 min. An experimenter blind to the genotype and treatment analyzed the videotaped behavior and scored the immobility time, defined by the absence of active, escape-oriented behaviors such as swimming, jumping, rearing, sniffing or diving.

Balance beam walk: The balance beam walk measured motor coordination and balance by scoring the ability of the mice to traverse a graded series of narrow beams to reach an enclosed safety platform. The beams consisted of long strips of wood (80 cm) with round cross section of 12- and 6-mm diameter. The beams were placed horizontally, 40 cm above the floor, with one end mounted on a narrow support and the other end attached to

an enclosed platform. Bright light illuminated the end of the beam where the mice started. Mice received three consecutive trials on each of the round beams, in each case progressing from the widest to the narrowest beam (15 min between each trial). Mice were allowed up to 60 s to traverse each beam. The time to traverse each beam and the number of times either hind paw slipped off each beam were recorded for each trial. Analysis of each measure was based on the mean score across all trials for that mouse at that time point. Experimenters were blinded to the genotype and the treatment of the mice.

Novel object recognition test: The novel object recognition (NOR) task measures recognition memory and is based on rodents' innate preference for exploring novel objects. This test was conducted only in the animals at baseline and after 4 weeks of treatment. The testing approach was identical to the OR task, but with a novel object placed at the location of one of the initial objects in trial 2.

4.5.16 ELISA

After the conclusion of the behavior experiments, the APP/PS1 animals that had received α-Ly6G or isotype control antibodies every 3 days for a month were sacrificed by lethal injection of pentobarbital (5 mg/100 g). Brains were quickly extracted and divided along the centerline. One half was immersed in 4% paraformaldehyde in phosphate buffered saline (PBS) for later histological analysis and the other half was snap frozen in liquid nitrogen.

The frozen APP/PS1 mouse hemi-brains (Iso-Ctr: n=6, 11.5-12.5 months old; α-Ly6G: n=7, 11.5-12.5 months old) were weighed and homogenized in 1 ml PBS containing complete protease inhibitor (Roche Applied Science) and 1 mM AEBSF (Sigma) using a Dounce homogenizer. The homogenates were then sonicated and centrifuged at 14,000 g for 30 min at 4° C. The supernatant (PBS-soluble fraction) was removed and stored at −80° C. The pellet was re-dissolved in 0.5 ml 70% formic acid, sonicated, and centrifuged at 14,000 g for 30 min at 4° C, and the supernatant was removed and neutralized using 1M Tris buffer at pH 11. Protein concentration was measured in the PBS soluble fraction and the formic acid soluble fraction using the Pierce BCA Protein Assay (Thermo Fischer Scientific). The PBS soluble fraction extracts were diluted 1:5. Formic acid extracts were diluted 1:1 after neutralization. These brain extracts were analyzed by sandwich ELISA for Aβ1-40, Aβ1-42, and Aβ aggregates using commercial ELISA kits and following the manufacturer's protocol (Aβ1-40: KHB3481; Aβ1-42: KHB3441; Aβ aggregates: KHB3491, Thermo Fisher Scientific). The Aβ concentration was calculated by comparing the sample absorbance with the absorbance of known concentrations of synthetic Aβ1–40 and Aβ1–42 standards on the same plate. Data was acquired with a Synergy HT plate reader (Biotek) and analyzed using Gen5 software (BioTek) and Prism (Graphpad).

4.5.17 Histopathology

Immunohistochemistry was performed on the brains of mice chronically treated every third day for 4 weeks with either α-Ly6G antibody or isotype control (Iso-Ctr n=5, α-Ly6G n=4). A single paraformaldehyde-fixed hemisphere of each brain was cut into 40

μm thick sagittal sections.

Every sixth section from each mouse was stained with 1% Thioflavin-S (T1892**,** Sigma) for 10 min at room temperature and washed twice with 80% ethanol for 2 min. The sections were mounted using Fluoroshield with DAPI (F6057, Sigma). Images were taken using confocal microscopy (Zeiss Examiner.D1 AXIO). For each image, the background was subtracted using the ImageJ background subtraction plugin (Rolling ball with 7 μm radius). Images were then manually thresholded, using the same threshold for all sections from a given mouse. Appropriate thresholds varied mouse to mouse and were set to ensure that the smallest Thioflavin-S labeled objects that morphologically appeared to be an amyloid plaque remained above threshold. Cortical and hippocampal regions of interest were defined in each section anatomically, and the fraction of pixels above threshold was determined across all sections for these regions of interest. All image processing was done blinded to treatment group. As a second measure of amyloid deposition, we manually counting the number of Thioflavin-S positive amyloid plaques in the cortex and hippocampus, again across all sections and while blinded to the treatment group. All sections were stained and imaged in parallel. Artifacts such as bubbles were eliminated from analysis by manually excluding these regions.

4.5.18 Statistical analysis

Boxplots were created using Prism7 (GraphPad). The box extends between the values for the 25th and 75th percentile of the data. The whiskers extend 1.5 times the difference between the value of the 75th and 25th percentile of the data from the top and bottom of

the box. Values lying outside the whiskers were defined as outliers and the mean was computed excluding these outliers. The median is indicated with a black horizontal line inside the box, while the mean is indicated with a red horizontal line. Violin plots were created using the statistical software package, R *(56)*.

Data in all groups was tested for normality using D'Agostino-Pearson omnibus normality test. Parametric statistics were used only if the data in all groups in the comparison were normally distributed. The statistical significance of differences between multiple groups was determined using one-way analysis of variance (ANOVA) followed by Tukey's multiple comparison correction for normally distributed data, and using Kruskal-Wallis one-way ANOVA followed by Dunn's multiple comparison correction for data with a non-normal distribution. Statistical comparisons between two groups were performed using the Student's t test or paired t test for normally distributed data, or using the Mann-Whitney test or Wilcoxon matched-pairs test for data with a non-normal distribution. P-values smaller than 0.05 were considered statistically significant. All statistical analysis was performed using Prism7 (GraphPad).

We use a standardized set of significance indicators across all figures in this manuscript. For comparisons between groups: *$p<0.05$, **$p<0.01$, ***$p<0.001$, ****$p<0.0001$. For matched comparisons before and after treatment: +$p<0.05$, ++$p<0.01$. Supplementary Table 1 provides details of the groups compared, animal and capillary numbers, statistical tests, and explanatory notes for individual panels in the main figures. This information is included in the caption of supplementary figures.

4.6 SUPPLEMENTARY TEXT ON NUMERICAL SIMULATIONS OF CEREBRAL BLOOD FLOW CHANGES INDUCE BY CAPILLARY OCCLUSIONS

In previous work, we studied how the occlusion of a single cortical capillary influenced blood flow in downstream vessels *(11)* and found strong reductions in blood flow (10% of baseline value 1 branch downstream; 25% at 2 branches; 50% at 3 and 4 branches), suggesting that even the small fraction of occluded capillaries we observed in APP/PS1 mice could cause a significant decrease in overall brain blood flow. To test this idea, we simulated blood flow in anatomically accurate blood vessel networks from mice and humans and examined how flow changed when we occluded a random selection of capillaries.

4.6.1 Validation of simulations by comparison to *in vivo* measurements in mouse

As described in the Materials and Methods above, our simulations resulted in calculated values for flow (Fig. 4.S20A), pressure (fig. 4.S20B), and hematocrit (fig. 4.S20C) in each vessel segment in the volume. We validated the simulation by comparing *in vivo* measurements of blood flow at different levels in the microvascular hierarchy acquired by 2PEF from the top 300 μm of mouse cortex (data from Santisakultarm, *et al. (41)*) with the simulation predictions. The simulation results are highly dependent on the boundary conditions imposed on capillaries at the lateral edges of the simulation volume. The calculated velocity distribution using pseudo-periodic boundary conditions in capillaries up to 300 μm in depth and using the vessel diameter corrections described above matches the experimental distribution well (fig. 4.S20D). For comparison, the

velocity distribution calculated using diameters from the raw datasets (without correction for the difference in vessel size between *in vivo* and post mortem measurements) and that calculated using a no-flow boundary condition both led to an order of magnitude underestimation of capillary flow speeds (fig. 4.S20D). Our new pseudo-periodic boundary condition, together with the correction of vessel diameters, led to a velocity distribution that approaches the distribution of experimental velocities. The experimental distribution has a sharper peak, which might be due to experimental bias associated with the limited number of vessels in which these measurements have been performed (147 *in vivo* measurements vs. 3,400 capillaries in the simulations). The simulated speeds in penetrating arterioles and ascending venules as a function of their diameters also closely matched experimental results from Santisakultarm, et al. *(41)* and from Taylor, et al. *(46)* (fig. 4.S20E).

4.6.2 Numerical simulation of cerebral blood flow reductions caused by capillary occlusions:

The effect of occlusions in capillaries was investigated by randomly selecting a given proportion of capillaries and reducing their flow by imposing a 100-fold reduction in diameter (fig. 4.S21A, Fig. 4.1H). To quantify the effects of the occlusions, we calculated the normalized cortical perfusion as the summed flow in the penetrating arterioles feeding the region, normalized by the value calculated with no capillary occlusions (Fig. 4.1J). While the magnitude of this summed flow is highly dependent on the boundary conditions, the decrease in flow due to capillary occlusions was much less sensitive to the choice of boundary conditions (fig. 4.S21B). For the mouse network shown in Figs. 4.1H

and S20A with pseudo-periodic boundary conditions and diameter correction, we found a linear decrease in the normalized perfusion with a slope S=-2.3±0.2 %baseline perfusion/% capillaries stalled (mean±SD) (Fig. 4.1J). This linear behavior was very robust to variations in the parameters chosen for the computations, with slopes equal to -2.2±0.1 (-2.1±0.2) with no-flow boundary conditions and diameter correction (no diameter correction). In order to evaluate the influence of boundary conditions with regard to the size of the simulated volume, 300 μm-thick sub-volumes of the mouse anatomical datasets were randomly extracted. The decrease in blood flow with increasing numbers of stalled capillaries was slightly larger when 300 μm-thick sub-volumes of the datasets were used (-2.6±0.4 and -2.9±0.5 with the pseudo-periodic boundary condition and the no-flow boundary condition, respectively), as compared to the full ~1 mm-thick volume. In Fig. 4.1J, only computations on the maximum simulation volume with the corrected diameters and pseudo-periodic boundary conditions are presented.

The simulations in the human network using pseudo-periodic boundary conditions yielded a slope of S=-2.3±0.6, very similar to the mouse results. This linear decrease was also observed in synthetic periodic networks of order three (i.e. three edges per node; S=-2.9, Fig. 4.1J).

4.6.3 Limitations and methodological considerations

The human dataset used in the simulations was only 300 μm thick, raising concerns about the influence of boundary conditions. The broad agreement between simulation results in mouse datasets with 1-mm and 300-μm thickness reduces this concern. The

simulations predicted a similar CBF increase across mouse and human vascular networks when stalls were reduced, suggesting that the blood flow improvements we observed in APP/PS1 mice may be achievable in humans.

The simulations predicted a smaller impact of capillary stalling on CBF than we observed experimentally. One possible explanation is that the simulations used vascular networks from wt mice, while AD mouse models have different vascular densities and topologies *(57)* that may influence the sensitivity of CBF to capillary stalls. In addition, increased leukocyte adhesion in APP/PS1 mice may lead not only to complete stalls, but also to slowed flow in some capillaries that is not captured in the simulations.

We also observed differences in the 2PEF and ASL-MRI measurements of blood flow increase after alpha-Ly6G administration that may be due to the limited sampling of penetrating arterioles at one anatomical location with 2PEF and to taking ASL-MRI data several hours later after treatment than 2PEF. In addition, the correlation between ASL-MRI values and arteriole flow may not be exact due to technical limitations in mouse ASL-MRI.

4.7 SUPPLEMENTARY FIGURES

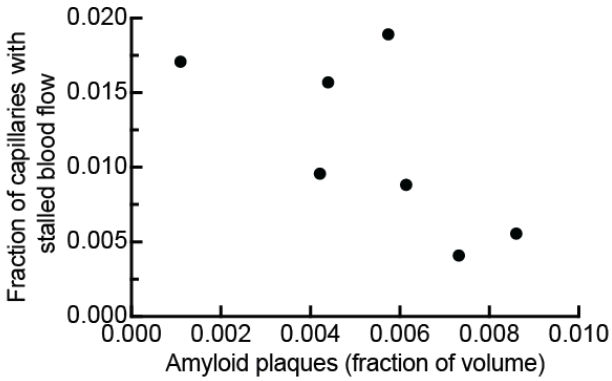

Fig. 4.S1. The fraction of capillaries with stalled blood flow did not increase with increasing cortical amyloid plaque density in APP/PS1 mice. Fraction of capillaries with stalled blood flow as a function of the cortical volume fraction that was labeled by methoxy-X04. Mice ranged from 50 to 64 weeks of age.

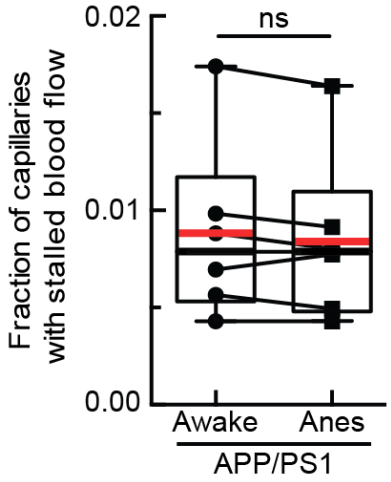

Fig. 4.S2. Plot of the fraction of capillaries with stalled blood flow in mice imaged while anesthetized and awake. Lines connecting data points indicate data from the same

animal. Animals were first trained to remain calm while head fixed and standing on a spherical treadmill. On the day of imaging, animals were briefly anesthetized to enable retro-orbital injection of Texas-Red dextran, and were then allowed to wake up. We imaged these animals first while awake and then while anesthetized under 1.5% isoflurane, with both imaging sessions occurring on the same day (n = 6 mice, no significant difference by Wilcoxon test).

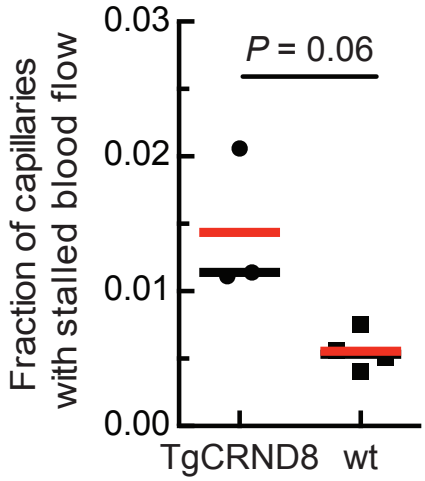

Fig. 4.S3. 2PEF imaging of cortical vasculature reveals a higher fraction of stalled capillaries in TgCRND8 mice as compared to wt mice. Fraction of capillaries with stalled blood flow in TgCRND8 and age-matched wild type littermates (TgCRND8: 3 mice, 3,028 capillaries; wild type: 4 mice, ~4,062 capillaries; p=0.06, Mann-Whitney).

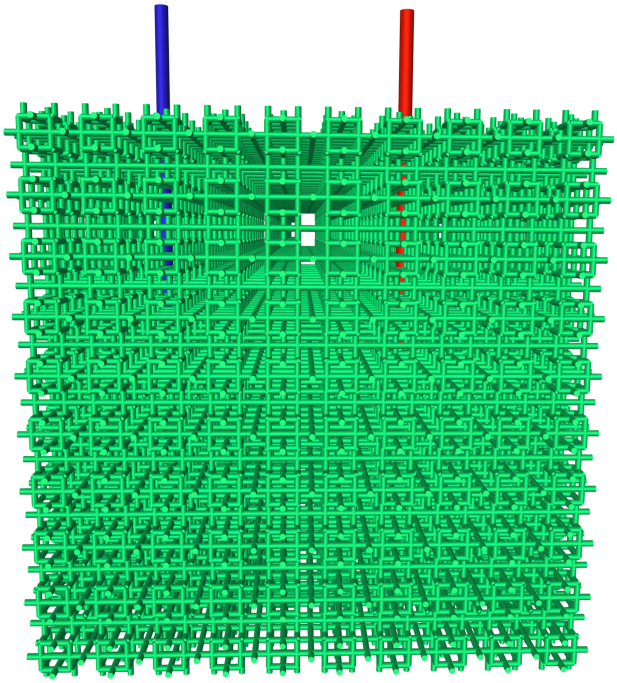

Fig. 4.S4. Synthetic capillary network of order three. Capillaries are indicated in green, while red and blue indicate the single feeding arteriole and draining venule, respectively.

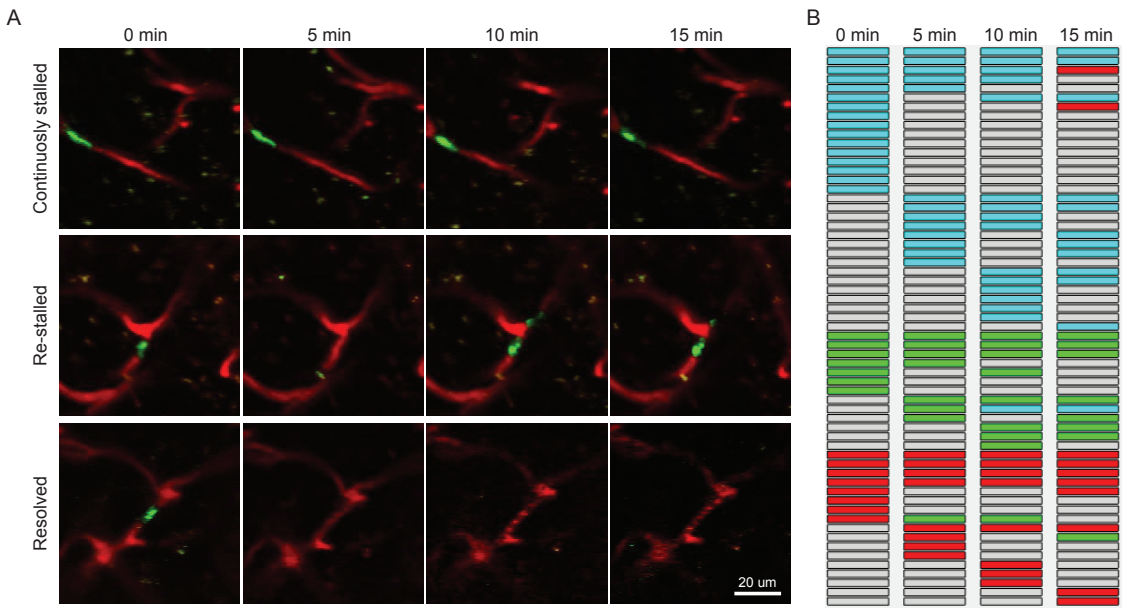

Fig. 4.S5. Characterization of capillary stall dynamics in APP/PS1 mice. (A) Repeated 2PEF imaging over 15 min of capillaries that were stalled at the baseline measurement and (top) remained stalled, (middle) began flowing and then re-stalled and (bottom) resolved and remained flowing. Blood plasma labeled with Texas-Red dextran (red) and leukocytes labeled with Rhodamine 6G (green). (B) Characterization of the fate of individual capillaries observed as being stalled across four image stacks taken at baseline and 5, 10, and 15 min later. Each row represents an individual capillary and the color of the box for each capillary at each time point indicates the status: flowing (grey), stalled with a leukocyte present (cyan), stalled with platelet aggregates present (green), and stalled with only RBCs (red).

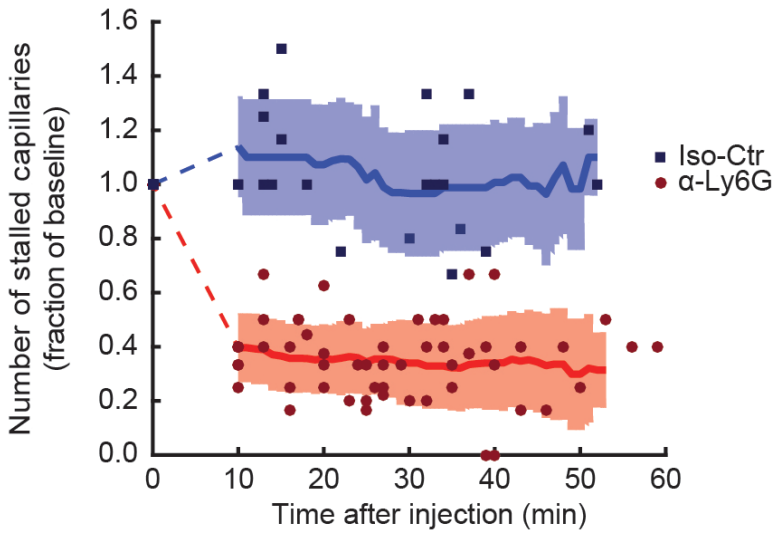

Fig. 4.S6. Number of stalled capillaries in APP/PS1 mice dropped rapidly after α-Ly6G administration. 2PEF image stacks were taken repeatedly over an hour after α-Ly6G or isotype control antibody injection and the number of stalled capillaries determined at each time point (α-Ly6G: n=6 mice; Iso-Ctr: n=4; each mouse imaged 2 to 6 times over the hour).

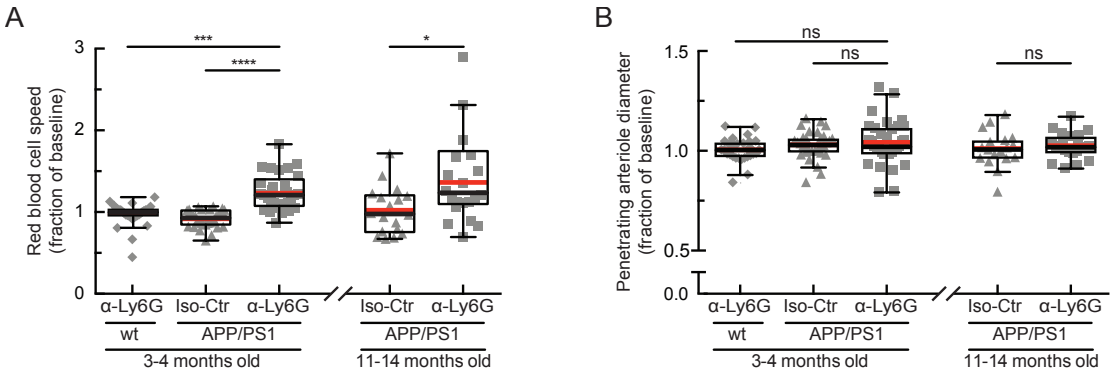

Fig. 4.S7. Administration of antibodies against Ly6G increased the RBC flow speed but did not alter the diameter of cortical penetrating arterioles in APP/PS1 mice. (A) RBC flow speed and (B) vessel diameter after α-Ly6G or isotype control antibody

administration in young (3-4 months) and old (11-14 months) APP/PS1 mice and wt control animals shown as a fraction of baseline (young wt α-Ly6G: 5 mice, 30 arterioles; young APP/PS1 Iso-Ctr: 5 mice, 32 arterioles; young APP/PS1 α-Ly6G: 5 mice, 33 arterioles; old APP/PS1 Iso-Ctr: 3 mice, 18 arterioles; old APP/PS1 α-Ly6G: 3 mice, 22 arterioles; * $p<0.05$, ** $p<0.01$, *** $p<0.001$, **** $p<0.0001$, Kruskal-Wallis one-way ANOVA with post-hoc pair-wise comparisons using Dunn's multiple comparison test).

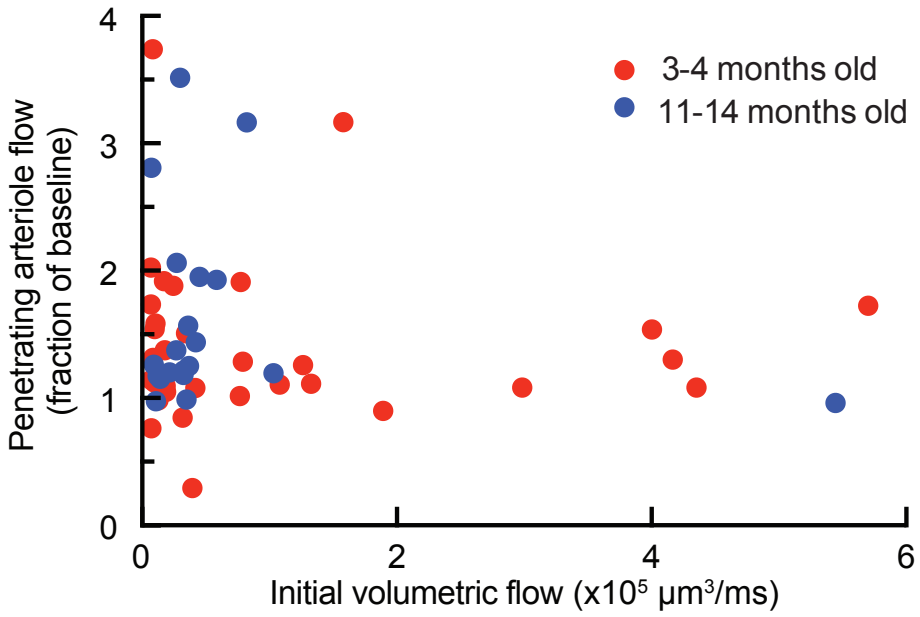

Fig. 4.S8. Penetrating arterioles with slower initial flow tended to increase flow speed more after α-Ly6G injection in APP/PS1 mice. Plot of penetrating arteriole flow after α-Ly6G antibody administration in young (3-4 months) and old (11-14 months) APP/PS1 mice shown as a fraction of baseline flow. Same data as shown in Fig. 3C.

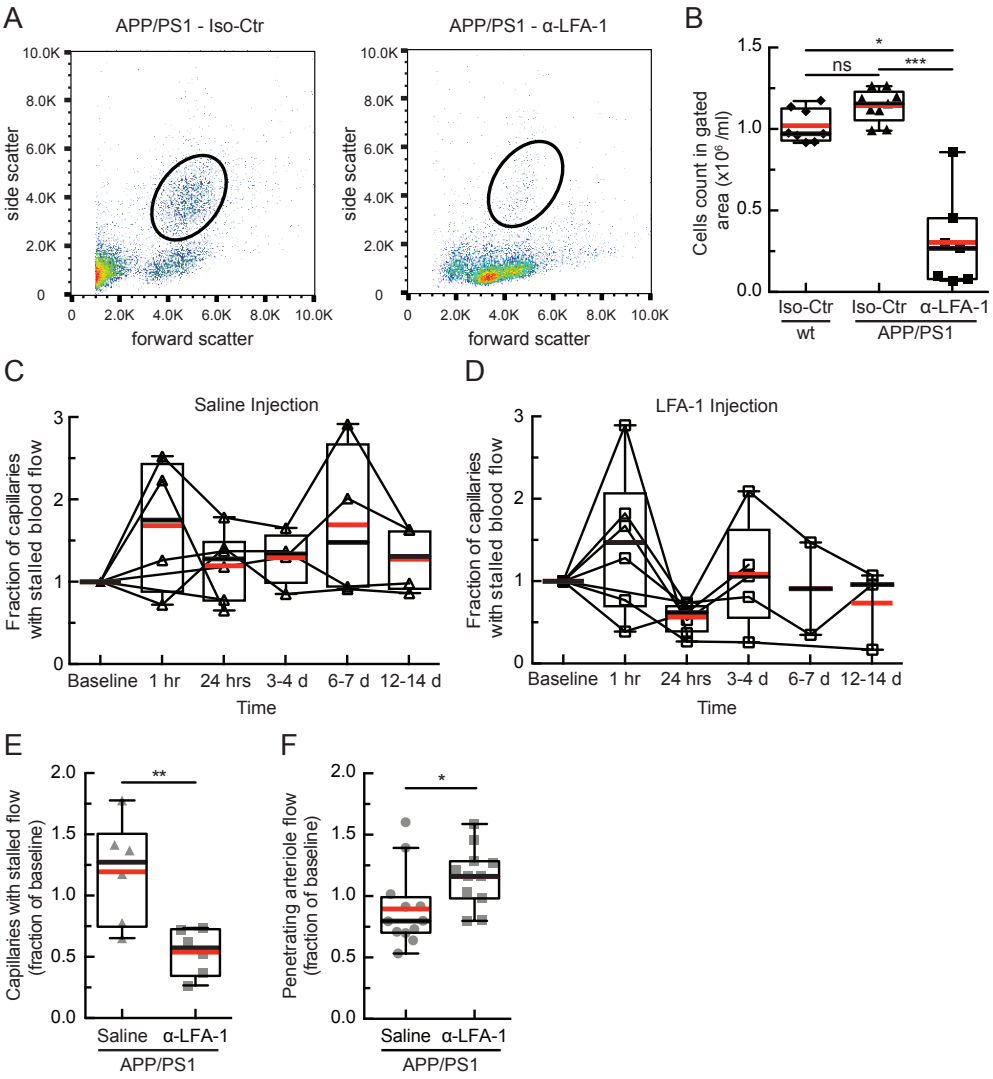

Fig. 4.S9. Treating APP/PS1 mice with α-LFA-1 reduced the number of stalled capillaries and improved arterial blood flow after 24 hours. (A) Flow cytometry scatter plots for APP/PS1 mice 24 hours after injection of isotype control antibodies (left) or with antibodies against Lymphocyte Functional Antigen 1 (α-LFA-1; M17/4 clone, BD Biosciences; 4 mg/kg, retro-orbital injection). Circles depict the gate used to identify leukocytes. (B) Leukocyte concentration in the blood 24 hours after treatment with α-LFA-1 or isotype control antibodies in APP/PS1 and wt mice. Leukocytes counts in the

gating area were decreased by 84% after α-LFA-1 as compared to the isotype control in APP/PS1 mice (Iso-Ctr in wt: 8 mice, Iso-Ctr in APP/PS1: 9 mice, α-LFA-1 in APP/PS1: 7 mice; *p<0.05, ***p<0.001, Kruskal-Wallis one-way ANOVA with post-hoc pair-wise comparisons using Dunn's multiple comparison test). (C and D) Fraction of capillaries with stalled blood flow as a function of time after a single retro-orbital treatment with 0.9% saline (C) or α-LFA-1 antibodies (D) in APP/PS1 mice (saline: n = 6 mice; α-LFA-1: n = 7 mice, 4 mg/kg). We observed a transient increase in the number of capillaries with stalled blood flow at about 1 hr after treatment in both groups. There was a significant decrease in the fraction of stalled capillaries 24 hours after injection in the α-LFA-1 group. Images were collected over the same capillary bed on each imaging day, and the fraction of capillaries stalled was determined for each time point, with the analysis performed blinded to treatment day and treatment type. (E) Number of stalled capillaries, expressed as a fraction of the baseline number, 24 hrs after administration of α-LFA-1 or saline. α-LFA-1 reduced capillary stalls by 65% as compared to the saline control. (*n* = 6 mice per treatment group. **p<0.01, Mann-Whitney test). (F) Fraction of baseline arteriole flow in penetrating arterioles from APP/PS1 mice 24 hours after α-LFA-1 or saline treatment. Each point represents a single arteriole in one mouse. The blood flow was increased after α-LFA-1 treatment by 29% compared with saline controls (APP/PS1 α-LFA1: 4 mice, 11 arterioles; APP/PS1 saline: 4 mice, 12 arterioles; *p<0.05, Mann- Whitney test).

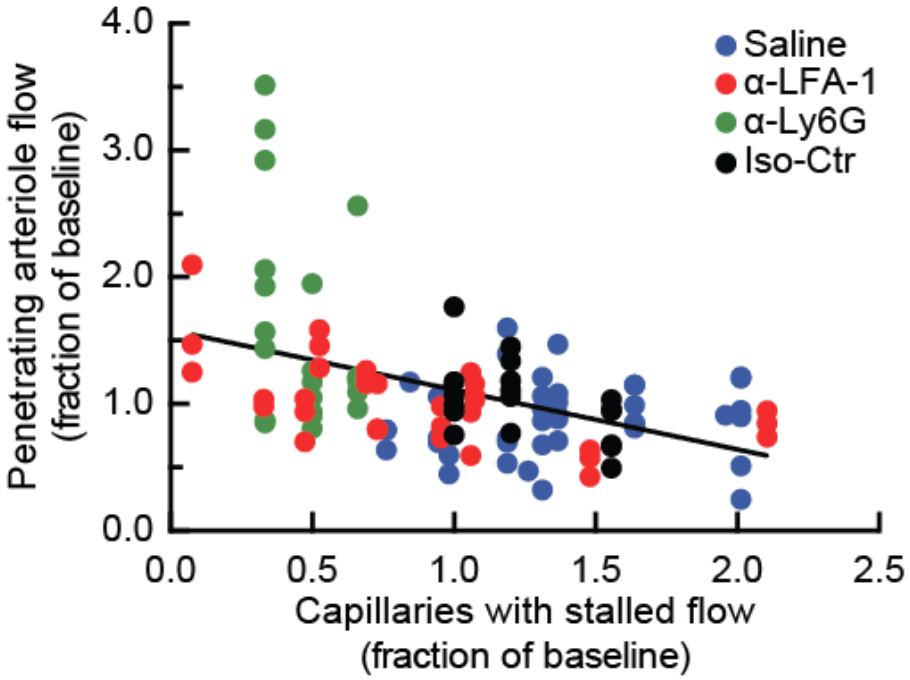

Fig. 4.S10. Brain penetrating arteriole blood flow negatively correlates with the number of capillaries stalled in underlying capillary beds in APP/PS1 mice. To correlate the effect of capillary stalling on penetrating arteriole blood flow, we imaged the same capillaries and measured blood flow in the same penetrating arterioles in APP/PS1 mice multiple times before and after administration of saline, α-LFA-1, α-Ly6G, and isotype control antibodies. For saline and α-LFA-1 animals, there were measurements at multiple time points over two weeks (data in Fig. S9). For α-Ly6G and isotype control animals there were measurements only at baseline and ~1 hr after administration (data in Fig. 3C and Figs. S7 and S8). For each penetrating arteriole at each imaged time point, we plotted the volumetric flow, expressed as a fraction of the baseline volumetric flow, as a function of the number of capillaries stalled at that time point, expressed as a fraction of the baseline number of capillaries stalled (APP/PS1 α-LFA1: 4 mice, 11 arterioles; APP/PS1 saline: 4 mice, 12 arterioles; APP/PS1 α-Ly6G: 3

mice, 22 arterioles; APP/PS1 Iso-Ctr: 3 mice, 18 arterioles). These data confirm the sensitive dependence of penetrating arteriole blood flow on the fraction of capillaries with stalled flow across several different manipulations that led to either increases or decreases in the fraction of capillaries that are stalled. The linear regression is defined by: $Y = -0.47\ X + 1.6$ ($R^2 = 0.2$, goodness of fit test; 95% confidence interval on slope: -0.65 – -0.29).

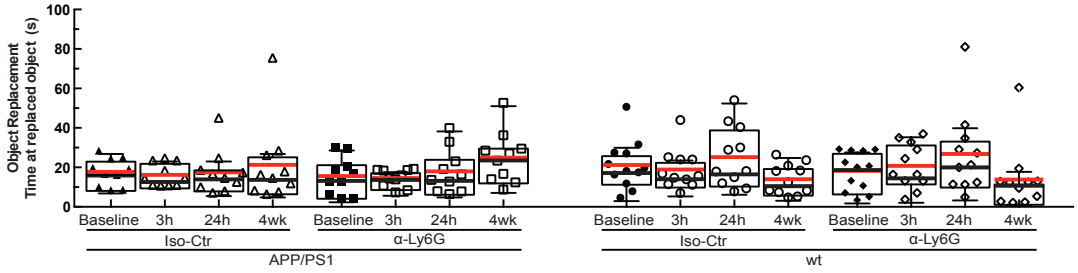

Fig. 4.S11. Time spent at the replaced object in wild type controls and APP/PS1 animals treated with α-Ly6G or isotype control antibodies. Time spent at the replaced object measured over 6 minutes for APP/PS1 and wt mice at baseline and at 3h and 24h after a single administration of α-Ly6G or isotype control antibodies, and after 4 weeks of treatment every three days (APP/PS1 Iso-Ctr: 10 mice; APP/PS1 α-Ly6G: 10 mice; wt Iso-Ctr: 11 mice; wt α-Ly6G: 11 mice; no significant differences among groups as determined by Kruskal-Wallis one-way ANOVA).

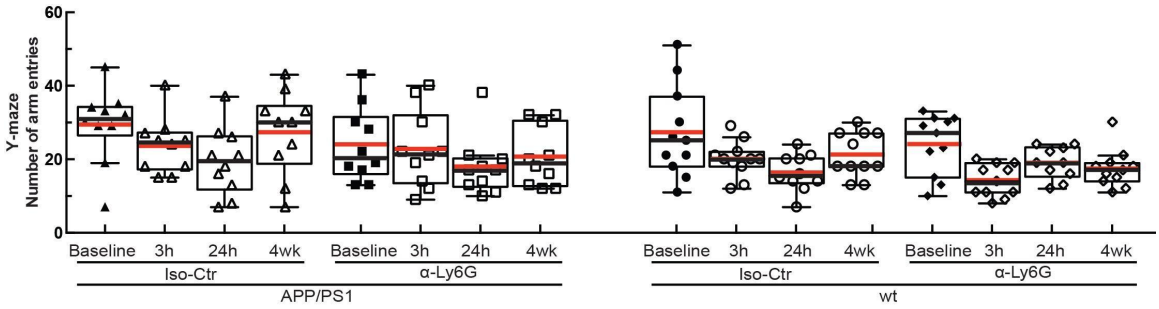

Fig. 4.S12. Number of arm entries in the Y-maze for wild type controls and APP/PS1 animals treated with α-Ly6G or isotype control antibodies. Number of arm entries in the Y-maze measured for 6 minutes for APP/PS1 and wt mice at baseline and at 3h and 24h after a single administration of α-Ly6G or isotype control antibodies, and after 4 weeks of treatment every three days (APP/PS1 Iso-Ctr: 10 mice; APP/PS1 α-Ly6G: 10 mice; wt Iso-Ctr: 11 mice; wt α-Ly6G: 11 mice; no significant differences among groups as determined by Kruskal-Wallis one-way ANOVA).

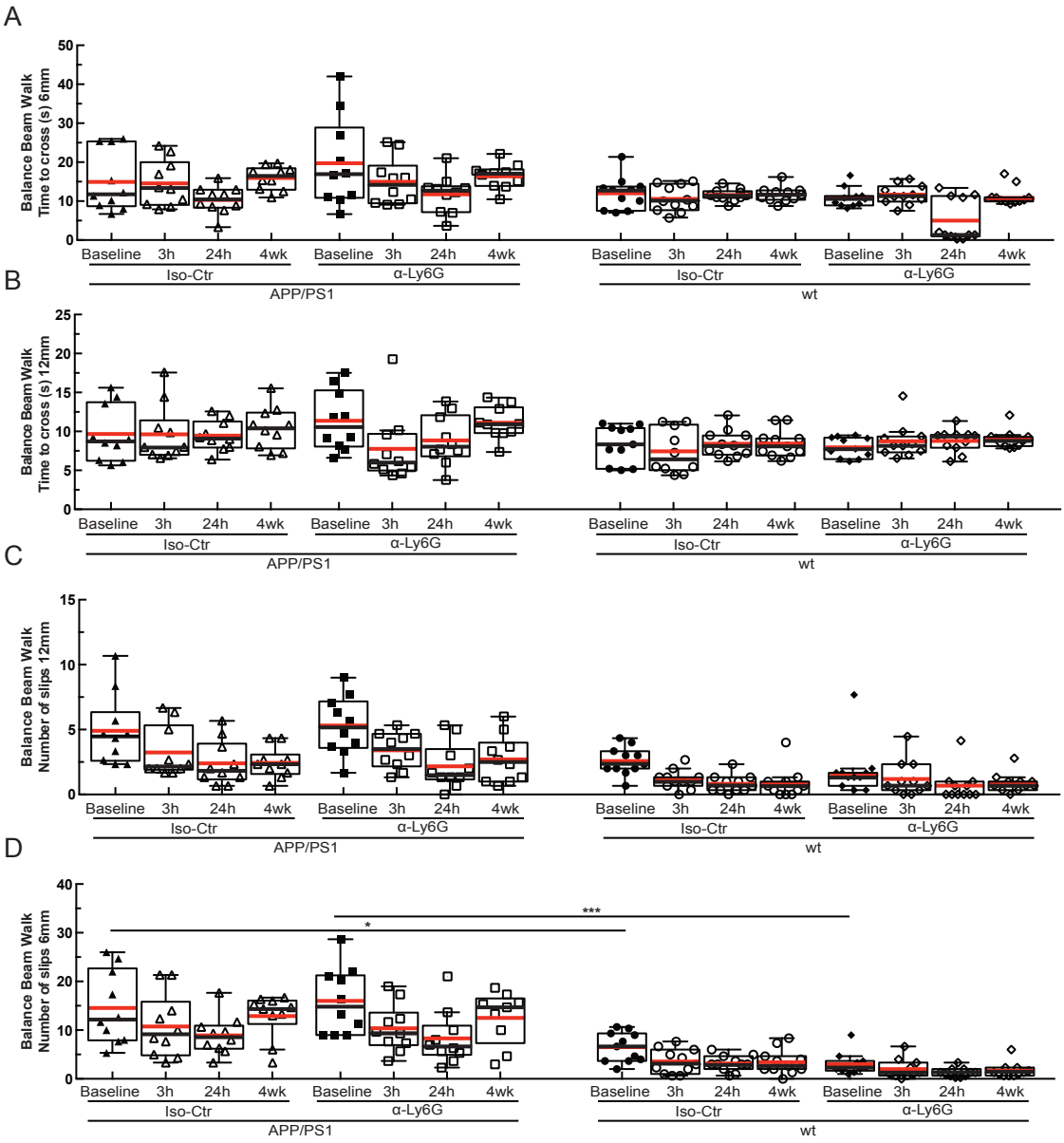

Fig. 4.S13. Balance beam walk (BBW) to measure motor coordination in wildtype controls and APP/PS1 animals treated with α-Ly6G or isotype control antibodies. (A and B) BBW time to cross on a 6- and 12-mm diameter beam, respectively, for APP/PS1 and wild type mice at baseline and at 3h and 24h after a single administration of

α-Ly6G or isotype control antibodies, and after 4 weeks of treatment every three days. APP/PS1 mice showed a modest trend toward taking more time to cross the 6-mm diameter beam as compared to wt controls. (C and D). Number of slips on the BBW for a 6- and 12-mm diameter beam, respectively, for APP/PS1 and wild type mice at baseline and at 3h and 24h after a single administration of α-Ly6G or isotype control antibodies, and after 4 weeks of treatment every three days. For both beam diameters, APP/PS1 mice showed significantly more slips while crossing the beam as compared to wt animals, suggesting a motor deficit in the APP/PS1 mice. All animal groups showed a reduction in the number of slips with subsequent trials, suggesting improved motor coordination with practice. This improvement did not appear different between α-Ly6G and isotype control treated APP/PS1 mice, suggesting that increases in brain blood flow did not influence the motor learning underlying the reduction in the number of slips (APP/PS1 Iso-Ctr: 10 mice; APP/PS1 α-Ly6G: 10 mice; wt Iso-Ctr: 11 mice; wt α-Ly6G: 11 mice; * $p < 0.05$, *** $p < 0.001$, Kruskal-Wallis one-way ANOVA with post-hoc pair-wise comparisons using Dunn's multiple comparison test)

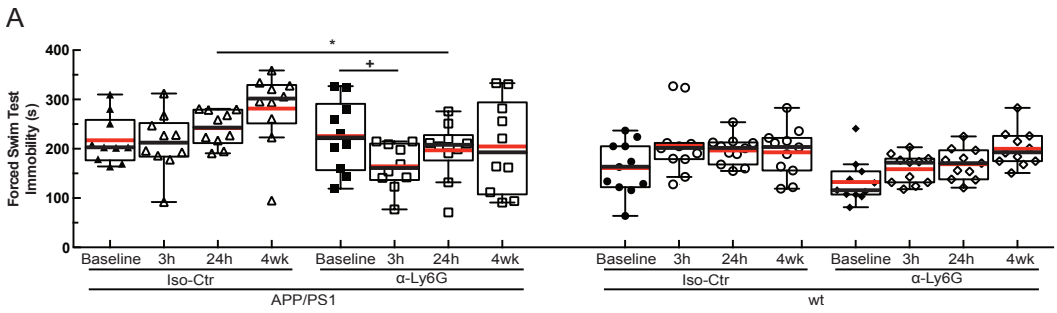

Fig. 4.S14. Depression-like behavior measured as immobility time in a forced swim test for wild type controls and APP/PS1 animals treated with α-Ly6G or isotype control antibodies. Immobility time in forced swim test measured over 6 minutes for APP/PS1 and wt mice at baseline and at 3h and 24h after a single administration of α-Ly6G or isotype control antibodies, and after 4 weeks of treatment every three days (APP/PS1 Iso-Ctr: 10 mice; APP/PS1 α-Ly6G: 10 mice; wt Iso-Ctr: 11 mice; wt α-Ly6G: 11 mice; * $p < 0.05$, Kruskal-Wallis one-way ANOVA with post-hoc pair-wise comparisons using Dunn's multiple comparison test; $p=0.06$ comparison between baseline and 3h for APP/PS1 α-Ly6G, Wilcoxon matched-pairs signed rank test relative to baseline).

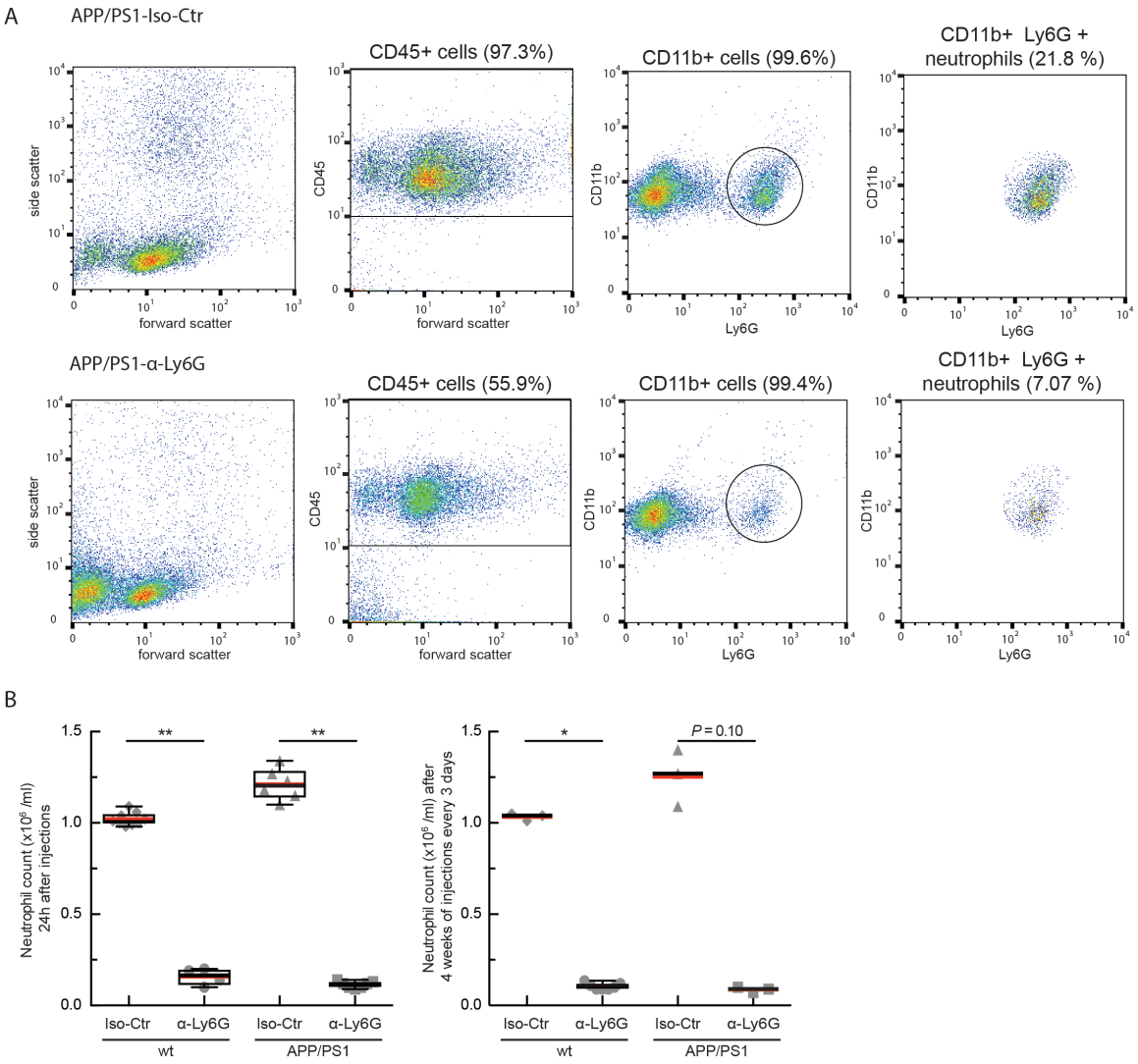

Fig. 4.S15. Treatment with α-Ly6G leads to neutrophil depletion in both APP/PS1 and wildtype control mice. (A) Representative flow cytometry data for blood drawn from APP/PS1 mice 24 hours after treatment with isotype control antibodies (top row) and α-Ly6G (bottom row). Left column shows forward and side scattering from entire population of blood cells (after lysing and removing red blood cells). The second column shows the gate on CD45+ cells, indicating leukocytes. The third column shows expression of CD11b (high for monocytes and neutrophils) and Ly6G (high for neutrophils) for the CD45+ cells. Cells with high expression levels of both CD11b and

Ly6G were considered to be neutrophils (right column). (B) Neutrophil counts for APP/PS1 and wt mice 24 hr after treatment with α-Ly6G or isotype control antibodies (left) and after 4 weeks of treatment every three days (right) (24 hr data: wt Iso-Ctr: n=9 mice; wt Ly6G: n=4; APP/PS1 Iso-Ctr: n=6; APP/PS1 Ly6G: n=7; 4 week data: wt Iso-Ctr: n=3; wt Ly6G: n=7; APP/PS1 Iso-Ctr: n=3; APP/PS1 Ly6G: n=3; *p<0.05, **p<0.01, Mann-Whitney comparison between Iso-Ctr and Ly6G treated animals).

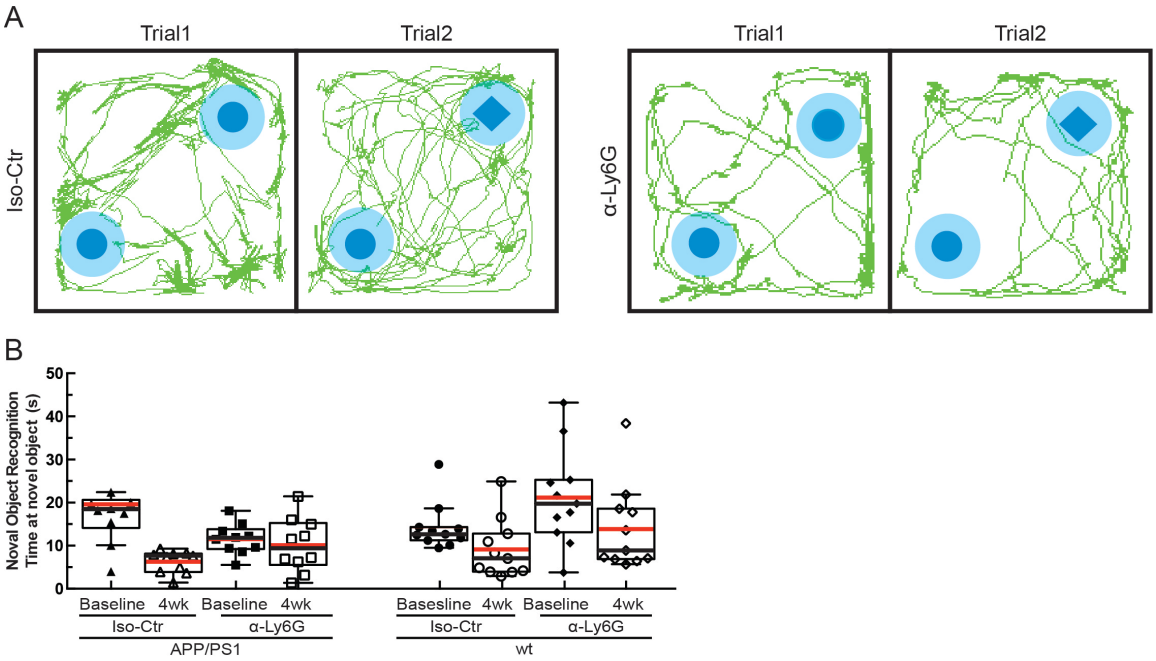

Fig. 4.S16. Representative map of animal location and time spent at the novel object in wild type controls and APP/PS1 animals treated with α-Ly6G or isotype control antibodies. (A) Tracking of mouse nose location from video recording during training and trial phases of novel object recognition task taken 4 weeks after administration of α-Ly6G or isotype control antibodies every three days in APP/PS1 mice. (B) Time spent at the novel object (APP/PS1 Iso-Ctr: 10 mice; APP/PS1 α-Ly6G: 10 mice; wt Iso-Ctr: 11

mice; wt α-Ly6G: 11 mice; no significant differences among groups as determined by Kruskal-Wallis one-way ANOVA).

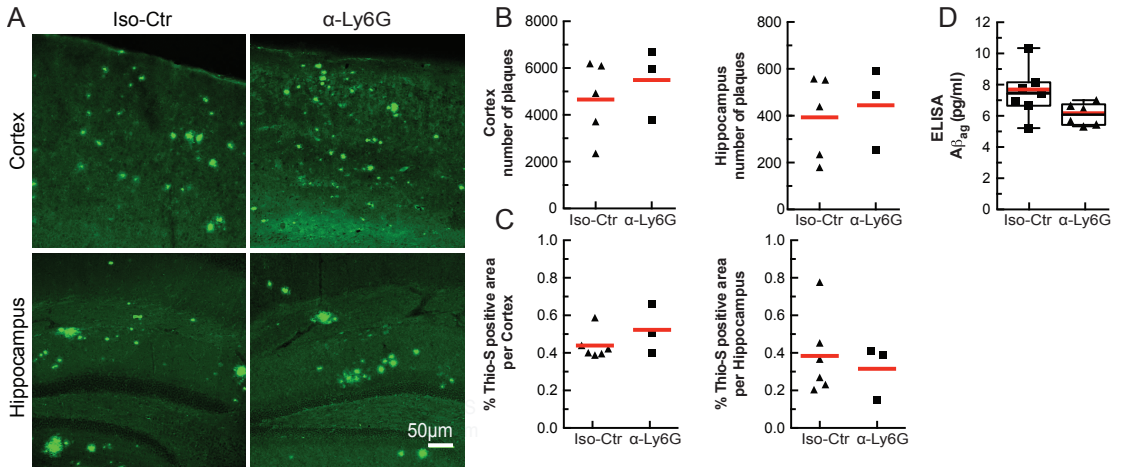

Fig. 4.S17. Amyloid plaque density and concentration of amyloid-beta oligomers were not changed in 11-month-old APP/PS1 animals treated with α-Ly6G every three days for a month. (A) Thioflavin-S staining of amyloid plaques in representative cortical sections (upper 2 panels) and hippocampal sections (lower 2 panels) for APP/PS1 mice treated with isotype control antibodies (left panels) or α-Ly6G (right panels). (B) Number of amyloid plaques in the cortex (left) and hippocampus (right) for APP/PS1 mice after one month of treatment (Iso-Ctr: 5 mice; α-Ly6G: 3 mice). (C) Percentage of tissue section positive for Thioflavin-S in the cortex (left) and hippocampus (right) (Iso-Ctr: 6 mice; α-Ly6G: 3 mice). (D) ELISA measurements of Aβ aggregate concentrations after 4 weeks of treatment with α-Ly6G or isotype control antibodies every three days (Iso-Ctr: 7 mice; α-Ly6G: 6 mice).

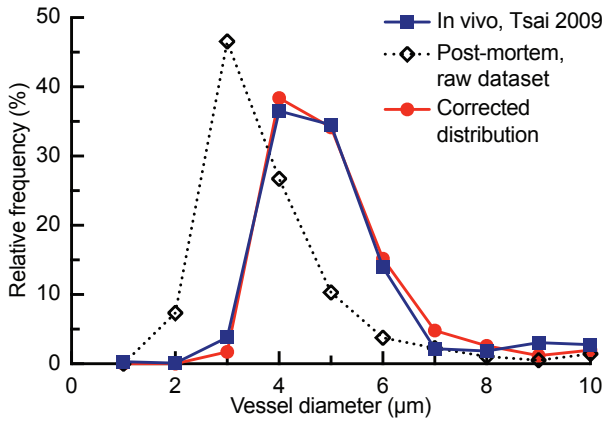

Fig. 4.S18. Histogram of mouse capillary diameters from *in vivo* measurements and post-mortem vascular casts. The diameter correction described in Eq. 3 closely aligned the post mortem diameters to the *in vivo* data**.**

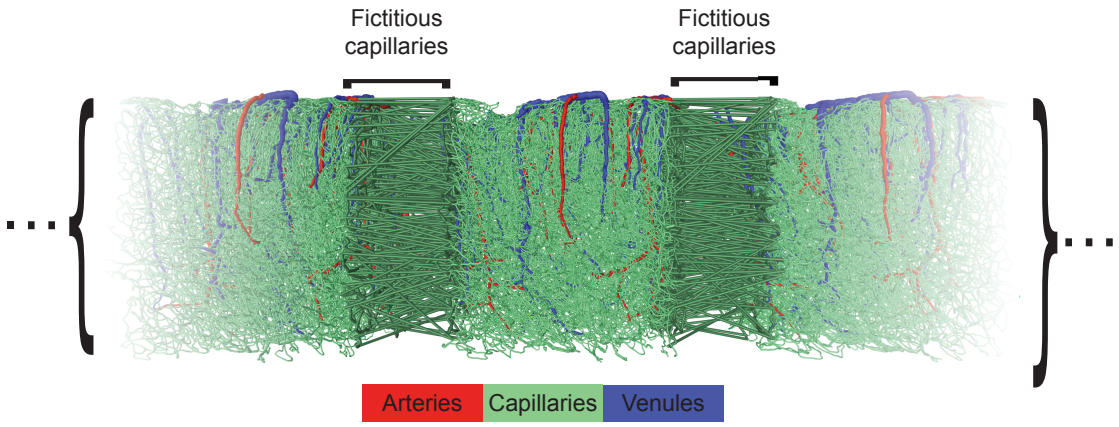

Fig. 4.S19. Illustration of the pseudo-periodic boundary conditions. Vessels categorized as arterioles are labeled in red, venules in blue, and capillaries in green.

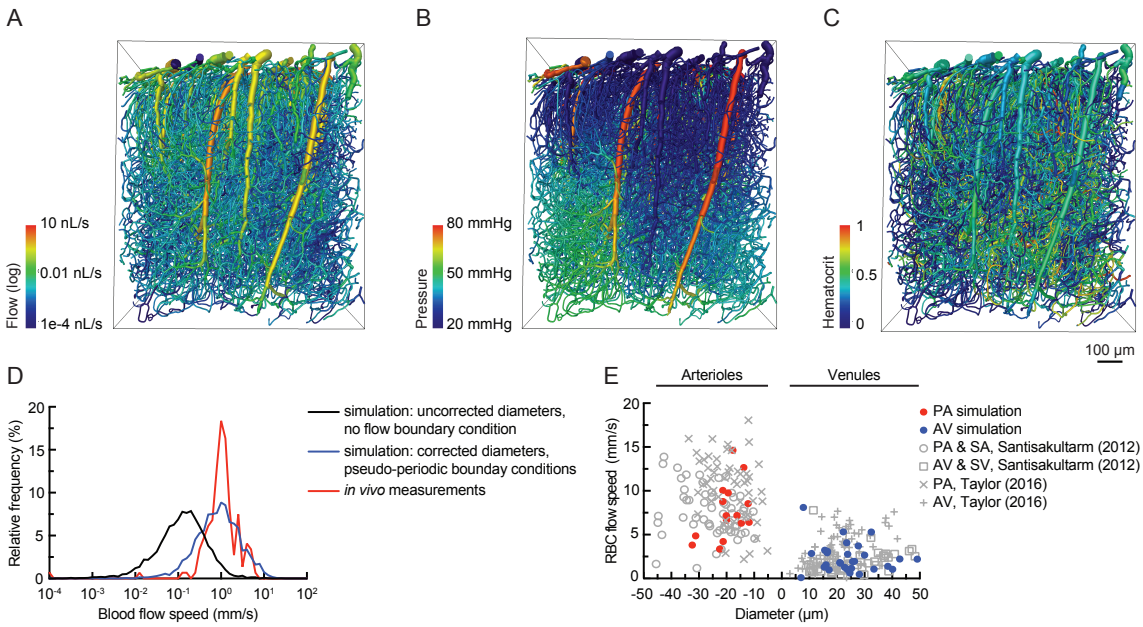

Fig. 4.S20. Validation of simulations. Spatial distribution of simulated blood flow (A), pressure (B), and hematocrit (C) in each vessel in the mouse vascular network. (D) Comparison of red blood cell velocities in capillaries in the top 300-µm of mouse cortex from experimental, *in vivo* measurements (red line), simulations with pseudo-periodic boundary conditions with corrected diameters (blue line), and no-flow boundary conditions without corrected diameters (black line). (E) Relationship between red blood cell speed and vessel diameter in arterioles and venules in calculations (solid red and blue dots) and experimental measurements (grey points).

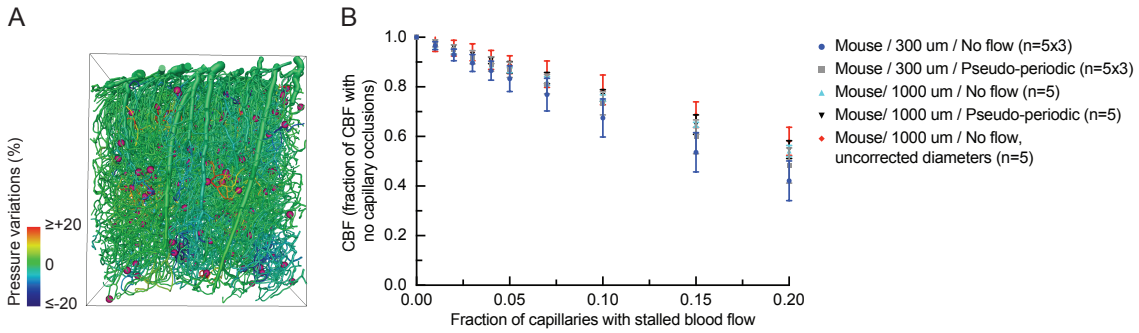

Fig. 4.S21. Calculated blood flow decreases due to capillary stalls was robust with respect to simulation parameters. (A) Pressure changes in mouse cortical vessel network due to randomly placed occlusions in 2% of capillaries. The corresponding flow changes are shown in Fig. 1J. (B) Calculated flow changes due to the occlusion of varying proportions of the capillaries using the full mouse dataset (1000 µm) or truncated datasets (1000x300 µm) with periodic or no flow boundary conditions, and with or without corrected vessel diameters. Error bars represent SD across n independent simulations (whole domain: n=5; 300 µm slices: n=5 for each of 3 slices).

4.8 SUPLEMENTARY TABLE

Table S1: Group sizes, statistical tests, and notes for main Figure panels.

Figure panel	Groups compared	Statistical tests and Notes
1C, D	APP/PS1: 28 mice, ~22,400 capillaries wt: 12 mice,	Mann-Whitney, ****p<0.0001 Each data point represents one mouse in which > 800 capillaries were scored as flowing or stalled. The lines in panel D represent a sliding average with a

	~9,600 capillaries	10-week window and the shaded areas represent 95% confidence intervals.
1F	APP/PS1: 7 mice Stalled: n ~ 120 Flowing: n = ~ 8,700	
1G	APP/PS1: 7 mice Stalled: n ~ 120 Flowing: n = ~ 8,600	
1J		Error bars represent SD across for five independent simulations.
2B	APP/PS1: 10 mice, 235 stalled capillaries	Error bars represent 95% confidence intervals.
2C	Stalled: n = 116 Flowing: n = 8,431	Mann-Whitney, ****p<0.0001
2D	APP/PS1: 7 mice Stalled: n ~ 120 Flowing: n ~ 9,000	
2E	APP/PS1: 3 mice, 31 capillaries	
2G	APP/PS1: 4 mice, 49 stalled capillaries followed from first	

	imaging session	
3A	α-Ly6G: 6 mice, ~4,800 capillaries Iso-Ctr: 6 mice, ~4,800 capillaries	Mann-Whitney, **p<0.01
3C	young APP/PS1 Iso-Ctr: 5 mice, 32 arterioles old APP/PS1 Iso-Ctr: 3 mice, 18 arterioles young wt α-Ly6G: 5 mice, 30 arterioles young APP/PS1 α-Ly6G: 5 mice, 33 arterioles old APP/PS1 α-Ly6G: 3 mice, 22 arterioles	Kruskal-Wallis one-way ANOVA with post-hoc using Dunn's multiple comparison correction, **p<0.01 and ***p<0.001
3E	wt α-Ly6G: 10 mice APP/PS1 α-Ly6G: 10 mice APP/PS1 Iso-Ctr: 10	Ordinary one-way ANOVA with post hoc using Tukey's multiple comparison correction to compare across groups, *p<0.05 Paired t-test to compare baseline and after treatment

	mice	within a group, ++p<0.01 Each data point indicates a single mouse and lines connecting baseline and after measurements indicate the same animal.
4C, D, E	APP/PS1 Iso-Ctr: 10 mice APP/PS1 α-Ly6G: 10 mice wt α-Ly6G: 11 mice wt Iso-Ctr: 11 mice	Kruskal-Wallis one-way ANOVA with post-hoc using Dunn's multiple comparison correction to compare across groups, *p<0.05 and **p<0.01 Wilcoxon matched-pairs signed rank test relative to the baseline measurement to compare baseline and after treatment within a group, +p<0.05 and ++p<0.01
4F	Iso-Ctr: 6 mice α-Ly6G: 7 mice	Mann-Whitney **p <0.01

References

1. Y. Iturria-Medina et al., Early role of vascular dysregulation on late-onset Alzheimer's disease based on multifactorial data-driven analysis. *Nature communications* **7**, 11934 (2016).
2. W. Dai et al., Mild cognitive impairment and alzheimer disease: patterns of altered cerebral blood flow at MR imaging. *Radiology* **250**, 856-866 (2009).
3. F. J. Wolters et al., Cerebral Perfusion and the Risk of Dementia: A Population-Based Study. *Circulation*, (2017).

4. M. Wiesmann et al., Hypertension, cerebrovascular impairment, and cognitive decline in aged AbetaPP/PS1 mice. *Theranostics* **7**, 1277-1289 (2017).
5. H. Li et al., Vascular and parenchymal amyloid pathology in an Alzheimer disease knock-in mouse model: interplay with cerebral blood flow. *Molecular neurodegeneration* **9**, 28 (2014).
6. K. Niwa, K. Kazama, S. G. Younkin, G. A. Carlson, C. Iadecola, Alterations in cerebral blood flow and glucose utilization in mice overexpressing the amyloid precursor protein. *Neurobiology of disease* **9**, 61-68 (2002).
7. R. S. Marshall et al., Recovery of brain function during induced cerebral hypoperfusion. *Brain* **124**, 1208-1217 (2001).
8. L. Wang et al., Chronic cerebral hypoperfusion induces memory deficits and facilitates Abeta generation in C57BL/6J mice. *Experimental neurology* **283**, 353-364 (2016).
9. R. Radde et al., Abeta42-driven cerebral amyloidosis in transgenic mice reveals early and robust pathology. *EMBO reports* **7**, 940-946 (2006).
10. M. A. Chishti et al., Early-onset amyloid deposition and cognitive deficits in transgenic mice expressing a double mutant form of amyloid precursor protein 695. *The Journal of biological chemistry* **276**, 21562-21570 (2001).
11. N. Nishimura et al., Targeted insult to subsurface cortical blood vessels using ultrashort laser pulses: three models of stroke. *Nature methods* **3**, 99-108 (2006).
12. P. S. Tsai et al., Correlations of neuronal and microvascular densities in murine cortex revealed by direct counting and colocalization of nuclei and vessels. *The Journal of neuroscience* **29**, 14553-14570 (2009).

13. F. Lauwers, F. Cassot, V. Lauwers-Cances, P. Puwanarajah, H. Duvernoy, Morphometry of the human cerebral cortex microcirculation: general characteristics and space-related profiles. *NeuroImage* **39**, 936-948 (2008).
14. S. Lorthois, F. Cassot, F. Lauwers, Simulation study of brain blood flow regulation by intra-cortical arterioles in an anatomically accurate large human vascular network. Part II: flow variations induced by global or localized modifications of arteriolar diameters. *NeuroImage* **54**, 2840-2853 (2011).
15. R. Deane, R. D. Bell, A. Sagare, B. V. Zlokovic, Clearance of amyloid-beta peptide across the blood-brain barrier: implication for therapies in Alzheimer's disease. *CNS & neurological disorders drug targets* **8**, 16-30 (2009).
16. A. E. Roher et al., Cerebral blood flow in Alzheimer's disease. *Vascular health and risk management* **8**, 599-611 (2012).
17. K. Niwa et al., A beta-peptides enhance vasoconstriction in cerebral circulation. *American journal of physiology. Heart and circulatory physiology* **281**, H2417-2424 (2001).
18. E. Farkas, P. G. Luiten, Cerebral microvascular pathology in aging and Alzheimer's disease. *Progress in neurobiology* **64**, 575-611 (2001).
19. S. M. Landau et al., Associations between cognitive, functional, and FDG-PET measures of decline in AD and MCI. *Neurobiology of aging* **32**, 1207-1218 (2011).
20. Y. Chen et al., Voxel-level comparison of arterial spin-labeled perfusion MRI and FDG-PET in Alzheimer disease. *Neurology* **77**, 1977-1985 (2011).
21. J. Royea, L. Zhang, X. K. Tong, E. Hamel, Angiotensin IV Receptors Mediate the Cognitive and Cerebrovascular Benefits of Losartan in a Mouse Model of

Alzheimer's Disease. *The Journal of neuroscience : the official journal of the Society for Neuroscience* **37**, 5562-5573 (2017)

22. A. Villringer et al., Imaging of leukocytes within the rat brain cortex in vivo. *Microvascular research* **42**, 305-315 (1991).
23. M. Ishikawa et al., Leukocyte plugging and cortical capillary flow after subarachnoid hemorrhage. Acta neurochirurgica 158, 1057-1067 (2016).
24. R. A. Kloner, No-reflow phenomenon: maintaining vascular integrity. *Journal of cardiovascular pharmacology and therapeutics* **16**, 244-250 (2011).
25. R. L. Engler, G. W. Schmid-Schonbein, R. S. Pavelec, Leukocyte capillary plugging in myocardial ischemia and reperfusion in the dog. *The American journal of pathology* **111**, 98-111 (1983).
26. R. Chibber, B. M. Ben-Mahmud, S. Chibber, E. M. Kohner, Leukocytes in diabetic retinopathy. *Current diabetes reviews* **3**, 3-14 (2007).
27. T. P. Santisakultarm et al., Stalled cerebral capillary blood flow in mouse models of essential thrombocythemia and polycythemia vera revealed by in vivo two-photon imaging. *Journal of thrombosis and haemostasis* : JTH **12**, 2120-2130 (2014).
28. O. O. Ilesanmi, Pathological basis of symptoms and crises in sickle cell disorder: implications for counseling and psychotherapy. *Hematology reports* **2**, e2 (2010).
29. G. Zuliani et al., Markers of endothelial dysfunction in older subjects with late onset Alzheimer's disease or vascular dementia. *Journal of the neurological sciences* **272**, 164-170 (2008).
30. C. Iadecola, Vascular and Metabolic Factors in Alzheimer's Disease and Related Dementias: Introduction. *Cellular and molecular neurobiology* **36**, 151-154 (2016).

31. J. X. Wang et al., Ly6G ligation blocks recruitment of neutrophils via a beta2-integrin-dependent mechanism. *Blood* **120**, 1489-1498 (2012).
32. E. Zenaro et al., Neutrophils promote Alzheimer's disease-like pathology and cognitive decline via LFA-1 integrin. *Nature medicine* **21**, 880-886 (2015).
33. P. Blinder et al., The cortical angiome: an interconnected vascular network with noncolumnar patterns of blood flow. *Nature neuroscience* **16**, 889-897 (2013).
34. J. L. Jankowsky et al., Mutant presenilins specifically elevate the levels of the 42 residue beta-amyloid peptide in vivo: evidence for augmentation of a 42-specific gamma secretase. *Human molecular genetics* **13**, 159-170 (2004).
35. W. E. Klunk et al., Imaging Abeta plaques in living transgenic mice with multiphoton microscopy and methoxy-X04, a systemically administered Congo red derivative. *Journal of neuropathology and experimental neurology* **61**, 797-805 (2002).
36. T. A. Pologruto, B. L. Sabatini, K. Svoboda, ScanImage: flexible software for operating laser scanning microscopes. *Biomedical engineering online 2*, **13** (2003).
37. D. A. Dombeck, A. N. Khabbaz, F. Collman, T. L. Adelman, D. W. Tank, Imaging large-scale neural activity with cellular resolution in awake, mobile mice. *Neuron* **56**, 43-57 (2007).
38. E. W. Dijkstra, A note on two problems in connexion with graphs. *Numerische Mathematik* Volume **1**, pp 269–271 (1959).
39. N. Otsu, A threshold selection method from gray-level histogram. *IEEE Trans. Syst. Man Cybern*. vol. **9**, pp. 62-66 (1979).
40. J. Lim, Two-Dimensional Signal and Image Processing. NJ, *Englewood Cliffs:Prentice Hall,* (1990).

41. T. P. Santisakultarm et al., In vivo two-photon excited fluorescence microscopy reveals cardiac- and respiration-dependent pulsatile blood flow in cortical blood vessels in mice. *American journal of physiology. Heart and circulatory physiology* **302**, H1367-1377 (2012).
42. G. Paxinos, K. Franklin, The mouse brain in stereotaxic coordinate. *Elsevier Academic Press*, (2004).
43. S. G. Kim, Quantification of relative cerebral blood flow change by flow-sensitive alternating inversion recovery (FAIR) technique: application to functional mapping. *Magnetic resonance in medicine* **34**, 293-301 (1995).
44. P. Herscovitch, M. E. Raichle, What is the correct value for the brain--blood partition coefficient for water? *Journal of cerebral blood flow and metabolism* **5**, 65-69 (1985).
45. F. Kober et al., High-resolution myocardial perfusion mapping in small animals in vivo by spin-labeling gradient-echo imaging. *Magnetic resonance in medicine* **51**, 62-67 (2004).
46. Z. J. Taylor et al., Microvascular basis for growth of small infarcts following occlusion of single penetrating arterioles in mouse cortex. *Journal of cerebral blood flow and metabolism* **36**, 1357-1373 (2016).
47. F. Cassot, F. Lauwers, C. Fouard, S. Prohaska, V. Lauwers-Cances, A novel three-dimensional computer-assisted method for a quantitative study of microvascular networks of the human cerebral cortex. *Microcirculation* **13**, 1-18 (2006).
48. H. M. Duvernoy, S. Delon, J. L. Vannson, Cortical blood vessels of the human brain. *Brain research bulletin* **7**, 519-579 (1981).
49. F. Reina-De La Torre, A. Rodriguez-Baeza, J. Sahuquillo-Barris, Morphological

characteristics and distribution pattern of the arterial vessels in human cerebral cortex: a scanning electron microscope study. *The Anatomical record* **251**, 87-96 (1998).

50. A. R. Pries, T. W. Secomb, P. Gaehtgens, J. F. Gross, Blood flow in microvascular networks. Experiments and simulation. *Circulation research* **67**, 826-834 (1990).
51. A. R. Pries, T. W. Secomb, P. Gaehtgens, Biophysical aspects of blood flow in the microvasculature. *Cardiovascular research* **32**, 654-667 (1996).
52. A. R. Pries, B. Reglin, T. W. Secomb, Structural response of microcirculatory networks to changes in demand: information transfer by shear stress. *American journal of physiology. Heart and circulatory physiology* **284**, H2204-2212 (2003).
53. S. Roman, A. Merlo, P. Duru, F. Risso, S. Lorthois, Going beyond 20 mum-sized channels for studying red blood cell phase separation in microfluidic bifurcations. *Biomicrofluidics* **10**, 034103 (2016).
54. D. E. Bragin, R. C. Bush, W. S. Muller, E. M. Nemoto, High intracranial pressure effects on cerebral cortical microvascular flow in rats. *Journal of neurotrauma* **28**, 775-785 (2011).
55. F. Schmid, P. S. Tsai, D. Kleinfeld, P. Jenny, B. Weber, Depth-dependent flow and pressure characteristics in cortical microvascular networks. *PLoS computational biology* **13**, e1005392 (2017).
56. R. C. Team, R: A language and environment for statistical computing. *R Foundation for Statistical Computing*. (2013).
57. W. R. Brown, C. R. Thore, Review: cerebral microvascular pathology in ageing and neurodegeneration. *Neuropathology and applied neurobiology* **37**, 56-74 (2011).

CHAPTER 5

CEREBRAL MICROBLEEDS, CSF P-TAU, AND COGNITIVE DECLINE: SIGNIFICANCE OF ANATOMIC DISTRIBUTION

This chapter presents an extensive analysis of the correlation between the anatomical location of brain microbleeds vs. CSF beta-amyloid, CSF p-tau, and longitudinal cognitive decline. My contribution to this manuscript was primarily in the acquisition, curation and initial analysis of the data obtained from the Alzheimer's Disease Neuroimaging Initiative (ADNI) (adni.loni.usc.edu), drafting of the first version of the manuscript, and contributing to the intellectual development of the study, while Gloria Chiang and others completed the final data analysis and final version of the manuscript. While I am not the first author on this work and thus consider it a secondary contribution, I include the full manuscript for clarity and completeness.

This work is published in *American Journal of Neuroradiology*. The citation is:

Chiang GC, Cruz Hernandez JC, Kantarci K, Jack CR Jr, Weiner MW (2015) Cerebral microbleeds, CSF p-Tau, and cognitive decline: significance of anatomic distribution. AJNR Am J Neuroradiol 36:1635–41. doi:10.3174/ajnr.A4351

5.1 ABSTRACT

Background and Purpose—Cerebral microbleeds are associated with aging, hypertension, and Alzheimer's disease. Microbleeds in a lobar distribution are believed to reflect underlying amyloid angiopathy, whereas microbleeds in the deep gray matter and infratentorial brain are commonly seen with hypertension. However, it is unknown how microbleeds in either distribution are related to Alzheimer's pathogenesis. The purpose of this analysis was to test whether lobar and deep gray/infratentorial microbleeds demonstrate differential associations with CSF beta-amyloid, CSF p-tau, and longitudinal cognitive decline.

Materials and Methods—626 subjects - 151 cognitively normal, 389 with mild cognitive impairment, and 86 with Alzheimer's disease - from the Alzheimer's Disease Neuroimaging Initiative who had 3 Tesla MRI scans and a lumbar puncture were included in the analysis. The number and location of microbleeds were visually assessed. Associations between lobar or deep gray/infratentorial microbleeds with levels of CSF beta-amyloid, abnormal CSF p-tau, and longitudinal cognitive decline were assessed using ordinary least squares, logistic, and mixed- effects regression models, adjusting for covariates.

Results—Having three or more lobar microbleeds are associated with lower levels of CSF beta- amyloid ($p=0.001$). Adjusting for CSF beta-amyloid, lobar microbleeds are independently associated with a higher likelihood of having an abnormal CSF p-tau level ($p=0.004$). Lobar microbleeds are associated with accelerated longitudinal cognitive

decline (p=0.007). Deep gray/ infratentorial microbleeds demonstrated no significant associations.

Conclusion—Microbleed distribution demonstrated different associations with amyloid, tau, and cognition. Lobar and deep gray/infratentorial microbleeds should be considered separately with regards to Alzheimer's disease pathogenesis.

5.2 INTRODUCTION

Cerebral microbleeds are common findings on gradient-echo (GRE) and susceptibility-weighted magnetic resonance imaging (MRI) sequences, typically associated with aging, hypertension, and Alzheimer's disease (AD). Approximately 36% of people over the age of 80 have microbleeds, compared to only 7% of people who are 45–50 years old [1]. Hypertensive individuals are four times more likely than the general population to have microbleeds [2], particularly in association with other signs of small vessel disease, such as white matter hyperintensities and lacunar infarcts [3,4]. People with mild cognitive impairment (MCI) and Alzheimer's disease (AD) have microbleeds with a reported prevalence of 20– 43% in MCI and 18–32% in AD, compared to 0–19% in cognitively normal individuals [5]. In the setting of AD, microbleeds are associated with global brain amyloidosis, seen with increased uptake on positron emission tomography (PET) scans using ^{18}F-florbetapir (PiB) [6] and decreased levels of CSF beta-amyloid [5].

The anatomical distribution of microbleeds is believed to reflect their underlying pathology. Microbleeds located in the deep gray matter and infratentorial brain are typically seen in hypertensive individuals [2,7] and correspond to foci of hemosiderin

leakage from abnormal small blood vessels [8]. Conversely, microbleeds in the setting of aging and AD are typically lobar, at the cortico-subcortical junction [2,7] and correspond to beta-amyloid deposition along vessel walls [9], also known as amyloid angiopathy. However, it remains unclear whether microbleeds, either from hypertension or amyloid angiopathy, relate to tau pathology or cognitive changes leading to Alzheimer's pathogenesis [10], independent of global brain amyloidosis.

The purpose of our analysis was to determine whether the distribution of microbleeds, either lobar or deep gray/infratentorial, may have differential associations with downstream events in Alzheimer's pathogenesis. Specifically, using data from the multicenter Alzheimer's Disease Neuroimaging Initiative (ADNI) (adni.loni.usc.edu) [11], we tested the hypotheses that lobar microbleeds (1) are associated with brain amyloidosis, reflected by lower levels of CSF beta-amyloid, (2) predict the presence of tau pathology, adjusting for overall brain amyloidosis, and (3) predict greater longitudinal cognitive decline.

5.3 RESULTS

5.3.1 Subjects Characteristics

Subject characteristics are presented in Table 5.1. Four hundred and seven of the 626 (65%) subjects had no microbleeds, whereas 219 (35%) had at least 1 microbleed. Of the 219 subjects with microbleeds, 192 (87%) had at least 1 lobar microbleed and 27 (12%) had only deep gray/infratentorial microbleeds. As expected, subjects with microbleeds were older in age ($p<0.001$) [1]. In addition, those with lobar microbleeds, either alone or

in combination with deep gray/infratentorial microbleeds, had a greater proportion of APOE4 carriers (p=0.03), which has also been previously described [1].

Table 5.1 Baseline group characteristics[a]

	Microbleeds absent		Microbleeds present			
		P Value[b]	Lobar microbleeds only	Mixed lobar and deep gray or infratentorial microbleeds	Deep gray/infratentorial microbleeds only	P Value[c]
Number of subjects	407		163	29	27	
Age (years)	72 [7.6]	<0.001[d]	74 [7.0]	77 [6.4]	77 [9.0]	0.06
Gender (male:female)	218:189	0.15	100:63	17:12	14:13	0.64
Education (years)	16 [2.6]	0.24	16 [2.9]	16 [2.9]	16 [2.3]	0.78
% with APOE4 % with APOE2 allele	43 7	0.15 >0.99	53 6	52 7	26 19	0.03[e] 0.06
% NL % MCI % AD	26 61 12	0.14 0.80 0.18	20 61 18	10 79 10	33 56 11	0.10 0.33 0.41

[a]Data are mean [standard deviation]. [b]P-values comparing baseline variables between those without microbleeds and with microbleeds (combining the 3 groups with different types of microbleeds) [c]P-values comparing baseline variables among the three groups with microbleeds [d]Significance by Wilcoxon rank-sum test. [e]Significance by Chi-squared test.

5.3.2 Having 3 or more lobar microbleeds are associated with levels of CSF Abeta, whereas deep gray/infratentorial microbleeds are not

Adjusting for covariates, having at least 1 lobar microbleed was associated with greater brain amyloidosis, reflected by lower CSF Abeta, although this association did not reach statistical significance (coeff=−0.04, p=0.08). However, accounting for increasing numbers of microbleeds, having three (coeff=−0.30, p=0.001) or more than three (coeff=−0.18, p=0.001) lobar microbleeds was also associated with lower levels of CSF Abeta (Table 5.2). Deep gray/infratentorial microbleeds were not associated with CSF Abeta (p=0.60), and increasing numbers of deep gray/infratentorial microbleeds also were not associated with CSF Abeta (p=0.27–0.99).

Table 5.2 Regression model demonstrating association between lobar microbleeds and CSF beta-amyloid (log- transformed)

CSF Abeta (log-transformed)	Coefficient [95% CI]	p-value
1 lobar microbleed	–0.005 [–0.057, 0.047]	0.86
2 lobar microbleeds	–0.029 [–0.12, 0.057]	0.51
3 lobar microbleeds	–0.30 [–0.48, –0.12]	0.001
More than 3 lobar microbleeds	–0.18 [–0.29, –0.071]	0.001
Age	–0.007 [–0.0099, –0.0042]	<0.001
Male gender	–0.013 [–0.056, –0.030]	0.55
Years of education	0.004 [–0.0044, 0.012]	0.38
APOE4	–0.23 [–0.28, –0.19]	<0.001
APOE2	0.059 [–0.022, 0.14]	0.15
MCI	–0.078 [–0.13, –0.028]	0.002
AD	–0.26 [–0.33, –0.19]	<0.001

5.3.3 Lobar microbleeds are associated with a higher likelihood of having an abnormal CSF p- tau level, independent of CSF Abeta. Deep gray/infratentorial microbleeds are not associated with abnormal CSF p-tau levels

Using logistic regression, adjusting for the CSF Abeta level, having at least 1 lobar microbleed was associated with more than double the odds of having an abnormal CSF p-tau level (p=0.004). On the other hand, having deep gray/infratentorial microbleeds was not associated with abnormal CSF p-tau levels (p=0.97). Unlike with CSF Abeta, no dose- response relationship was visualized; having one lobar microbleed was most associated with an abnormal CSF p-tau level, with an odds ratio of 2.8 (p=0.001) (Table 5.3).

Table 5.3 Regression model demonstrating association between lobar microbleeds and likelihood of abnormal CSF phosphorylated tau

Abnormal CSF p-tau	Odds ratio [95% CI]	p-value
1 lobar microbleed	2.82 [1.52, 5.24]	0.001
2 lobar microbleeds	1.24 [0.51, 3.01]	0.63
3 lobar microbleeds	0.37 [0.081, 1.73]	0.21
More than 3 microbleeds	3.19 [0.40, 25.60]	0.27
Abnormal CSF Abeta	3.40 [2.16, 5.34]	<0.001
Age	1.01 [0.99, 1.04]	0.33
Male gender	0.93 [0.61, 1.42]	0.74
Years of education	0.98 [0.90, 1.06]	0.56
APOE4	2.34 [1.42, 3.84]	0.001
APOE2	1.02 [0.52, 2.02]	0.95
MCI	1.05 [0.67, 1.67]	0.83
AD	3.5 [1.15, 10.70]	0.03

5.3.4 Lobar microbleeds are associated with accelerated longitudinal cognitive decline

Using a linear mixed-effects model and adjusting for covariates, including CSF Abeta level and diagnostic group, having at least 1 lobar microbleed was significantly associated with accelerated longitudinal change in ADAS scores (p=0.007) of 1.4 points per year compared to 0.8 points per year for those without lobar microbleeds. Furthermore, having more than 3 lobar microbleeds was significantly associated with an increase of 2.3 points per year (p<0.001) (Table 5.4). Deep gray/infratentorial microbleeds were not associated with change in ADAS scores (p=0.31).

Table 5.4 Mixed effects regression model demonstrating association between lobar microbleeds and longitudinal change in ADAS

	Annual change in ADAS [95% CI]	p-value
No lobar microbleeds	0.78 [0.52, 1.03]	<0.001
1 lobar microbleed	1.35 [0.91, 1.78]	0.025
2 lobar microbleeds	0.36 [–0.61, 1.33]	0.41
3 lobar microbleeds	0.50 [–2.07, 3.06]	0.83
More than 3 lobar microbleeds	2.34 [1.51, 3.18]	<0.001

5.4 DISCUSSION

The major findings of our analysis are: (1) having 3 or more lobar microbleeds are associated with global brain amyloidosis, whereas deep gray/infratentorial microbleeds are not, (2) lobar microbleeds, unlike deep gray/infratentorial microbleeds, are associated with elevated CSF p-tau, although without a dose-response relationship, and (3) lobar microbleeds, unlike deep gray/infratentorial microbleeds, are associated with accelerated longitudinal cognitive decline. Taken together, our analysis suggests a differential association of lobar versus deep gray/infratentorial microbleeds with Alzheimer's pathogenesis, suggesting the importance of lobar microbleeds in prognostication, independent of CSF Abeta levels.

The first major finding that lobar microbleeds are associated with greater overall brain amyloidosis is concordant with prior studies that have shown lower CSF Abeta levels [3,18,19] and higher uptake on PET amyloid scans [5,6] in people with microbleeds. Prior papers have also suggested that microbleeds that are lobar in location are more suggestive of underlying amyloid angiopathy [2,7,9], which is seen concomitantly in 78–98% of Alzheimer's disease brains postmortem [20]. The finding that only higher numbers of lobar microbleeds were found to be associated with CSF Abeta suggests that severe amyloid angiopathy is more related to overall brain amyloidosis and may contribute to the disease process. On the other hand, deep gray/infratentorial microbleeds, which are more typically associated with hypertension, were not associated with CSF Abeta. Prior work has also demonstrated that deep gray, not lobar, microbleeds are associated with small vessel disease [21]. Taken together, hypertension may produce

deep gray/infratentorial microbleeds and small vessel changes, but is likely involved in Alzheimer's pathogenesis from a non-amyloid pathway, such as decreased cognitive reserve.

The second major finding is that having at least 1 lobar microbleed, unlike deep gray/ infratentorial microbleeds, was associated with greater odds of having an abnormal level of CSF p-tau, adjusting for CSF Abeta levels. A recent study in a memory clinic population found a similar association between microbleeds and CSF total tau, but not CSF p-tau, in nondemented individuals [19]. The fact that they did not find an association between microbleeds and p-tau may reflect technical differences in the assay or the fact that p-tau is more specific for neurodegeneration in a cohort with more comorbid vascular disease. Nonetheless, both of our studies demonstrated an association between microbleeds and elevated levels of forms of CSF tau. One hypothesis is that microbleeds could reflect damaged microvasculature, resulting in decreased blood flow to neurons, ischemia, neuronal degeneration, and increased tau pathology. Post-mortem, p-tau does appear to have increased aggregation around arteries and arterioles with Abeta in the vessel walls [22]. Alternatively, microbleeds could induce enough inflammation, without duration, to cause elevated CSF p-tau. In an animal model, microhemorrhages were seen to trigger inflammation and activated microglia, macrophages, lymphocytes, [9,23] rather than cell death or ischemia. This inflammation may be sufficient to produce neuronal release of tau into the extracellular space. This inflammation may also contribute to further Alzheimer's pathogenesis. Finally, the presence of lobar microbleeds, reflecting amyloid angiopathy, may suggest that the patients are farther along in the Alzheimer's

disease cascade [10]. In this case, lobar microbleeds, in addition to abnormal CSF Abeta, may signal more severe underlying disease.

The third major finding is that having at least 1 lobar microbleed is associated with accelerated longitudinal cognitive decline. The literature evaluating the association between microbleeds and cognitive decline has been variable, depending on the cohort studied – community-based populations [24-27], people with a history of or suspected stroke [28-31], or memory clinic MCI/AD subjects [3,32-36], – and whether cognition was being evaluated on a cross-sectional [24,28-30,32,33] or longitudinal basis [25,31,34-37]. The majority of these studies demonstrated an association between microbleeds and either global or executive impairment [3,24,26,28-30] cross-sectionally, as well as increased progression of memory impairment [36], greater longitudinal change in MMSE [34], higher likelihood of MCI conversion to AD [25], and increased risk of developing incident dementia [37]. One study also found cognitive improvement after stroke if no microbleeds were present [31], suggesting a detrimental role of microbleeds on cognitive recovery. However, none of these studies adjusted for concomitant Alzheimer's pathology, which may have driven the longitudinal changes in cognition. In our study, the association between lobar microbleeds and accelerated cognitive decline persisted after adjusting for CSF Abeta levels, which suggests that microbleeds alone, perhaps reflecting underlying amyloid angiopathy, lead to cognitive impairment. This mirrors a postmortem study that demonstrated that moderate-to-severe amyloid angiopathy is associated with perceptual speed and episodic memory, even after adjusting for concomitant AD pathology [38]. We also found that having 3 or more lobar

microbleeds were more associated with decreasing cognition, similar to prior studies that found greater cognitive decline with 2 or more [37] or 5 or more [26]. The finding that deep/ infratentorial microbleeds were not associated with cognitive decline is concordant with a prior study [30], although differs from another study that found mixed, not strictly lobar microbleeds, were associated with cognitive decline [37]. The differential effect on cognitive decline secondary to microbleed location, again may hint at differing etiologies of microbleeds.

Our study has several limitations. First, the ADNI is not a community sample. The cohort consisted of more Caucasians, was more highly educated, and had fewer comorbidities than a community population at this age [39]. Furthermore, ADNI subjects were included if they had a low Modified Hachinski score equal or less than 4, excluding people with more severe comorbid vascular pathologies [40]. Therefore, although we did not find a significant effect on hypertension-related deep gray/infratentorial microbleeds on tau pathology and cognition, a significant association may be found in people with more significant vascular disease. As a result, generalization of these findings should be approached with caution and further validation in prospective population-based cohorts is required.

5.5 METHODS

5.5.1 Subjects

The subjects of these analyses were ADNI participants who had 3 Tesla MRI scans and a lumbar puncture for cerebrospinal fluid (CSF) analysis, resulting in 626 individuals - 151

cognitively normal, 389 with mild cognitive impairment (MCI), and 86 with AD. The ADNI is a longitudinal, multicenter observational cohort study designed to identify imaging and biochemical biomarkers for diagnosis and monitoring of AD [12]. The study was approved by the Institutional Review Boards of all of the participating institutions. Informed written consent was obtained from all participants at each site. Subjects who enrolled in ADNI-2 and ADNI-grand opportunity underwent a T2* GRE sequence, which was used to enumerate the number of microbleeds in the brain. Subjects were between the ages of 55 and 90, without clinical or structural evidence of a significant neurological or psychiatric disease, and without systemic medical illness or laboratory abnormalities that would interfere with follow-up. Cognitive function was assessed using the Alzheimer's Disease Assessment Scale (ADAS) [13], which is the most widely used measure for clinical trials.

The ADNI was launched in 2003 by the National Institute on Aging (NIA), the National Institute of Biomedical Imaging and Bioengineering (NIBIB), the Food and Drug Administration (FDA), private pharmaceutical companies, and non-profit organizations, as a $60 million, 5-year public-private partnership. The primary goal of ADNI has been to test whether serial magnetic resonance imaging (MRI), positron emission tomography (PET), other biological markers, and clinical and neuropsychological assessment can be combined to measure the progression of mild cognitive impairment (MCI) and early Alzheimer's disease (AD). Determination of sensitive and specific markers of very early AD progression is intended to aid researchers and clinicians to develop new treatments and monitor their effectiveness, as well as lessen the time and cost of clinical trials. The

Principal Investigator of this initiative is Michael W. Weiner, MD, VA Medical Center and University of California – San Francisco. ADNI is the result of efforts of many coinvestigators from a broad range of academic institutions and private corporations, and subjects have been recruited from over 50 sites across the U.S. and Canada. The initial goal of ADNI was to recruit 800 subjects but ADNI has been followed by ADNI-GO and ADNI-2. To date these three protocols have recruited over 1500 adults to participate in the research, consisting of cognitively normal older individuals, people with early or late MCI, and people with early AD. The follow up duration of each group is specified in the protocols for ADNI-1, ADNI-2 and ADNI-GO. Subjects originally recruited for ADNI-1 and ADNI-GO had the option to be followed in ADNI-2. For up-to-date information, see www.adni-info.org.

5.5.2 MR Image Acquisition

The 3 Tesla MRI protocol included T2* GRE and T1-weighted three-dimensional MPRAGE sequences, which have been described previously (http://adni.loni.usc.edu/methods/ documents/mri-protocols/). Microbleeds were quantified visually by a board-certified neuroradiologist with subspecialty certification (GCC). Microbleeds were defined as hypointense lesions within the brain parenchyma, measuring less than 10mm on the GRE sequence. Only microbleeds that were considered definite were included in the analysis.

Microbleeds were visually classified by location as (1) deep gray matter/infratentorial, if they involved the basal ganglia, thalami, brainstem, or cerebellum, or (2) lobar, if they

involved other regions of the brain parenchyma.

5.5.3 CSF Biomarkers

Subjects included in this analysis underwent lumbar puncture to obtain CSF samples for quantifying levels of CSF beta-amyloid (Abeta) and phosphorylated tau (p-tau) [14]. Briefly, lumbar puncture was performed with a 20- or 24-gauge spinal needle at the baseline visit after an overnight fast. The CSF samples were then transferred into polypropylene transfer tubes, frozen on dry ice within an hour after collection, and shipped on dry ice overnight to a single designated laboratory. After thawing for 1 hour at room temperature and gentle mixing, 0.5 ml aliquots were prepared from these samples. The aliquots were then stored in bar code-labeled polypropylene vials at −80°C and measured using the xMAP Luminex platform (Luminex Corp, Austin, TX) with Innogenetics (INNOBIA AlzBio3, Ghent, Belgium) immunoassay kit-based reagents. Monoclonal antibodies specific for Abeta and p- tau were used as reagents, which have been found to be useful in predicting AD [15]. CSF total tau was not included in this analysis because this value was not available for some of the participants. In addition, p-tau has a higher specificity and negative predictive value in ruling out the presence of AD with 90% probability [16].

5.5.4 APOE Genotyping

All participants underwent APOE genotyping at the baseline visit. Approximately 6 ml of blood were obtained from each participant in an EDTA tube, gently mixed by inversion, and shipped at ambient temperature to a single designated laboratory within 24 hours of

collection for analysis for genotyping.

5.5.5 Statistical Analysis

All statistical analyses were programmed in STATA version 13 (StataCorp, College Station, TX). Comparisons of baseline variables among groups were performed using the Wilcoxon rank-sum test, Fisher exact test, Kruskal Wallis test, and Chi squared test, depending on number of groups and type and distribution of variables.

To test the hypothesis that lobar microbleeds are associated with overall brain amyloidosis, we used ordinary least squares regression with age, gender, years of education, APOE2 and APOE4 status, and diagnostic group (NL, MCI, or AD) as covariates. CSF Abeta values were log-transformed for normality and included as the outcome variable. Lobar microbleeds was first dichotomized as 0 or 1, indicating presence or absence, and used as the predictor. The number of lobar microbleeds was then categorized as an ordinal variable of 0, 1, 2, 3, or greater than 3, to determine whether increasing numbers of lobar microbleeds were associated with greater brain amyloidosis, reflected by decreased CSF Abeta. The regressions were then repeated using deep gray/infratentorial microbleeds, categorized as dichotomous or ordinal variables, to differentiate between microbleeds that may be associated with hypertension and those associated with amyloid angiopathy.

To determine whether lobar microbleeds are associated with tau pathology, we used logistic regression, adjusting for age, gender, years of education, APOE2 and APOE4

status, and diagnostic group. CSF Abeta was also included as a covariate, dichotomized as normal or abnormal based on the previously published cutoff of 192 pg/ml, [17] to determine the effect of microbleeds independent of global brain amyloidosis. We then dichotomized abnormal CSF p-tau using the cutoff of 23 pg/ml, [17] which was used as the outcome variable. Lobar versus deep gray/infratentorial microbleeds were again included as the predictor, either as a dichotomous or ordinal variables.

To determine whether lobar microbleeds are associated with longitudinal change in cognition, we used a linear mixed-effects model: $ADAS_{ij} = (B_0 + \beta_0) + \beta_1 MCH_{ii} + (\beta_2 + \beta_3 MCH_{ii}) t_{ij}$ + covariates + ε_{ij}. $ADAS_{ij}$ represents the ADAS score of subject i at timepoint j, MCH_i represents the presence or absence of lobar microbleeds in each subject, and t_{ij} represents the time interval between ADAS tests. $(B_0 + \beta_0)$ are the coefficients for the random and fixed variations in baseline ADAS scores. The coefficient β_1 represents the fixed effects of having lobar microbleeds at baseline. Finally, $(\beta_2 + \beta_3)$ are the coefficients for time-dependent changes in ADAS scores, irrespective (β_2) and respective (β_3) of presence of microbleeds. The error term ε_{ij} represents random noise.

5.6 CONCLUSION

The distribution of microbleeds is clinically significant because it not only suggests differing underlying pathology (i.e. amyloid angiopathy versus hypertension) as previously reported in the pathological literature, but also is associated with different downstream events in Alzheimer's pathogenesis (i.e. tau and cognitive decline). Clinical

reports, particularly those in older individuals who are being assessed for cognitive decline, should report these microbleeds separately.

5.7 ACKNOWLEDGMENTS

Grant Support: The work was supported in part by NIH National Center for Advancing Translational Sciences/ CTSC grant (UL1 TR000457-06)

Data collection and sharing for this project was funded by the Alzheimer's Disease Neuroimaging Initiative (ADNI) (National Institutes of Health Grant U01 AG024904) and DOD ADNI (Department of Defense award number W81XWH-12-2-0012). ADNI is funded by the National Institute on Aging, the National Institute of Biomedical Imaging and Bioengineering, and through generous contributions from the following: Alzheimer's Association; Alzheimer's Drug Discovery Foundation; Araclon Biotech; BioClinica, Inc.; Biogen Idec Inc.; Bristol- Myers Squibb Company; Eisai Inc.; Elan Pharmaceuticals, Inc.; Eli Lilly and Company; EuroImmun; F. Hoffmann- La Roche Ltd and its affiliated company Genentech, Inc.; Fujirebio; GE Healthcare; ; IXICO Ltd.; Janssen Alzheimer Immunotherapy Research & Development, LLC.; Johnson & Johnson Pharmaceutical Research & Development LLC.; Medpace, Inc.; Merck & Co., Inc.; Meso Scale Diagnostics, LLC.; NeuroRx Research; Neurotrack Technologies; Novartis Pharmaceuticals Corporation; Pfizer Inc.; Piramal Imaging; Servier; Synarc Inc.; and Takeda Pharmaceutical Company. The Canadian Institutes of Health Research is providing funds to support ADNI clinical sites in Canada. Private sector contributions are facilitated by the Foundation for the National Institutes of Health (www.fnih.org). The grantee organization is the Northern California Institute for Research and Education, and

the study is coordinated by the Alzheimer's Disease Cooperative Study at the University of California, San Diego. ADNI data are disseminated by the Laboratory for Neuro Imaging at the University of Southern California.

5.8 SUPPLEMENTARY MATERIALS

Abbreviations

CSF cerebrospinal fluid

p-tau phosphorylated tau-181

Abeta beta-amyloid

References

1. Poels MM, Vernooij MW, Ikram MA, et al. Prevalence and risk factors of cerebral microbleeds: an update of the Rotterdam scan study. Stroke. 2010; 41:S103–106. [PubMed: 20876479]

2. Cordonnier C, Al-Shahi S, Wardlaw J. Spontaneous brain microbleeds: systematic review, subgroup analyses, and standards for study design and reporting. Brain. 2007; 130:1988–2003. [PubMed: 17322562]

3. Goos JD, Kester MI, Barkhof F, et al. Patients with Alzheimer disease with multiple microbleeds: relation with cerebrospinal fluid biomarkers and cognition. Stroke. 2009; 40:3455–3460. [PubMed: 19762705]

4. Wardlaw JM, Lewis SC, Keir SL, et al. Cerebral microbleeds are associated with lacunar stroke defined clinically and radiologically, independently of white matter lesions.

5. Yates PA, Villemagne VL, Ellis KA, et al. Cerebral microbleeds: a review of clinical, genetic, and neuroimaging associations. Front Neurol. 2014; 4:205. [PubMed: 24432010]

6. Kantarci K, Gunter JL, Tosakulwong N, et al. Focal hemosiderin deposits and beta-amyloid load in the ADNI cohort. Alzheimers Dement. 2013; 9:S116–123. [PubMed: 23375568]

7. Park J, Seo WS, Kim C, et al. Pathogenesis of cerebral microbleeds: in vivo imaging of amyloid and subcortical ischemic small vessel disease in 226 individuals with cognitive impairment. Ann Neurol. 2013; 73:584–593. [PubMed: 23495089]

8. Fazekas F, Kleinert R, Roob G, et al. Histopathologic analysis of foci of signal loss on gradident- echo T2* weighted magnetic resonance images in patients with spontaneous intracerebral hemorrhage: evidence of microangiopathy-related microbleeds. AJNR: Am J Neuroradiol. 1999; 20:637–642. [PubMed: 10319975]

9. Schrag M, McAuley G, Pomakian J, et al. Correlation of hypointensities in susceptibility-weighted images to tissue histology in dementia patients with cerebral amyloid angiopathy: a postmortem MRI study. Acta Neuropathol. 2010; 119:291–302. [PubMed: 19937043]

10. Jack CR, Knopman DS, Jagust WJ, et al. Tracking pathophysiological processes in Alzheimer's disease: an updated hypothetical model of dynamic biomarkers. Lancet Neurol. 2013; 12:207–216. [PubMed: 23332364]

11. Petersen RC, Aisen PS, Beckett LA, et al. Alzheimer's Disease Neuroimaging Initiative (ADNI): clinical characterization. Neurology. 2010; 74:201–209. [PubMed: 20042704]

12. Mueller SG, Weiner MW, Thal LJ, et al. Ways toward an early diagnosis in

Alzheimer's disease: the Alzheimer's Disease Neuroimaging Initiative (ADNI). Alzheimers Dement. 2005; 1:55–66. [PubMed: 17476317]

13. Rosen WG, Mohs RC, Davis KL. A new rating scale for Alzheimer's Disease. Am J Psychiatry. 1984; 141:1356–1364. [PubMed: 6496779]

14. Shaw LM. PENN Biomarker Core of the Alzheimer's Disease Neuroimaging Initiative. Neurosignals. 2008; 16:19–23. [PubMed: 18097156]

15. Hansson O, Zetterberg H, Buchhave P, Londos E, Blennow K, Minthon L. Association between CSF biomarkers and incipient Alzheimer's disease in patients with mild cognitive impairment: a follow-up study. Lancet Neurol. 2006; 5:228–234. [PubMed: 16488378]

16. Mitchell A, Brindle N. CSF phosphorylated tau: does it constitute an accurate biological test for Alzheimer's disease? Int J Geriatr Psychiatry. 2003; 18:407–411. [PubMed: 12766916]

17. Shaw LM, Vanderstichele H, Knapik-Czajka M, et al. Cerebrospinal fluid biomarker signature in Alzheimer's disease neuroimaging initiative subjects. Ann Neurol. 2009; 65:403–413. [PubMed: 19296504]

18. Yates PA, Sirisriro R, Villemagne VL, et al. Cerebral microhemorrhage and brain beta-amyloid in aging and Alzheimer disease. Neurology. 2011; 77:48–54. [PubMed: 21700585]

19. Kester MI, Goos JD, Teunissen CE, et al. Associations between cerebral small-vessel disease and Alzheimer disease pathology as measured by cerebrospinal fluid biomarkers. JAMA Neurol. 2014; 71:855–862. [PubMed: 24818585]

20. Kalaria RN, Ballard C. Overlap between pathology of Alzheimer disease and vascular

dementia. Alzheimer Dis Assoc Disord. 1999; 13:S115–123. [PubMed: 10609690]

21. Vernooij MW, van der Lugt A, Ikram MA. Prevalence and risk factors of cerebral microbleeds: the Rotterdam Scan Study. Neurology. 2008; 70:1208–1214. [PubMed: 18378884]

22. Williams S, Chalmers K, Wilcock GK, et al. Relationship of neurofibrillary pathology to cerebral amyloid angiopathy in Alzheimer's disease. Neuropathol Appl Neurobiol. 2005; 31:414–421. [PubMed: 16008825]

23. Rosidi NL, Zhou J, Pattanaik S, et al. Cortical microhemorrhages cause local inflammation but do not trigger widespread dendrite degeneration. PLoS ONE. 2011; 6:e26612. [PubMed: 22028924]

24. Takashima Y, Mori T, Hashimoto M, et al. Clinical correlating factors and cognitive function in community-dwelling healthy subjects with cerebral microbleeds. J Stroke Cerebrovasc. 2011; 20:105–110.

25. Kirsch W, McAuley G, Holshouser B, et al. Serial susceptibility weighted MRI measures brain iron and microbleeds in dementia. J Alzheimers Dis. 2009; 17:599–609. [PubMed: 19433895]

26. Poels MM, Ikram MA, van der Lugt A, et al. Cerebral microbleeds are associated with worse cognitive function: the Rotterdam Scan Study. Neurology. 2012; 78:326–333. [PubMed: 22262748]

27. Qiu C, Cotch MF, Sigurdsson S, et al. Cerebral microbleeds, retinopathy, and dementia: the AGES-Reykjavik Study. Neurology. 2010; 75:2221–2228. [PubMed: 21172845]

28. Werring DJ, Frazer DW, Coward LJ, et al. Cognitive dysfunction in patients with

cerebral microbleeds on T2*-weighted gradient-echo MRI. Brain. 2004; 127:2265–2275. [PubMed: 15282216]

29. Patel B, Lawrence AJ, Chung AW, et al. Cerebral microbleeds and cognition in patients with symptomatic small vessel disease. Stroke. 2013; 44:356–361. [PubMed: 23321452]

30. Gregoire SM, Scheffler G, Jager HR, et al. Strictly lobar microbleeds are associated with executive impairment in patients with ischemic stroke or transient ischemic attack. Stroke. 2013; 44:1267– 1272. [PubMed: 23482601]

31. Tang WK, Chen Y-K, Lu J-Y, et al. Absence of cerebral microbleeds predicts reversion of vascular ”cognitive impairment no dementia” in stroke. Int J Stroke. 2011; 6:498–505. [PubMed: 22111793]

32. Pettersen JA, Sathiyamoorthy G, Gao FQ, Szilagyi G, Nadkarni NK, St George-Hyslop P, Rogaeva E, Black SE. Microbleed topography, leukoaraiosis, and cognition in probable Alzheimer disease from the Sunnybrook dementia study. Arch Neurol. 2008; 65:790–795. [PubMed: 18541799]

33. Nakata Y, Shiga K, Yoshikawa K, et al. Subclinical brain hemorrhages in Alzheimer’s disease: evaluation by magnetic resonance T2*-weighted images. Ann N Y Acad Sci. 2002; 977:169–172. [PubMed: 12480748]

34. van der Vlies AE, Goos JD, Barkhof F, Scheltens P, van der Flier WM. Microbleeds do not affect rate of cognitive decline in Alzheimer disease. Neurology. 2012; 79:763–769. [PubMed: 22875093]

35. Haller S, Bartsch A, Nguyen D, et al. Cerebral microhemorrhage and iron deposition in mild cognitive impairment: susceptibility-weighted MR imaging assessment.

Radiology. 2010; 257:764–773. [PubMed: 20923870]

36. Ayaz M, Boikov AS, Haacke EM, et al. Imaging cerebral microbleeds using susceptibility weighted imaging: one step toward detecting vascular dementia. J Magn Reson Imaging. 2010; 31:142–148. [PubMed: 20027582]

37. Miwa K, Tanaka M, Okazaki S, et al. Multiple or mixed cerebral microbleeds and dementia in patients with vascular risk factors. Neurology. 2014; 83:646–653. [PubMed: 25015364]

38. Arvanitakis Z, Leurgans SE, Wang Z, et al. Cerebral amyloid angiopathy pathology and cognitive domains in older persons. Ann Neurol. 2011; 69:320–327. [PubMed: 21387377]

39. Petersen RC, Aisen PS, Beckett LA, et al. Alzheimer's Disease Neuroimaging Initiative (ADNI): clinical characterization. Neurology. 2010; 74:201–209. [PubMed: 20042704]

40. Rosen WG, Terry RD, Fuld PA, et al. Pathological verification of ischemic score in differentiation of dementias. Ann Neurol. 1980; 7:486–488. [PubMed: 7396427]

CHAPTER 6

USE OF TETHERED ENZYMES AS A PLATFORM TECHNOLOGY FOR RAPID ANALYTE DETECTION

This chapter presents the design and construction of a new diagnostic platform (biosensor), based on enzymes tethered to nanoparticles, that is able to detect, in a rapid and sensitive manner, the presence of stroke biomarkers such as neuron-specific enolase (NSE) in blood samples. My contributions to this study was in leading the *in vivo* experiments of this project, which include: surgical and stroke model preparation (Fig 7.3A-F), blood sample collection for enolase detection (fig 7.3C-F), histological analysis of stroke volumes (Fig 7.3 A and B), and contributing to the intellectual guidance of the study, while Roy Cohen and James Lata, researchers at Travis's lab, completed the design and construction of the biosensor, the experimental data taking and analysis. While I am not the first author on this work and thus consider it a secondary contribution, I include the full manuscript for clarity and completeness.

This work is published in *PLoS ONE*. The citation is:

Cohen R., et al. (2015) Use of Tethered Enzymes as a Platform Technology for Rapid Analyte Detection. PLoS ONE 10(11): e0142326.

6.1 ABSTRACT

Background: Rapid diagnosis for time-sensitive illnesses such as stroke, cardiac arrest, and septic shock is essential for successful treatment. Much attention has therefore focused on new strategies for rapid and objective diagnosis, such as Point-of-Care Tests (PoCT) for blood biomarkers. Here we use a biomimicry-based approach to demonstrate a new diagnostic platform, based on enzymes tethered to nanoparticles (NPs). As proof of principle, we use oriented immobilization of pyruvate kinase (PK) and luciferase (Luc) on silica NPs to achieve rapid and sensitive detection of neuron-specific enolase (NSE), a clinically relevant biomarker for multiple diseases ranging from acute brain injuries to lung cancer. We hypothesize that an approach capitalizing on the speed and catalytic nature of enzymatic reactions would enable fast and sensitive biomarker detection, suitable for PoCT devices.

Methods and findings: We performed in-vitro, animal model, and human subject studies. First, the efficiency of coupled enzyme activities when tethered to NPs versus when in solution was tested, demonstrating a highly sensitive and rapid detection of physiological and pathological concentrations of NSE. Next, in rat stroke models the enzyme-based assay was able in minutes to show a statistically significant increase in NSE levels in samples taken 1 hour before and 0, 1, 3 and 6 hours after occlusion of the distal middle cerebral artery. Finally, using the tethered enzyme assay for detection of NSE in samples from 20 geriatric human patients, we show that our data match well ($r = 0.815$) with the current gold standard for biomarker detection, ELISA—with a major difference being that we achieve detection in 10 minutes as opposed to the several hours required for traditional ELISA.

Conclusions: Oriented enzyme immobilization conferred more efficient coupled activity, and thus higher assay sensitivity, than non-tethered enzymes. Together, our findings provide proof of concept for using oriented immobilization of active enzymes on NPs as the basis for a highly rapid and sensitive biomarker detection platform. This addresses a key challenge in developing a PoCT platform for time sensitive and difficult to diagnose pathologies.

6.2 INTRODUCTION

There is pressing need for quick and objective diagnostic technologies for both time sensitive and difficult to diagnose pathologies. Much attention has therefore focused on the identification of disease-specific peripheral biomarkers, and use of new technologies to improve anti- body-based detection capabilities. This interest is well justified because of the enormous medical, social and economic impacts of these diseases, in both developed and developing countries. This manuscript presents data about an alternative technological approach to bio- marker detection—the use of enzymes tethered to NPs. For proof of principle, we'll focus on a single biomarker, NSE, that has been suggested to have value for diagnosing various pathologies (particularly those involving the central nervous system). No single biomarker is known to be sensitive and specific enough to diagnose a complex neural disease state. Rather, we present these data as proof of principle for the underlying diagnostic platform suitable for rapid detection of biomarker analytes.

Stroke is one of the best examples of a brain disease that is both hard to diagnose and

time sensitive, annually affecting over 15 million people. Of these, 5 million die and an additional 5 million are left permanently disabled [1]. Currently, its diagnosis relies on neurologists to distinguish stroke from mimics using advanced imaging tests (e.g. CT, MRI) in order to determine whether the stroke is ischemic or hemorrhagic. If appropriate, thrombolytic treatment can then be initiated, but is most effective only within a short 3–4 hour window from onset [2]. Remarkably, due to the time constraints for initiating effective treatment lack of prompt diagnosis for ischemic stroke results in less than 4% of patients in the US receiving thrombolytic therapy [3]. In addition to rapid diagnosis of stroke, there is growing military and civilian need for PoCT devices that provide objective, biomarker-based, diagnostic and prognostic information regarding traumatic brain injuries (TBI/concussion), and neurodegenerative disease [e.g. Alzheimer's disease (AD), Parkinson's Disease (PD)]. For these brain injuries, an objective PoCT could lead to interventions beginning early upon the onset of disease as well as provide a platform to monitor disease progression or response to therapy. From a global perspective, the increasing incidence of stroke in developing countries [4], the high cost and limited availability of health resources associated with stroke diagnosis, significantly reduces favorable outcomes [5].

Traditional technologies for blood biomarker diagnostics include ELISA, PCR, and mass spectrometry (MS). However, these technologies are limited to laboratory use because they require sample preparation, and use of sophisticated instruments and highly trained technicians. Moreover, they are time and labor intensive, and are expensive [6]. Much of the research on detection of blood biomarkers has focused on antibody-based methods.

Although there has been considerable progress in the field, such as the introduction of lateral flow based assays, constraints due to the speed of antibody-antigen interactions, low sensitivity, semi-quantitative results and the complexity of associated detection instrumentation have thus far prevented such antibody capture methods from becoming the basis for a field-capable PoCT device to detect brain injuries [6].

Over the last few decades, a large number of molecules have been studied for their potential usefulness as blood-borne biomarkers. Although no single biomarker will likely provide a definitive diagnosis of any disease, the glycolytic enzyme, NSE, is released from damaged neurons and has been suggested to be valuable for the diagnosis of various brain injuries [7-9]. Evidence also supports its usefulness as a prognostic indicator in predicting neurological outcomes of post-cardiac arrest [10] and mild TBI [11]. NSE has been suggested to be useful in distinguishing stroke from mimics, an important first step in expediting the diagnostic process [7]. In addition, it has been suggested that changes in serum NSE levels may indicate changes in brain morphology in AD [12]. Overall, changes in plasma NSE levels are of clinical significance to several of the major brain injuries, making it an excellent first candidate to test a new diagnostic platform technology.

As an alternative to antibody capture, fluid phase enzymatic reactions have been used to detect plasma NSE by means of its enzymatic activity [13, 14]; however, in the 30 years since these assays were first described, to our knowledge, no related PoCT technologies have been reported. Semi-solid phase bioluminescence detection of NSE through its

binding to immuno-beads enabled high sensitivity detection [15]. However, this method required long serum-bead incubation times and did not tether the downstream enzymes (i.e. PK and Luc). Tethering enzymes has several advantages for a PoCT, such as concentrating the detection reaction, spatially localizing the readout, and potentially improving shelf life. The principle obstacle lies in maintaining enzymatic function when immobilizing enzymes. Immobilization often interferes with substrate binding sites and/or needed conformational changes [16].

To overcome this obstacle, we adopted a strategy of biomimicry, inspired by the tethering of glycolytic enzymes to a cytoskeletal scaffold in the sperm flagellum, where they provide localized energy production [17,18]. We previously showed that oriented immobilization via genetically-encoded binding domains conferred advantages in specific activity versus either random adsorption or chemically-specific binding [19,20]. Here, we extend our previous studies [19,20] in a novel direction to generate a PoCT platform based on enzymes tethered to nanoparticles via biomimetic oriented immobilization (Tethered Enzyme Technology, TET). Our approach couples production of ATP by PK with activity of firefly luciferase (Luc) to generate a highly rapid and sensitive bioluminescent readout for the detection of NSE. As a tethering scaffold for the PoCT device, we employed SiO_2 nanoparticles for their many positive attributes: high biocompatibility, low optical absorption, dispersibility, high surface area, and the ability to be integrated into various devices with spatial control. We hypothesized that oriented immobilization of PK and Luc on SiO_2 NPs could provide the basis for highly rapid, quantitative and sensitive detection of NSE through an enzymatic cascade reaction in a

form suitable for use in a PoCT.

6.3 RESULTS

6.3.1 Improving couple reaction activity by immobilization of PK and Luc on NPs

We have previously shown that oriented immobilization of the glycolytic enzymes, TPI and GAPDH, enhances both their individual activities as well as the activity of their coupled sequential reactions in comparison to enzymes tethered via chemically-specific but non-oriented carboxyl-amine binding [20]. To test whether this would hold true for the coupled sequential reactions of PK and the non-glycolytic enzyme Luc, we generated mammalian PK and Luc expression plasmids, each as a fusion protein with two affinity tags, as described in the Materials and Methods section. Each of the constructs included an amino-terminal silica-binding peptide sequence (Si-tag) [21,22] for immobilization of proteins onto SiO_2 nanoparticles (Si-NPs) and a 6xHis-tag to be used for protein purification (Fig 6.1A, see also 6. S1).

To test our hypothesis that oriented immobilization would impart an improvement on the specific activity of the coupled reaction (Fig 6.1B), we measured the coupled activities of various combinations of tethered and free PK and Luc (Fig 6.1C and 6.S2). Analysis of all four possible combinations revealed a significant increase in the readout signal when Luc was immobilized (green triangles, 3.01±0.2 fold, $p<0.001$) and an even larger increase upon immobilization of both Luc and PK (black circles, 4.25±0.12 fold, $p<0.001$). When Luc was in solution (not tethered), the coupled activity of the PK-Luc reaction was reduced, regardless of whether PK was in solution or tethered, suggesting

that having Luc in close proximity with the source of ATP production (PK) was crucial for increased coupled reaction efficiency.

To investigate further the source of the improvement in Luc activity when tethered, we com- pared Luc in-solution versus immobilized. In agreement with previous findings [23], our measurements revealed a 10-fold average reduction in the sensitivity to ATP of immobilized Luc (data not shown). However, Luc tethered on the Si-NPs exhibited extended photon emission dynamics, with a slower decay rate when compared to the soluble protein (Fig. 6.S2B). The differences in the enzymatic activity of immobilized Luc might result from a change in diffusion resistance and/or a slowing of kinetics due to conformational constraints. In terms of the PK-Luc coupled reaction, the reduction in Luc sensitivity was most likely compensated for by the prolonged emission kinetics. For example, placing Luc in closer proximity to PK (such as occurs with particle packing) would enhance the efficiency of ATP channeling by reducing the diffusion distance and effective local reaction volume, thereby increasing the effective local concentration of ATP, and enhancing luminescence output. Additional investigations of the impacts of enzyme tethering/proximity can be found as supplemental material (Figs 6.S2 and 6.S4).

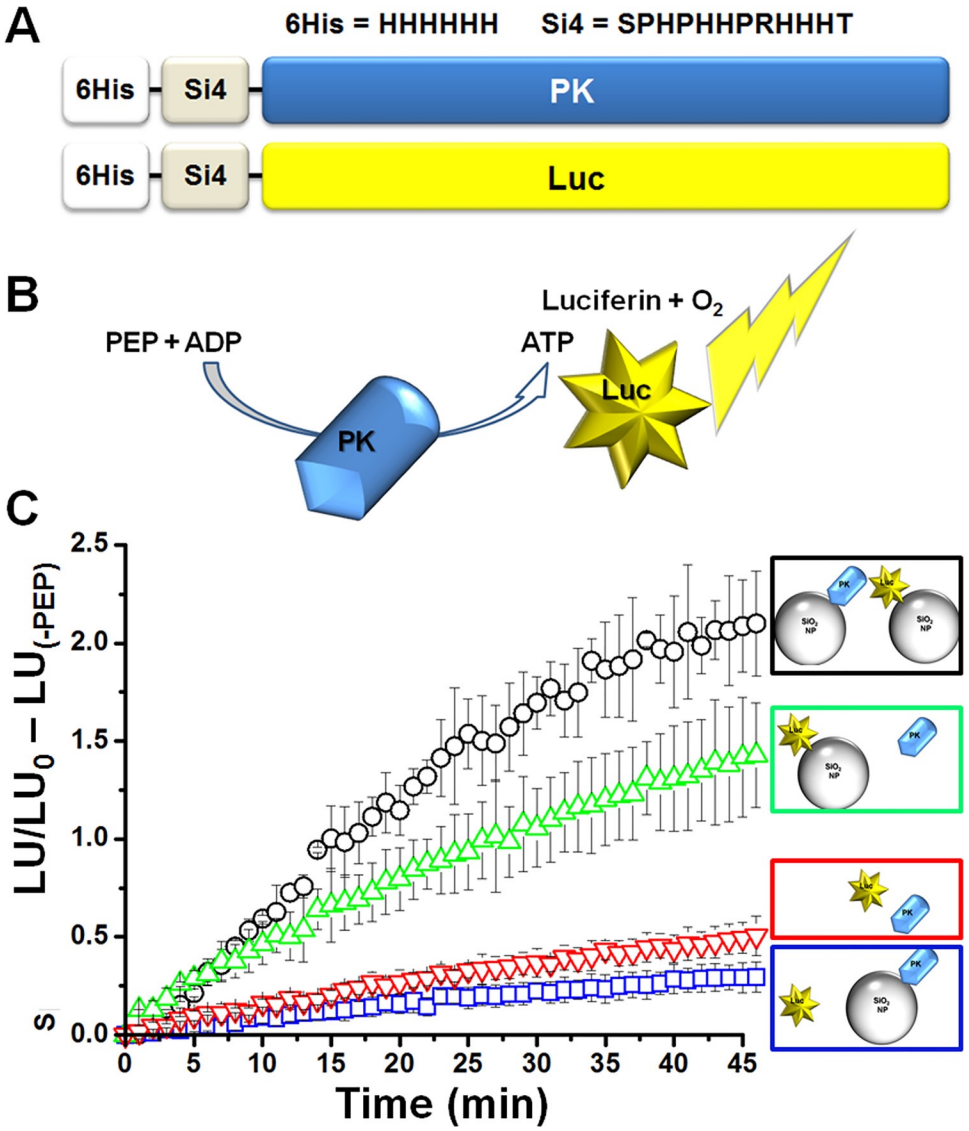

Fig 6.1. Immobilization of PK and Luc on NPs improves coupled reaction efficiency. A) Schematic illustration of the 6XHis-Si tag fusion constructs for PK or Luc. B) Schematic representation of the PK-Luc coupled reaction as used in the experiments described in C. C) PK and Luc coupled activity was assayed in 4 combinations as indicated by the color coded schematic illustrations: black- (NP-PK) + (NP-Luc), blue- (NP-PK) + (soluble Luc), green- (NP-Luc) + (soluble PK) or red- (soluble PK + soluble Luc). All combinations included equivalent amounts of PK and Luc. Maximal coupled

reaction efficiency, as calculated from normalizing each time point data to t_0 (indicating the ratio of luminescence generated at each time point relative to the luminescence at the beginning of the reaction) and subtraction of the negative control well (no PEP, corresponding to the background luminescence signal), was observed when both PK and Luc were immobilized on NPs (each condition was tested in triplicates; data shown represents 3 individual experiments; AVG±STDEV).

6.3.2 Improving sensitivity of enolase detection

We next hypothesized that the increased efficiency of the immobilized coupled reactions might provide a sensitive and rapid luminescence based assay for detection of the biomarker NSE, through a 3-step coupled reaction as follows–enolase/NSE catalyzes the conversion of 2-phosphoglycerate (2-PG) to phosphoenolpyruvate (PEP), PK in turn converts PEP and ADP to pyruvate and ATP, with the latter being used by Luc to generate a photon of light. We first tested this hypothesis using the non-neuronal isoform α-enolase (ENO). The sensitivity of the tethered enzymes (red, PK and Luc tethered separately to NPs) was significantly higher than that of freely diffusing enzymes (blue) when detecting ENO activity (Fig 6.2A). In particular, higher sensitivity of the PK-Luc coupled reaction was observed at lower ENO concentrations (Fig 6.2A inset).

Next, we sought to determine whether the NP-PK and NP-Luc coupled reaction could detect physiologically relevant concentrations of human NSE (< 8.7 ± 3.9 ng/ml [24]). Fig 6.2B shows a representative dose response experiment where sub-physiological amounts of commercial human NSE were added to the reaction mixture in the presence

of NP-PK and NP-Luc (tethered separately). The luminescent signal generated by Luc was integrated over 10 minutes, showing statistically significant differences for each concentration of NSE. These results indicate that using immobilized PK-Luc coupled reactions provides sub-physiological sensitivity for NSE, at concentrations well below typical pathological plasma levels, with rapid detection times.

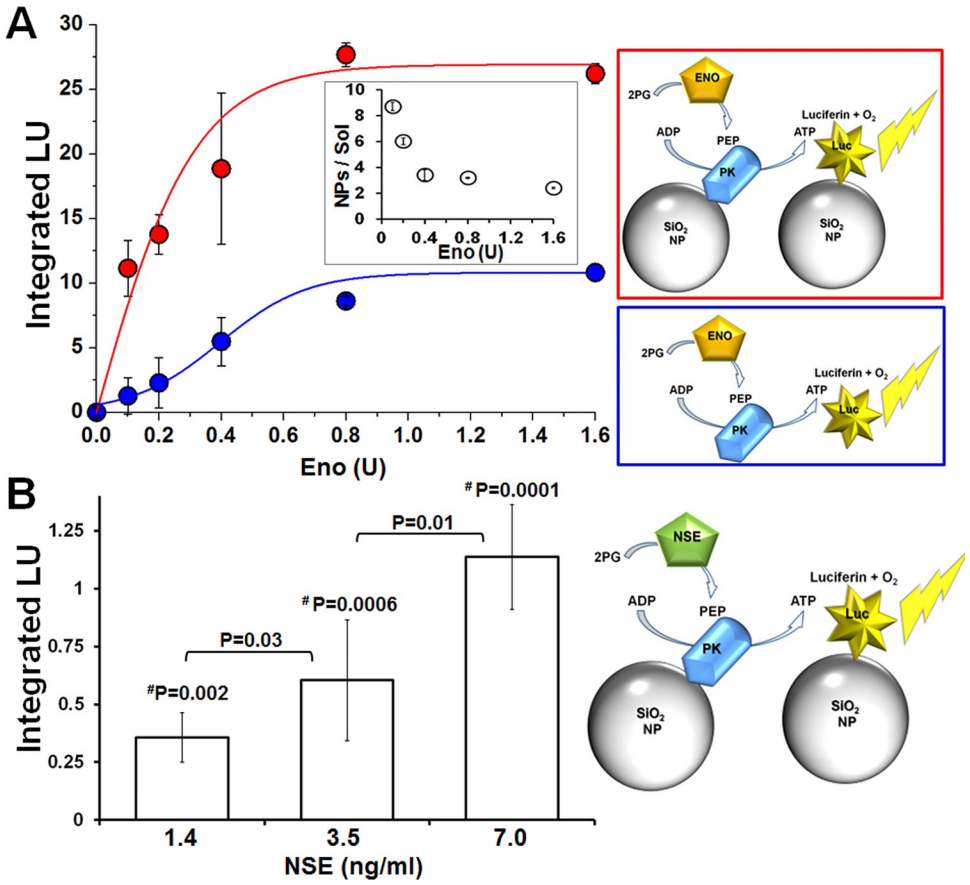

Fig 6.2. Improved sensitivity for enolase detection via its enzymatic activity when using tethered PK and Luc. A) Comparison of the detection sensitivity for enolase activity (Eno) as measured by NP-PK + NP-Luc (red) vs. PK + Luc in solution (blue). Increasing concentrations of Eno were added to immobilized or freely diffusing enzymes

in reaction buffer. Luminescence was detected and integrated over 10 minutes at RT and plotted against Eno final unit amount (lines were added to guide the eye). The inset shows the ratio of the enzymes' activities on NPs versus in solution as a function of units of ENO. Data presented as AVG±STDEV. B) NSE detection via PK and Luc coupled activity was performed as indicated in the schematic illustration (right). His-Si-PK and His-Si-Luc were immobilized on 500 nm NPs and mixed with reaction buffer supplemented with increasing concentrations of human NSE. Luminescence readout was normalized to t0 (first read) values and plotted as a function of time. Then, the luminescent signal was integrated for first 10 minutes, and a reading from the zero NSE well was subtracted from the collected signal. The sensitivity of the tethered enzyme assay was about 5 times higher than the reported average physiological NSE blood concentration (8.7 ± 3.9 ng/ml [24]). P values were calculated using student's t-test for comparisons between NSE concentrations; values marked with $^{\#}$P were calculated for significance when compared against 0 ng/ml NSE.

6.3.3 Detection of neurons-specific enolase on *in vivo* stroke model

The improved sensitivity and kinetics of NSE detection with the tethered coupled enzymatic reactions encouraged us to test our biomarker detection assays in the complex environment of blood plasma. For these experiments, we used a rat model for stroke, in the form of a focal stroke that was induced by clotting the distal branches of the middle cerebral artery (MCA).

Peripheral blood samples from experimental stroke and sham-operated control rats were

taken 1 hour before and 0, 1, 3 and 6 hours after occlusion of distal MCA branches. Luminescence output was integrated over 10 minutes from the NSE-PK-Luc coupled reaction (PK and Luc tethered separately to NPs), but with the active NSE originating from the damaged/dying neurons. Stroke-induced cell death in the rats was confirmed with Fluoro-Jade C staining (see details in Materials and Methods section). The volume of brain with damaged neurons was on average 11.25±4 mm^3 (n = 4, 3A) in the stroke animals, and 0.002±0.001 mm^3 in the sham- operated controls (3B n = 4). Integrated luminescence values at each time point were calculated by subtracting a negative control reaction (lacking the NSE substrate, 2-PG) from the test reaction (that included 2-PG). Fig 6.3E summarizes the data collected from 10 rats (5 stroke and 5 control), showing a statistically significant increase in NSE levels as soon as 1 hour post-occlusion, whereas control rats showed no increase in plasma NSE levels (detailed time point data for each rat are provided in panels 3C and 3D).

Next, we compared results from our tethered enzyme technology (TET) versus quantification of the rat NSE as obtained from a commercial ELISA kit, which is currently the standard detection technology. Consistent with the results from the coupled enzymatic assay at that same time point, the ELISA revealed a 2-fold increase in NSE concentration at 6 hours post stroke (Fig 6.3F). No elevation was found in non-neuronal isoforms of enolase (NNE) as measured using a NNE ELISA kit (data not shown), demonstrating that the source of enolase activity that we measured was indeed NSE. Importantly, while the measurements of NSE concentration using the “gold standard” ELISA assays took over 3 hours, the TET based assay provided results within 10

minutes.

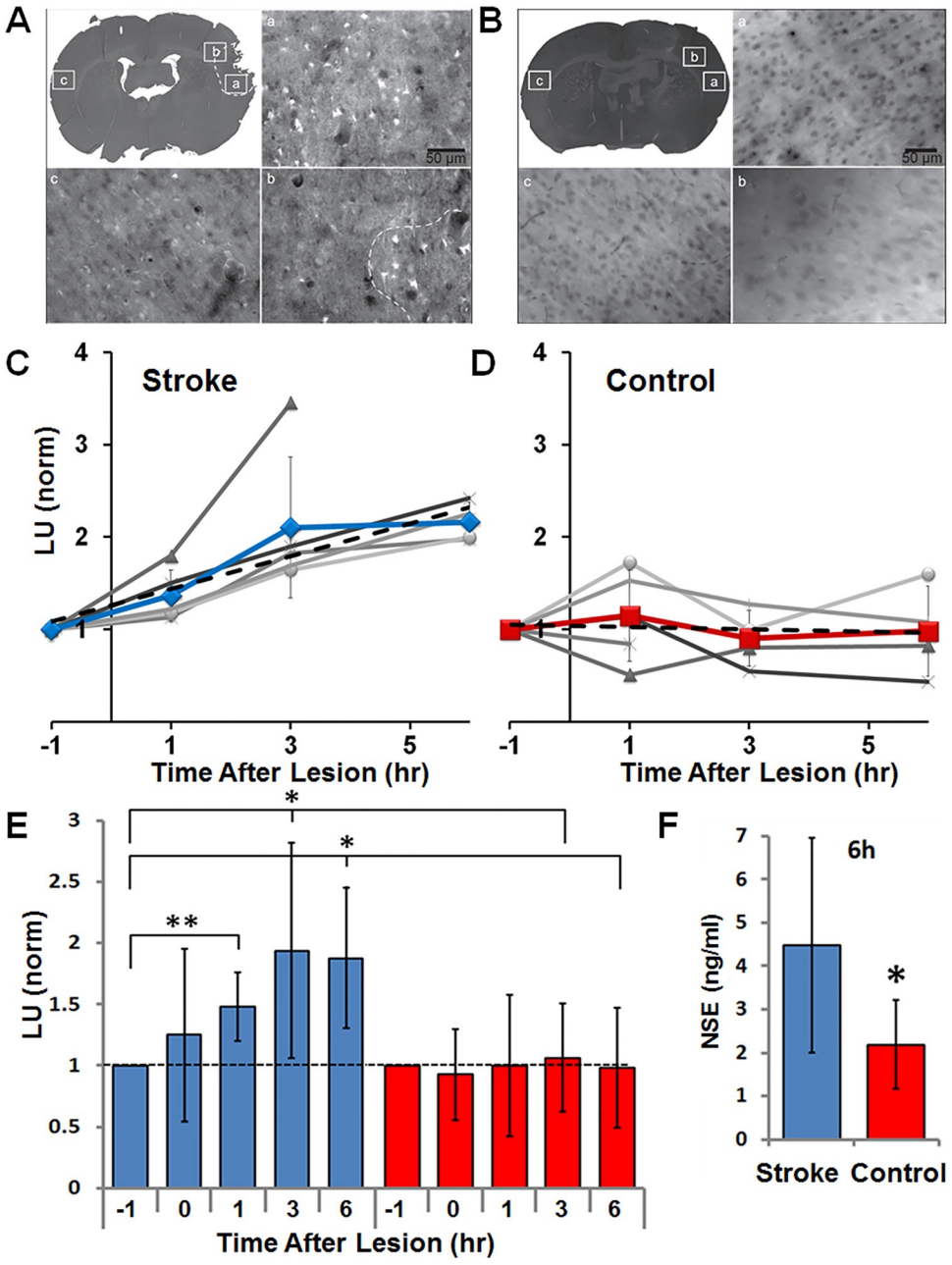

Fig 6.3. Using NP-PK and NP-Luc for rapid detection of NSE in a rat model for stroke. A) Fluoro Jade-C staining for measurement of damaged brain tissue volume. The presence and absence of FJC-labeled degenerative neurons were imaged with

epifluorescence under 20x magnification using filters for FITC. (a) Region with abundant FJC staining (bright cells) on lesioned side. (b) Region at the edge of FJC staining. (c) Region that is contralateral to (a) that did not show any FJC staining. Dotted line in B and low magnification inset indicates manually-mapped border between FJC positive and negative areas. B) FJC staining in control brain section. (a) and (b) are in area of craniotomy. C-D) Individual rat data (C-stroke and D-control) for NSE measurements at each time point (grayscale lines indicate data points for individual animals, line with symbol indicates the mean±standard deviation) as performed by tethered PK and Luc assay, and normalized to time point -1 hour. Plasma samples were collected from stroke induced or control rats pre (-1 hr), and post occlusion (0, 1, 3 and 6 hr). The mean slope of the trend (dashed line) was calculated averaging individual slopes in each group (stroke = 0.26 with 0.95 confidence interval, control = -0.02 with 0.38 confidence interval). E) Summary of rat stroke model experiments showing a statistically significant increase in NSE plasma levels in stroke (blue bars) vs. control (red bars) rats as soon as 1 hour post occlusion. F) Measurements of NSE in plasma from rats using ELISA showed elevated levels in stroke compared to control rats at the last time point (6 hr post-occlusion). P values– $0.05<*<0.1$, $0.01<**<0.05$. Data from 10 rats were included in our analysis, with the exclusion of 3 hour and 6 hour time points for one control animal that died (at 2 hour mark), and a 6 hour time point for a stroke animal which died and was found to have a large hemorrhage at the base of the brain.

6.3.4 Rapid detection of neurons-specific enolase on human samples

Moving forward from an animal model, we next tested TET's ability to detect NSE in the

even less defined environment of human plasma. Blood samples were collected from consenting patients seen at the Central New York Alzheimer's Disease Assistance Center (ADAC) at SUNY Upstate Medical University using Na-Heparin tubes. Plasma was then divided with a portion of the sample tested immediately using TET and the rest frozen at -80°C for later confirmation via commercial ELISA. We ran this experiment using TET in the form of a first generation PoCT technology for human NSE testing. Namely, reactions were designed to work with minimal plasma volume in white 96 well plates in which all test and control reaction components had been lyophilized. 10 µl of freshly collected plasma was added into pre-loaded wells and the light output was measured with a conventional plate reader. TET reaction reading was completed within 10 minutes from the addition of plasma to the pre-loaded wells, where each test included triplicate negative control wells (reaction lacking 2PG), positive control wells (pre-loaded with enolase) and test wells, so that a total of 90 µl of plasma was used for each subject tested (a volume able to be obtained from less than 4 drops of blood). Importantly, using a positive control reaction including known amounts of spiked Eno, allowed us to normalize the data between experiments and minimize any variabilities that might arise from batch to batch differences in enzyme activity. To validate the accuracy of the TET results (representative data shown in Fig 6.4A), plasma samples were sent for lab testing (ARUP labs, Salt Lake City, UT). Using a Pearson's correlation test, we compared TET and ELISA data finding a significant correlation of 0.81 between the two approaches (Fig 6.4B).

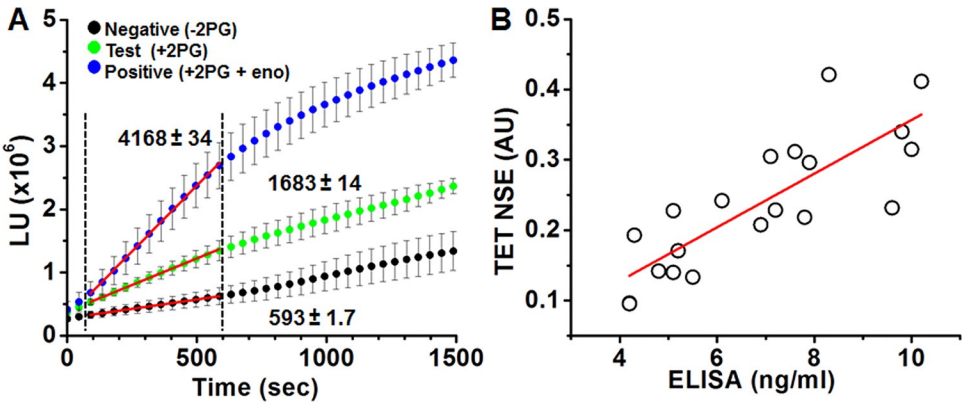

Fig 6.4. Using the tethered enzyme assay for rapid detection of NSE in human subjects. A) Representative data as measured from a total of nine wells per subject (triplicate measurements of negative control with no 2PG; the test sample with 2PG; and positive control wells with 2PG and enolase (Eno); mean ±STDEV) For calculation of NSE levels, slopes of averaged curves were calculated for the first 0.5–10 minutes of the enzymatic reactions (indicated by the red linear fit in between the dashed lines), then test wells were normalized to positive and negative wells (see methods section). B) High correlation was found between NSE measurements by ELISA (ng/ml) vs. TET assay (AU represents the normalization of test reaction to the negative and positive reactions, as illustrated in A and described in the methods section) as of the human plasma samples. Line indicates best fit. Pearson's r = 0.815, n = 20.

6.4 DISCUSSION

Our results suggest that enzymes tethered via oriented immobilization can provide a PoCT platform enabling simple, rapid and objective testing for biomarkers associated with hard to diagnose and time sensitive diseases. We focused on NSE for this proof of

concept because it has been shown to convey clinically relevant information for several brain injuries and cancers.

Immobilized enzymes present several important advantages for medical applications including stability and spatial organization in a device, whether with a microfluidic card or paper chromatography. Of note, our data show that oriented enzyme immobilization also significantly improved the efficiency with which coupled enzymatic reactions occurred. This is of special importance because use of coupled enzymatic reactions allows signal amplification at both the stages of biomarker detection and transduction of signal into the luminescent readout. When combined with the inherently enhanced sensitivity and speed of catalytic activity, tethered enzymes provide some of the highly desired features expected from a PoCT diagnostic platform. Demonstrating their suitability for this purpose, we showed in vitro the advantages of using tethered versus soluble enzymes. We showed that TET-based systems could detect physiologically and pathologically relevant concentrations. Importantly, the immobilized enzyme-based detection system provided an ultra-rapid analysis (i.e. within 10 minutes) even when using plasma samples obtained from rat stroke models or human patients.

The high correlation between ELISA and TET suggests circulating NSE enzymatic activity corresponds very well with the amount of protein. This comparison between TET and ELISA in detection of NSE raises another important finding regarding the dynamic range for detection provided by these two methods. Whereas the ELISA method provides a linear detection range, the enzyme-based assay offers close to a 2-fold larger dynamic

range (as defined by the difference between the smallest and largest usable signal, and calculated from the max to min values for each assay). Along with the increased assay speed (minutes for TET vs. hours for ELISA), minimal user effort (TET is a "mix and test" assay, while ELISA requires multiple wash steps), this finding revealing the increased sensitivity of TET versus antibody capture techniques pro- vides another feature contributing to the improvements of TET over ELISA.

One potential criticism of use of tethered enzymes is that the range of biomarkers able to be detected through enzymatic reactions represents a limited subset of target analytes. However, there are numerous biomarkers with bona fide enzymatic activity (e.g. nucleoside diphosphate kinase A; NDKA [25], and phosphoglycerate mutase; PGM [26]), or are modulators of enzyme activity (e.g. calcium [27], magnesium [28]), or are substrates and metabolites of enzymatic reactions (e.g. glutamate and glucose [29]). Currently, no single biomarker, including NSE, can accurately and definitively diagnose any disease. Therefore, we are designing and testing TET- based approaches for multiple classes of target analytes, beyond enzymes. This will allow us to simultaneously quantify suites of biomarkers, significantly increasing the accuracy and robust- ness of the diagnostic test.

Together, our data support further investigations of enzymes tethered to NPs via oriented immobilization in PoCT diagnostics. The advantages of spatial control of enzyme activities, and rapid and sensitive detection with signal amplification at both detection and transduction into luminescence output, combine to make TET a highly attractive

alternative to antibody- based detection. These attributes are especially attractive for integrating TET into a PoCT technology for use by paramedics, athletic trainers and in the field. In terms of lack of need for excitation, low power requirements, and potential telemedicine capability, this technology is potentially game-changing for health care management in rural areas and developing countries.

6.5 METHODS

6.5.1 Ethics Statement

All research involving human participants (including consent forms and procedure) was approved by Cornell (#1410005002) and SUNY Upstate (#623458–5) IRBs. Written and verbal consent were obtained from participating subjects or health care surrogates and documented according to best practices. Samples were given de-identifying codes to ensure participant confidentiality. All animal procedures were reviewed and approved by the Cornell University Institutional Care and Use Committee (#2009–0043) and were conducted in strict accordance with the recommendations in the Guide for the Care and Use of Laboratory Animals (published by NIH).

6.5.2 Experimental Design

The aim of this study was to explore the advantages of utilizing enzymes tethered via oriented immobilization in the detection of NSE, a neuronal injury biomarker, towards development of a PoCT technology for time sensitive illnesses.

The study was designed to follow 3 successive stages: (i) Test the enzyme-based assay in vitro to examine the effects of oriented enzyme immobilization on the sensitivity and

efficiency of the solid phase vs fluid phase reaction. (ii) Test the tethered enzyme assay in plasma from a rat stroke model. Here, to simulate stroke, 2 groups of rats underwent craniotomy under anesthesia, and branches of the MCA were cauterized in the test group. Peripheral blood samples were drawn over a time period of 6 hours to monitor changes in NSE level. Finally, the changes in NSE levels as measured with TET were compared to those obtained with ELISA. (iii) Use pre-filled 96 well plates in a comparative analysis of NSE plasma levels in samples taken from human subjects and measured by both the solid phase TET reaction and ELISA.

6.5.3 Reagents

Enliten ATP detection kit was purchased from Promega (Madison, WI). 2-PG, PEP, ADP, ATP, luciferin, PK antibody, NSE, and yeast α-enolase were from Sigma (St. Louis, MO). pcDNA4/HisMax TOPO TA vector was from Invitrogen (Carlsbad, CA). Si-NPs (500 nm) were purchased from Spherotech Inc. (Lake Forest, IL).

6.5.4 Construction of His-Si4 fusion proteins

The complementary deoxyribonucleic acid (cDNA) of PK was obtained by reverse-transcription polymerase chain reaction (RT-PCR) from mouse muscle RNA. The Luc2 sequence was amplified from the Luciferase2 plasmid, Promega (Madison, WI). His-PK and His-Luc were generated by TA cloning of PK and Luc into pcDNA4/HisMax TOPO TA. To generate the His-Si4 vector, two complementary oligonucleotides (Integrated DNA Technologies, Inc. USA) encoding the Si4 sequence [22] with overhanging A were hybridized and cloned into the TA site of the pcDNA4/HisMax TOPO TA plasmid,

followed by restriction/ligation of PCR fragments of PK and Luc to make His-Si4-plasmids. Subsequently, the Si4-PK and Si4-Luc sequences were amplified by PCR and inserted into pcDNA3.1 to make Si4-PK and Si4-Luc. Constructs were validated by sequencing and amplified in TOP10 cells and then purified.

6.5.5 Protein expression and purification

HEK293-F-FreeStyle cells (Invitrogen, Grand Island, NY) were transfected with plasmids encoding His, His-Si4 or Si4 fusion proteins using the Freestyle MAX reagent (Invitrogen, Grand Island, NY) and incubated for 24–72 hrs in 8% CO_2. Cells were harvested and lysed by sonication (Sonifier 250, Branson, Danbury, CT). His-tag or His-Si4 fusion proteins were purified on Ni/NTA beads as previously described [30], with the exception that the Si4 tag was used to immobilize PK on silica NPs directly from the cell lysate (Figs. 6.S1D and 6.S1E), providing a fast and simpler purification process.

6.5.6 Enzymatic activity assays

Enzyme activities for both single and coupled reactions were assessed via luminescence output, in sodium phosphate buffer (50 mM) supplemented with $MgCl_2$ (5 mM) and KCl (20 mM). The forward reaction for PK is: PEP + ADP ! pyruvate + ATP. The forward reaction for Luc is: ATP + luciferin + Mg^{2+} ! hν. The PK and Luc coupled reaction is: PEP + ADP ! pyruvate + ATP + luciferin ! hν. All experiments were carried out in 96-well black or white plates at room temperature. Purified or immobilized PK was mixed with Enliten luciferase/luciferin reagent in addition to ADP and PEP as indicated for

individual experiments. Purified or immobilized Luc was mixed with luciferin, Mg^{2+}, K^{+} and ATP as indicated in individual experiments and activity was monitored by means of light emission as detected by a luminometer (GloMax, Promega, Madison, WI), where the luminescence signal was integrated for 3 seconds every minute for up to 50 minutes, as indicated per each experiment. To assess the activity of the coupled reactions, PK and luciferase were mixed as indicated above, with luciferin, ADP and PEP, and light emission was measured by luminescence. To maximize enzyme activity per NP, protein was added in saturating amounts to the NPs [31]. Data processing and analysis were carried out using Excel (Microsoft) and Origin (Origin Lab, Northampton, MA). In experiments with internal repetitions, data are presented as average ± standard deviation. Otherwise, representative experiments are shown that were repeated independently at least three times with similar results.

6.5.7 Detection of NSE in rat stroke model

Surgery and occlusion. Male Sprague-Dawley rats (Charles River, Wilmington, MA) with average weight 400 g (std. dev. 83 g, range 260–530 g) were used in these experiments. Only males were used, to eliminate potentially confounding effects from the stage of estrus cycle. Animals were anesthetized with 5% isoflurane in oxygen and were maintained on 1.3–2.0% isoflurane. Anesthesia was adjusted to maintain both constant breathing rate of ~1 Hz, measured manually, and suppression of pedal withdrawal reflex. Rats were free breathing. In previous work [32], we have found that with these parameters it is not necessary to artificially ventilate animals for consistent cortical blood

flow. Body temperature was maintained at 37.5°C with a feedback controlled rectal thermometer. Glycopyrrolate (50 mg/100 g rat) was injected intra- muscularly to suppress fluid buildup in the lungs. Rats were placed in a stereotaxic device and incision locations were shaved, cleaned and injected with bupivacaine (0.125%, s.c.) for analgesia. The femoral artery was catheterized with PE 50 tubing for arterial blood draws. The skin and muscle on the right side of the skull were retracted, and a craniotomy was drilled from the temporal bone to just above the zygomatic arch. The dura was reflected. In experimental stroke animals, branches of the MCA were cauterized at both the entry and exit points from the field of view so that there was no flow visible in the exposed branches of the MCA. In sham animals no cauterization was used. The occlusion procedure took approximately 15 minutes, with time 0 recorded at the end of the occlusion procedure. The occlusions were visually checked every 15 minutes to ensure that the clots remained. In a few animals, some vessels became patent within the first hour and were re-cauterized. Experiments were conducted in matched pairs of sham animals and stroke animals. Blood (0.5 ml) was drawn at 1 hour before occlusion (or sham), and after 0, 1, 3 and 6 hours post occlusion. In order to avoid dilution, flushing of the catheter was minimized. Fluids were replenished by subcutaneous injection of 0.5 ml of 5% glucose after every blood collection.

After the last blood draw, animals were overdosed with pentobarbital. Chest cavities were opened before the heartbeat ceased and in some cases blood was drawn from a ventricular cardiac puncture. Animals were intracardially perfused with ~150 ml PBS and 300 mL 4% paraformaldehyde in PBS. Heads were stored in paraformaldehyde. Images were

taken of each brain after extraction and before sectioning.

Fluoro-Jade C Staining. Brains were harvested and cryoprotected in 30% sucrose and then 60% sucrose for at least 24 hour each. Brains were frozen and cut into coronal, 45-μm sections on a cryotome. For Fluoro-Jade C (FJC; Millipore) staining, sections were washed in 80% EtOH in 1% NaOH for five minutes, 70% EtOH for 2 minutes, and 0.06% $KMnO_4$ for 10 minutes. Sections were then incubated in the solution of 0.00015% of FJC solution (1:100 stock, according to manufacturer's instructions, dissolved in 0.1% of acetic acid) for 20 minutes. Sections were then washed with distilled water 3 times, for 1 minute each, at which time the slides were dried for 5 minutes and put into xylene solution for 5 minutes. Last, slides were dried for an hour and coverslipped with Permount (Electron Microscopy Sciences). Initially, FJC staining was performed at 1 mm spacing throughout the brain. After the most anterior and posterior sections with FJC staining were identified, additional sections were stained to resolve the stroke volume with 200–300 μm spacing.

Measurement of rat brain infarct volume and torn tissue area. Low magnification white light images of the entire section were photographed under a stereoscope. FJC staining was imaged with epifluorescence under 20x magnification using filters for FITC. The area labeled with FJC was manually identified by a person blinded to the treatment and marked on the low magnification, white light images of whole brain sections using ImageJ. For figures, images were normalized by calculating the mean and standard deviation of manually selected back- ground region and then setting the minimum

intensity to 4.2 x standard deviation below the mean, and maximum intensity to 7.2 x standard deviation above the mean. Total FJC volume was obtained by multiplying each section's infarct area by the distance between sections.

In some sections, a part of tissue was torn in the stroke region. To compensate for missing tissue volume, the torn tissue area was obtained by subtracting the area of the ipsilateral from the contralateral side as calculated from the low magnification images. The volume of torn tis- sue was obtained by multiplying each section's missing tissue by the distance between sections. The torn tissue volume was then added to the FJC volume to calculate the total stroke volume.

Measurements of NSE activity and quantification by ELISA. Plasma was separated from whole blood samples using CAPIJECT Micro Collection Tubes (Terumo Medical Corporation, Somerset NJ). 50 μl samples of plasma were added to individual wells in a 96-well plate, and reaction mix was added just before luminescence measurements were initiated (GloMax, Pro- mega). Reaction mixtures included 1:1 ratio of NP-PK and NP-Luc, with equal mass amounts of enzyme bound to the NPs, resulting in roughly a 2:1 ratio of Luc to PK molecules. To minimize batch-to-batch differences in repeat experiments, the amounts of the NP-PK and the NP-Luc to be added was based on their individual activities. In this way, the relative activities of each enzyme were kept constant among experiments with different batches of protein. Luminescence signal was integrated for 3 seconds, every minute for 50 minutes. Control wells (-2PG) were then subtracted from the raw data and LU were integrated over the first 20 minutes of the measurements.

Integrated LU values of each time point were then normalized to t (-1 hour).

Rat NSE was quantified using an ELISA Kit, (R&D Systems, Inc., Minneapolis, MN) according to the manufacturer's directions. Non-Neuronal Enolase (NNE) was also detected using ELISA Kit, (antibodies-online.com, Atlanta, GA) according to manufacturer's directions. Assays were read using an Infinite M200Pro microplate reader (Tecan Trading AG, Maennedorf, Switzerland) and Magellan software (Tecan Austria GmbH, Grödig/Salzburg, Austria).

6.5.8 Detection of NSE in blood samples from human subjects

Plasma sample collection. 5 ml of blood was collected from enrolled subjects into Na-heparin 6 ml tubes. Tubes were spun at 1000 g for 5 minutes and then plasma was aspirated and placed over ice. Samples were divided and aliquots frozen for later analysis as indicated.

6.5.9 Detection of NSE in plasma samples from human subjects. 10 µl of freshly collected plasma was diluted with 10 µl of water and added to individual wells of a 96-well plate pre- loaded with lyophilized TET reagent mixtures for negative, test and positive control wells (in triplicates). The readout luminescence signal was integrated for 0.4 seconds, and read continuously for 25 minutes using a TECAN Safire plate reader. For calculation of NSE levels, the linear regression slope for the initial activity was calculated per each well. Then, control wells (-2PG) were subtracted from the test channel and normalized to the positive control well (with 2-PG and enolase). Positive

control reactions allowed us to normalize the results to reduce batch to batch variability. Plasma samples were sent for further analysis to ARUP laboratories (Salt Lake City, UT). Variability for PK and Luc activity between batches was addressed by preparing mixtures of the enzymes with equal activity rather than adding equal amounts of each protein.

6.6 ACKNOWLEDGMENTS

This study was funded by NIH, Pioneer Award 8DP1-EB016541 (originally 5DP1-OD-006431), “Nanoscale Energy Production for Implantable Medical Devices” (AJT); CTSC Seed Funding Program (NIH, Weill), Pilot Award, “Developing a Multiplexed Point-of-Care Plat- form to Detect Multiple Stroke Biomarkers” (AJT); NIH F32: F32AG031620 (NN) and the SUNY Research Foundation award, “Development of Hand-held Biosensors for Rapid Diagnosis and Study of Neural Disease & Neurotoxins” (AJT).

6.7 SUPPLEMENTARY MATERIALS

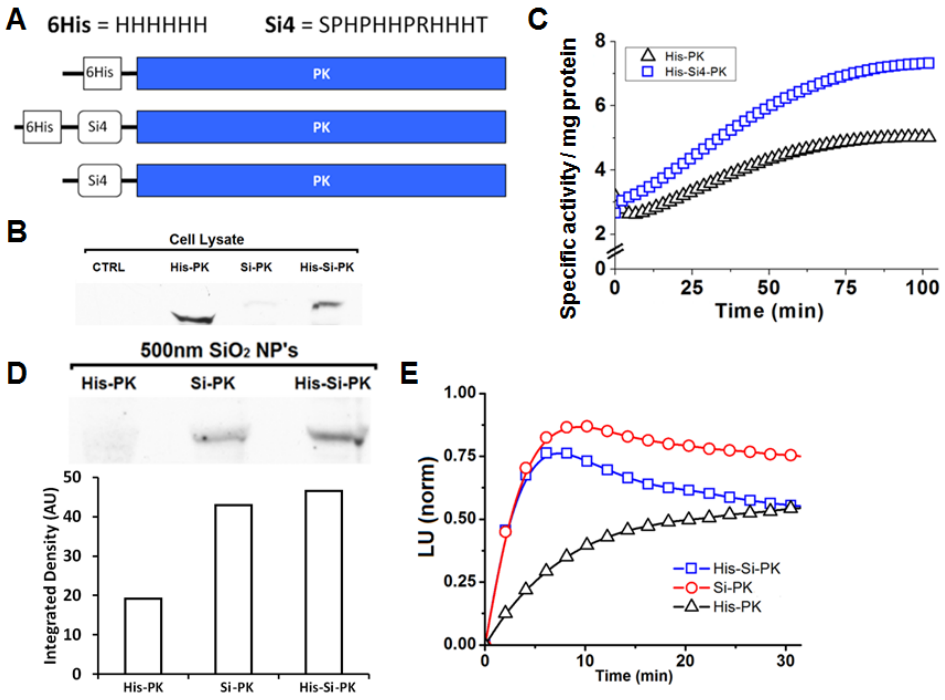

Fig. 6.S1 Construction and expression of PK-affinity tag fusion constructs. A) Schematic illustration of fusion PK constructs indicating location of the His and Si4 peptide sequences. Three fusion plasmids were constructed for PK–His-PK, His-Si-PK and Si-PK. B) HEK-293 cells were transfected with each of the 3 plasmids. 3 days later, cell lysates were separated by SDS-PAGE and then immunoblotted for PK expression, where His-PK showed highest expression level. C) His-PK and His-Si-PK were purified (using the His-tag, see methods section) and tested for their specific activity when not tethered. Protein concentrations were determined with the Micro-BCA assay (Pierce, Rockford, IL), and purity of the samples was analyzed by SDS-PAGE and immunoblotting. D) Immunoblot (top) and quantification (bottom) of protein bound to 500 nm SiO_2 NPs following incubation with whole cell lysates of His-PK, His-Si4-PK or

Si4-PK expressing cells. This comparison shows that the Si tag increases >2 fold the amount of protein bound to SiO_2 NPs. E) The activity of His-PK, His-Si4-PK or Si4-PK fusion proteins was measured when immobilized on SiO_2 NPs following incubation of whole cell lysates with the 500 nm NPs. Oriented immobilization through the Si tag of His-Si-PK (blue squares) and Si-PK (red circles) results in comparable initial reaction rates, while His-PK lacking the SiO_2 affinity tag reveals a slower activity rate most likely due to its non-specific adsorption to the NPs.

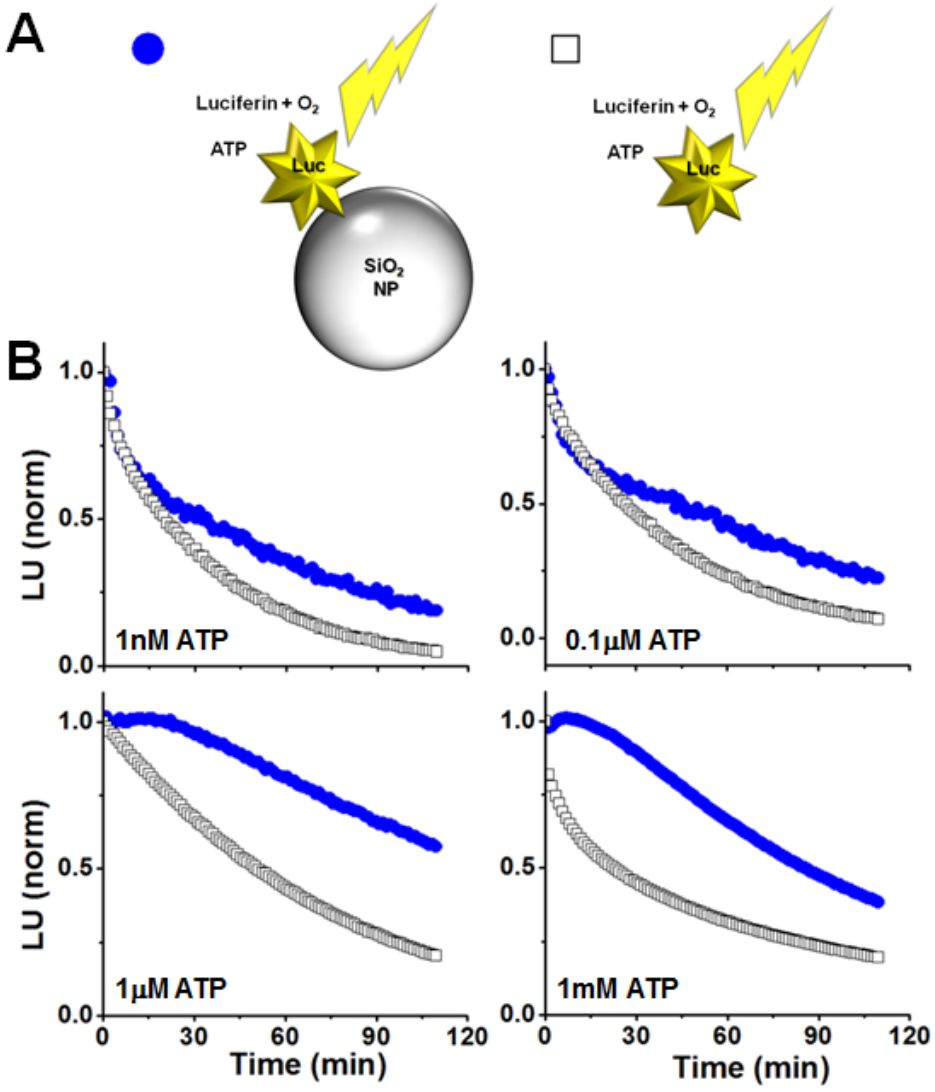

Fig. 6.S2 Supplementary analysis for PK-Luc coupled reaction as shown in Fig 6.1. A) PK and Luc coupled activity was assayed in 4 combinations: (NP-PK) + (NP-Luc), (NP-PK) + (soluble Luc), (NP-Luc) + (soluble PK) or (soluble PK + soluble Luc). Luminescence output was measured for each combination with and without PEP, as indicated by the colored symbols. All combinations included equivalent amounts of PK and Luc. Here, coupled efficiency was calculated using the analysis as used in Fig 6.5, calculated by subtracting the negative reaction (-PEP) from positive reactions (+PEP) slopes (indicated by solid lines). B) Summary of data presented in A, shows that having both PK and Luc on NPs (black) facilitates reaction rates compared to other combinations. Each condition was tested in triplicates; data shown represents 3 individual experiments; AVG±STDEV.

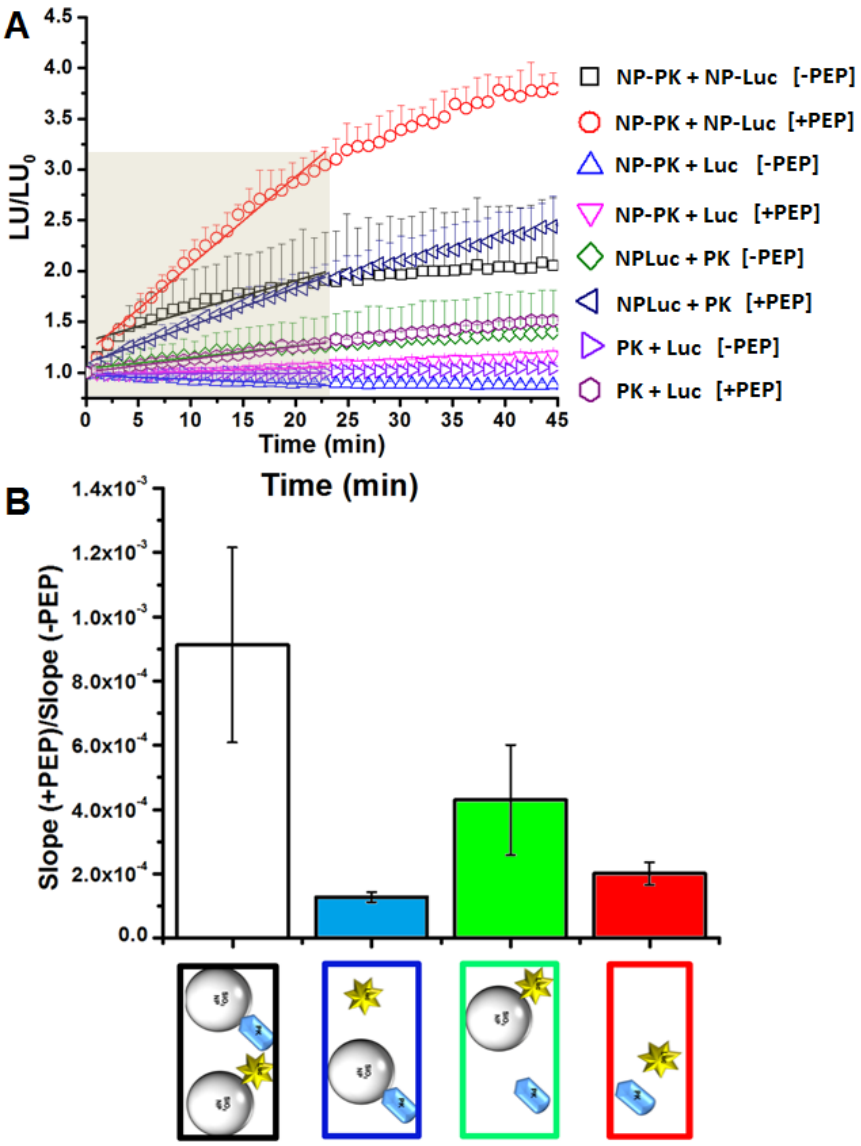

Fig. 6.S3 Determining the activity of His-Si4-Luc immobilized on silica NP's. A) Schematic representation of experimental setup in the luciferase activity assay. B) Representative traces showing the activity of Luc measured when immobilized on silica NPs (blue dots), or in solution (square) with various ATP concentrations. For these experiments, the luminescent signal was normalized against LU at time point 0, and plotted as a function of time, demonstrating a significantly slower decay time for Luc when tethered.

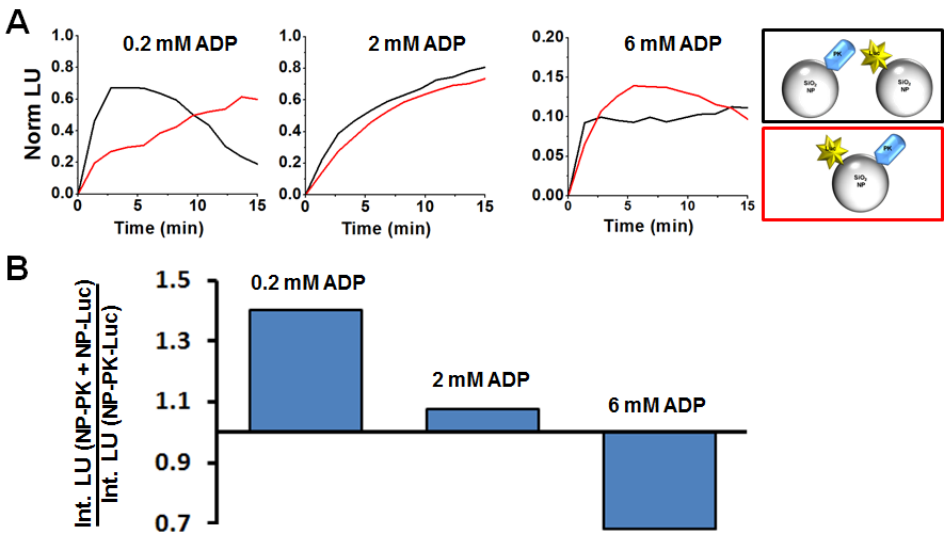

Fig. 6.S4 Co-immobilization of PK and Luc on single NPs reduced reaction efficiency when ADP was limiting. A) To investigate the effect of enzyme proximity on coupled activity more directly, His-Si-PK and His-Si-Luc were immobilized on 500 nm silica NPs separately (black) or together (red). Luminescence signal in the presence of 0.2, 2 or 6 mM ADP was normalized to t (0 min) and plotted against time (all other conditions/substrates were kept the same). B) Surprisingly, we found the activity of the coupled reactions to be significantly reduced when the enzymes were co-tethered on single particles versus tethered on separate particles. There are multiple possible explanations for this finding, ranging from steric hindrance between the two proteins when co-tethered, to interference by Luc with PK tetramers, to a competition between the enzymes for interaction with ADP [33, 34]. Such competition would reduce substrate availability for PK, resulting in overall reduced luminescence. To distinguish between these possibilities, we repeated the experiment with increased concentrations of ADP,

and found that 10-fold excess or more of ADP reversed the reduction in activity (middle and right panels), suggesting that competition for ADP was largely responsible.

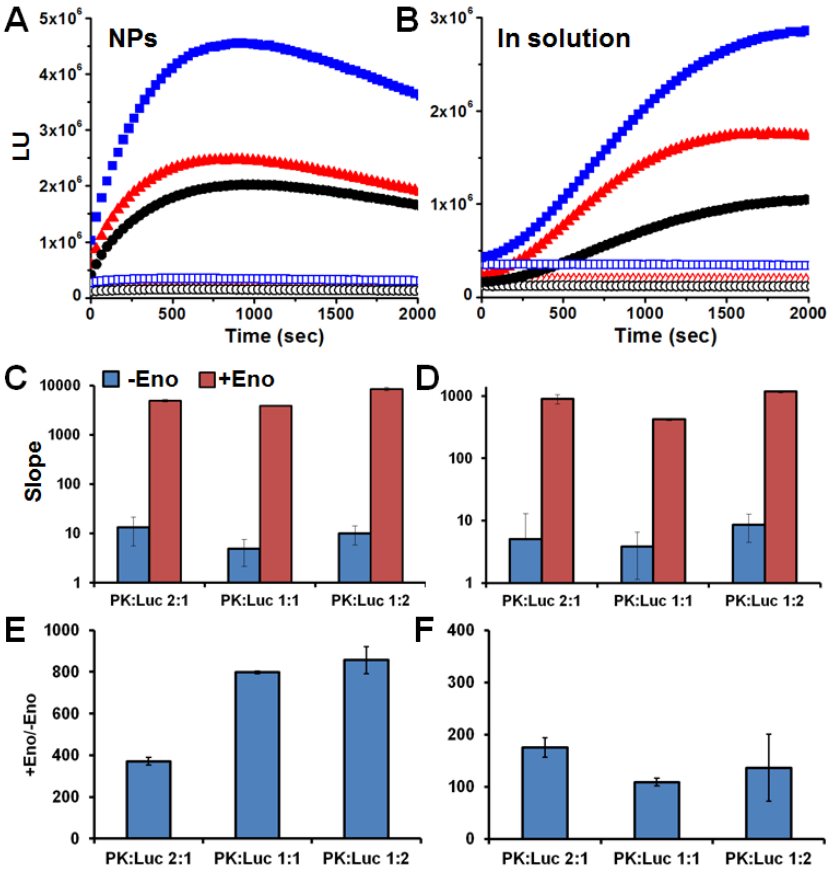

Fig. 6.S5 Testing various ratios of PK and Luc in coupled reactions to detect Enolase. A and B) Representative traces showing the luminescence output signal as measured for 3 ratios of PK and Luc on NPs (A) or in solution (B) in coupled reactions to detect Eno (PK:Luc ratios as follows- blue squares- 2:1, red triangles- 1:1, black circles 1:2; filled markers represent reaction with Eno, empty markers represent no Eno). C and D) average slopes for reaction as presented in A and B (blue bars–no Eno, red bars with Eno, AVG±STDEV). E and F) the calculated signal to background ratio for the 3

different ratios of PK:Luc when tethered (E) or in solution (F). Each ratio was tested in triplicate; AVG±STDEV.

References

1. WHO. Global burden of stroke. http://wwwwhoint/cardiovascular_diseases/en/cvd_atlas_15_burden_strokepdf. 2002;(1).
2. Maiser SJ, Georgiadis AL, Suri MF, Vazquez G, Lakshminarayan K, Qureshi AI. Intravenous recombi- nant tissue plasminogen activator administered after 3 h following onset of ischaemic stroke: a meta- analysis. Int J Stroke. 2011; 6(1):25–32. Epub 2011/01/06. doi: 10.1111/j.1747-4949.2010.00537.x PMID: 21205237.
3. Kleindorfer D, de los Rios La Rosa F, Khatri P, Kissela B, Mackey J, Adeoye O. Temporal trends in acute stroke management. Stroke; a journal of cerebral circulation. 2013; 44(6 Suppl 1):S129–31. Epub 2013/06/05. doi: 10.1161/STROKEAHA.113.001457 PMID: 23709709.
4. Brainin M, Teuschl Y, Kalra L. Acute treatment and long-term management of stroke in developing countries. Lancet Neurol. 2007; 6(6):553–61. Epub 2007/05/19. doi: 10.1016/S1474-4422(07)70005-4 PMID: 17509490.
5. Norrving B, Kissela B. The global burden of stroke and need for a continuum of care. Neurology. 2013; 80(3 Suppl 2):S5–12. Epub 2013/01/18. doi: 10.1212/WNL.0b013e3182762397 PMID: 23319486.
6. Song Y, Huang YY, Liu X, Zhang X, Ferrari M, Qin L. Point-of-care technologies for molecular diagnos- tics using a drop of blood. Trends Biotechnol. 2014;

32(3):132–9. Epub 2014/02/15. doi: 10.1016/j. tibtech.2014.01.003 PMID: 24525172; PubMed Central PMCID: PMC3962833.

7. Dash PK, Zhao J, Hergenroeder G, Moore AN. Biomarkers for the diagnosis, prognosis, and evaluation of treatment efficacy for traumatic brain injury. Neurotherapeutics. 2010; 7(1):100–14. Epub 2010/02/ 05. doi: 10.1016/j.nurt.2009.10.019 PMID: 20129502.

8. Ahmad O, Wardlaw J, Whiteley WN. Correlation of levels of neuronal and glial markers with radiological measures of infarct volume in ischaemic stroke: a systematic review. Cerebrovasc Dis. 2012; 33(1):47– 54. Epub 2011/12/03. doi: 10.1159/000332810 PMID: 22133844.

9. Wunderlich MT, Lins H, Skalej M, Wallesch CW, Goertler M. Neuron-specific enolase and tau protein as neurobiochemical markers of neuronal damage are related to early clinical course and long-term out- come in acute ischemic stroke. Clinical neurology and neurosurgery. 2006; 108(6):558–63. Epub 2006/ 02/07. doi: 10.1016/j.clineuro.2005.12.006 PMID: 16457947.

10. Culler L, Whitcomb J, Webster S. Serum neuron-specific enolase predicting neurological outcomes post-cardiac arrest: a review of the literature. Dimens Crit Care Nurs. 2014; 33(6):309–15. Epub 2014/ 10/04. doi: 10.1097/NCC.0000000000000185 PMID: 25280197.

11. Cheng F, Yuan Q, Yang J, Wang W, Liu H. The prognostic value of serum neuron-specific enolase in traumatic brain injury: systematic review and meta-analysis. PLoS One. 2014; 9(9):e106680. Epub 2014/09/05. doi: 10.1371/journal.pone.0106680 PMID: 25188406; PubMed Central PMCID:

PMC4154726.

12. Chaves ML, Camozzato AL, Ferreira ED, Piazenski I, Kochhann R, Dall'Igna O, et al. Serum levels of S100B and NSE proteins in Alzheimer's disease patients. Journal of neuroinflammation. 2010; 7:6. Epub 2010/01/29. doi: 10.1186/1742-2094-7-6 PMID: 20105309; PubMed Central PMCID: PMC2832635.

13. Wevers RA, Jacobs AA, Hommes OR. A bioluminescent assay for enolase (EC 4.2.1.11) activity in human serum and cerebrospinal fluid. Clinica chimica acta; international journal of clinical chemistry. 1983; 135(2):159–68. PMID: 6652924.

14. Viallard JL, Murthy MR, Dastugue B. An ultramicro bioluminescence assay of enolase: application to human cerebrospinal fluid. Neurochemical research. 1985; 10(12):1555–66. Epub 1985/12/01. PMID: 4088431.

15. Wevers RA, Theunisse AW, Rijksen G. An immunobioluminescence assay for gamma-gamma enolase activity in human serum and cerebrospinal fluid. Clin Chim Acta. 1988; 178(2):141–50. Epub 1988/12/ 15. PMID: 3072116.

16. Halliwell CM, Morgan G, Ou CP, Cass AE. Introduction of a (poly)histidine tag in L-lactate dehydroge- nase produces a mixture of active and inactive molecules. Analytical biochemistry. 2001; 295(2):257– 61. Epub 2001/08/08. doi: 10.1006/abio.2001.5182 PMID: 11488630.

17. Travis AJ, Foster JA, Rosenbaum NA, Visconti PE, Gerton GL, Kopf GS, et al. Targeting of a germ cell- specific type 1 hexokinase lacking a porin-binding domain to the mitochondria as well as to the head and fibrous sheath of murine spermatozoa. Molecular biology of the cell. 1998; 9(2):263–76. Epub 1998/04/04. PMID: 9450953; PubMed Central PMCID: PMC25249.

18. Travis AJ, Jorgez CJ, Merdiushev T, Jones BH, Dess DM, Diaz-Cueto L, et al. Functional relationships between capacitation-dependent cell signaling and compartmentalized metabolic pathways in murine spermatozoa. The Journal of biological chemistry. 2001; 276(10):7630–6. Epub 2000/12/15. doi: 10. 1074/jbc.M006217200 PMID: 11115497.

19. Mukai C, Bergkvist M, Nelson JL, Travis AJ. Sequential reactions of surface-tethered glycolytic enzymes. Chem Biol. 2009; 16(9):1013–20. Epub 2009/09/26. doi: 10.1016/j.chembiol.2009.08.009 PMID: 19778729; PubMed Central PMCID: PMC4051345.

20. Mukai C, Gao L, Bergkvist M, Nelson JL, Hinchman MM, Travis AJ. Biomimicry enhances sequential reactions of tethered glycolytic enzymes, TPI and GAPDHS. PLoS One. 2013; 8(4):e61434. Epub 2013/04/30. doi: 10.1371/journal.pone.0061434 PMID: 23626684; PubMed Central PMCID: PMC3634084.

21. Oren EE, Notman R, Kim IW, Evans JS, Walsh TR, Samudrala R, et al. Probing the molecular mecha- nisms of quartz-binding peptides. Langmuir. 2010; 26(13):11003–9. Epub 2010/05/27. doi: 10.1021/ la100049s PMID: 20499870.

22. Naik RR, Brott LL, Clarson SJ, Stone MO. Silica-precipitating peptides isolated from a combinatorial phage display peptide library. J Nanosci Nanotechnol. 2002; 2(1):95–100. Epub 2003/08/12. PMID: 12908327.

23. Nakamura M, Mie M, Funabashi H, Kobatake E. Construction of streptavidin-luciferase fusion protein for ATP sensing with fixed form. Biotechnol Lett. 2004; 26(13):1061–6. Epub 2004/06/26. doi: 10.1023/ B:BILE.0000032966.17759.08 5379493 [pii]. PMID: 15218380.

24. Casmiro M, Maitan S, De Pasquale F, Cova V, Scarpa E, Vignatelli L. Cerebrospinal fluid and serum neuron-specific enolase concentrations in a normal population. Eur J Neurol. 2005; 12(5):369–74. Epub 2005/04/05. doi: 10.1111/j.1468-1331.2004.01021.x PMID: 15804267.

25. Marginean IC, Stanca DM, Vacaras V, Soritau O, Margiean M, Muresanu DF. Plasmatic markers in hemorrhagic stroke. J Med Life. 2011; 4(2):148–50. Epub 2011/07/22. PMID: 21776296; PubMed Cen- tral PMCID: PMC3124268.

26. Hayashi T, Matuo Y. A new stroke marker as detected by serum phosphoglycerate mutase B-type iso- zyme. Biochemical and biophysical research communications. 2001; 287(4):843–5. Epub 2001/09/28. doi: 10.1006/bbrc.2001.5666 PMID: 11573940.

27. Chung JW, Ryu WS, Kim BJ, Yoon BW. Elevated calcium after acute ischemic stroke: association with a poor short-term outcome and long-term mortality. J Stroke. 2015; 17(1):54–9. Epub 2015/02/19. doi: 10.5853/jos.2015.17.1.54 PMID: 25692107; PubMed Central PMCID: PMC4325634.

28. Stippler M, Fischer MR, Puccio AM, Wisniewski SR, Carson-Walter EB, Dixon CE, et al. Serum and cerebrospinal fluid magnesium in severe traumatic brain injury outcome. J Neurotrauma. 2007; 24 (8):1347–54. Epub 2007/08/23. doi: 10.1089/neu.2007.0277 PMID: 17711396.

29. Hasan N, McColgan P, Bentley P, Edwards RJ, Sharma P. Towards the identification of blood biomark- ers for acute stroke in humans: a comprehensive systematic review. British journal of clinical pharma- cology. 2012; 74(2):230–40. Epub 2012/02/11. doi: 10.1111/j.1365-2125.2012.04212.x PMID: 22320313;

PubMed Central PMCID: PMC3630743.

30. Mukai C, Bergkvist M, Nelson JL, Travis AJ. Sequential reactions of surface-tethered glycolytic enzymes. Chem Biol. 2009; 16(9):1013–20. Epub 2009/09/26. S1074-5521(09)00278-6 [pii] doi: 10. 1016/j.chembiol.2009.08.009 PMID: 19778729.

31. Lata JP, Gao L, Mukai C, Cohen R, Nelson JL, Anguish L, et al. Effects of Nanoparticle Size on Multi- layer Formation and Kinetics of Tethered Enzymes. Bioconjugate chemistry. 2015. Epub 2015/08/19. doi: 10.1021/acs.bioconjchem.5b00354 PMID: 26280845.

32. Schaffer CB, Friedman B, Nishimura N, Schroeder LF, Tsai PS, Ebner FF, et al. Two-photon imaging of cortical surface microvessels reveals a robust redistribution in blood flow after vascular occlusion. PLoS biology. 2006; 4(2):e22. PMID: 16379497.

33. Ford SR, Chenault KD, Hall MS, Pangburn SJ, Leach FR. Effect of periodate-oxidized ATP and other nucleotides on firefly luciferase. Arch Biochem Biophys. 1994; 314(2):261–7. Epub 1994/11/01. S0003-9861(84)71440-8 [pii] doi: 10.1006/abbi.1994.1440 PMID: 7979363.

34. Ford SR, Chenault KH, Bunton LS, Hampton GJ, McCarthy J, Hall MS, et al. Use of firefly luciferase for ATP measurement: other nucleotides enhance turnover. J Biolumin Chemilumin. 1996; 11(3):149–67. Epub 1996/05/01. doi: 10.1002/(SICI)1099-1271(199605)11:3<149::AID-BIO411>3.0.CO;2-Q PMID: 8844345.

CHAPTER 7

THE DEVELOPMENT OF A MIDDLE SCHOOL SCIENCE CURRICULUM TO FURTHER DEVELOP THE UNDERSTANDING OF ENGINEERING AND PHYSICS APPROACHES TO SOLVING BIOLOGICAL PROBLEMS

This chapter presents two main parts, the first one is the design and development of a middle school biological science curriculum, which explain the concepts of inflammation, Alzheimer's disease, plugging phenomena and blood flow in the brain of healthy and disease states. In the second part, this chapter presents an unpublished educational manuscript, which introduces the concepts of fluorescence and collateral transport to the students. The second part of this chapter has been coauthored with Amanda Bares, another graduate student, and an identical version of this chapter appears in her thesis. In the second part of the chapter, we had the students use an oak leaf to study what happens to transport when collateral pathways are and are not present after an injury. We then translated this idea over to the human cerebral vasculature and discussed some of the research that was being conducted in SN lab. The writing style in this chapter diverges from the rest of the chapters as it is meant to help motivate and guide middle school teachers to replicate this activity in their classroom.

PART I: Modeling of brain capillary network and leukocyte capillary plugging

7.1 ABSTRACT

We have developed a module to help middle school students apply their quantitative approaches and physics knowledge to solve biological questions. The specific goal of this activity was understand and simulate how blood flow at the normal conditions differs from blood flow under brain inflammation or microstrokes. In order to achieve these goals, we had the students construct a vascular network similar to the capillary network in the brain to study what happens to the flow when one or multiple components of the network get obstructed. We then translated this idea over to the brain capillary network and discussed some our research that was being conducted in our lab. An evaluation of the curriculum in the form of a lab report and survey, yielded an increase in understanding of concepts in biology and physics as well as how these two fields can be applied into the biomedical research. The writing style in the first part of this chapter diverges from the rest of the chapters as it is meant to help motivate and guide middle school teachers to replicate this activity in their classroom.

7.2 INTRODUCTION

The microvasculature system (the portion of the circulatory system composed of the smallest vessels, such as the capillaries, arterioles, and venules) (Fig. 7.1) is comprised a series of feeder vessels and networks with extensive redundant connections [1]. Normal brain function is completely dependent of adequate level of blood flow, since the brain energy usually comes from oxygen-dependent metabolism (i.e., blood sugar). To

maintain the adequate blood flow, the brain has extensive inter-connections between capillaries to provide a high surface area for gases and nutrients exchange. In addition, if there is a potentially adverse event (strokes, microhemorrhages, atherosclerosis, etc.) that can cause miss-function in any of these vessels (i.e. a blood clot, stalls, ischemia, etc.) the redundancy of this microvasculature network allows blood flow to be redistributed with minimal damage to the brain (Fig 7.2) [2]. As a result the obstruction or malfunction of one of the capillaries would expect a reroute of flow to the neighboring capillary, a change in pressure and eventually blood flow velocity across the microvasculature network.

We present an inquiry-based activity that was recently taught to a seventh- grade class. The purpose of this lab was to develop an understanding of how engineering and physics is involved in science such as neurobiology and behavior. To initiate this activity, students will first learn about optics and how new advances in imaging allow us to perform *in vivo* experiments and study the progression of diseases at cellular level. In addition student learn about the main pathological condition present in dementia and other neurodiseases, and finally the students were invited to perform the experiments. By conducting these experiments, students will strengthen their understanding of scientific inquiry, including further development of their ability to generate and test hypotheses.

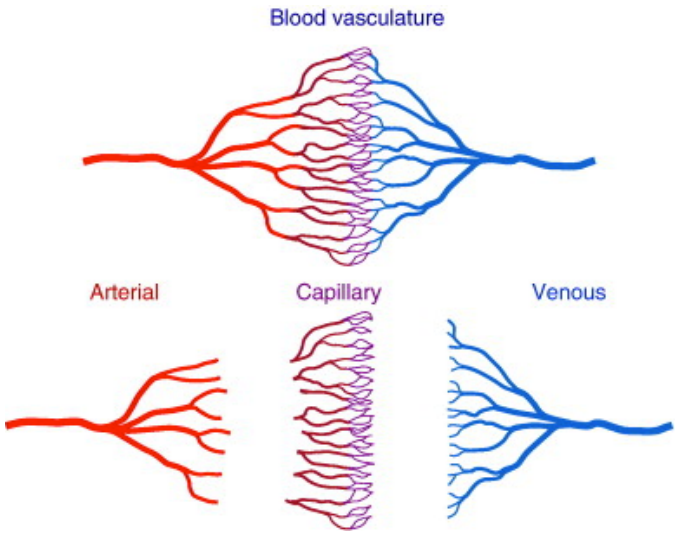

Figure 7.1 Branching of a typical microvasculature showing the inter connection between the capillaries network.

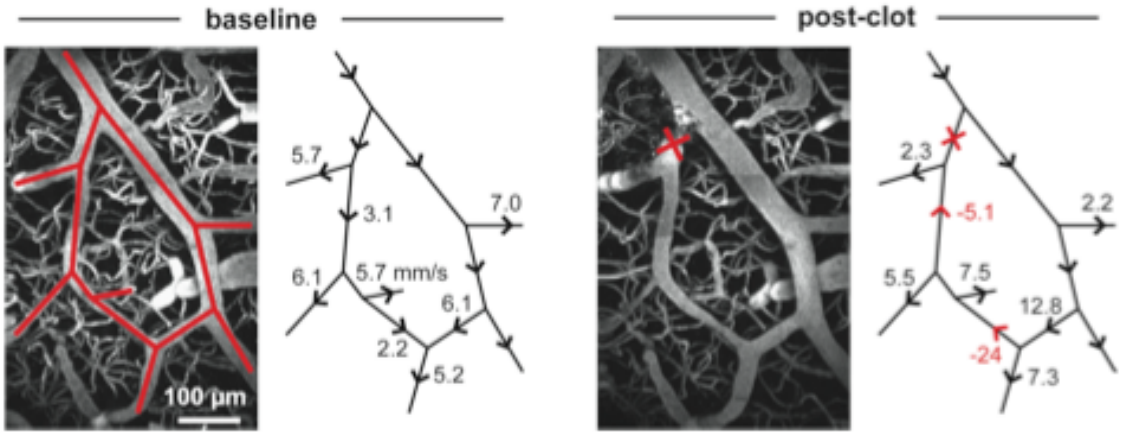

Figure 7.2 Loops in surface arterial network provide collateral flow. Case study highlighting the importance of vascular loops following a vessel occlusion. For baseline and post-clot examples, the left panels are magnified fluorescence images of the surface vasculature, with an arterial network outlined. Right panels show the network schematics with blood flow speeds in the vessels of interest, with arrows indicating direction of blood flow. Note that after optochemically inducing a clot (red X under post-clot), blood

flow does not stop, but is maintained through the reversal of flow in two vessels (red arrows and values). These redundant loops help support collateral flow and minimize the pathological effects associated with a blocked vessel[2].

7.3 LESSONS

We split this activity into two separate lessons, with students working in groups of four or five. In the first section, an open- class discussion was held to explain the main concepts of optics and flow in biology how this lab is analogous to flow in the brain and physiological consequences that may arise from complications in blood flow (45 minutes). Second, the experiment was performed, they create a vascular system to help flow transport network and understand the significance of collateral loops (~1 hour).

7.4 LABORATTORY COMPONENTS

The implementation of the lab took place in the biological science teaching classrom at Boynton Middle School in Ithaca, NY . Students were asked to build a network of serial and parallel connecting tubes in which bead solution can flow through. Students were asked to draw a schematic of the network and measure the dimensions of each segment of tubing for future analysis. Finally, the students were asked to hypothesize the flow direction of the bead solution through the network of tubing before and after a blockage in one of the channels in the tube. Figure 7.3 shows a schematic network and the pre-modeling system analogous to the vasculature in the brain made during the lab.

Students then connected their network of tubes to a syringe pump or peristaltic pump

containing bead solution. The bead solution was set to flow at a constant flow rate while the students measured the time it took for beads to travel a given distance, yielding velocity, using screen projector.

Once velocity measurements were taken for all tube segments in the network, students were asked to block a segment to study the rearrangement and distribution of flow after blockage. Students blocked a segment then repeated velocity measurements as described above for each segment of the network.

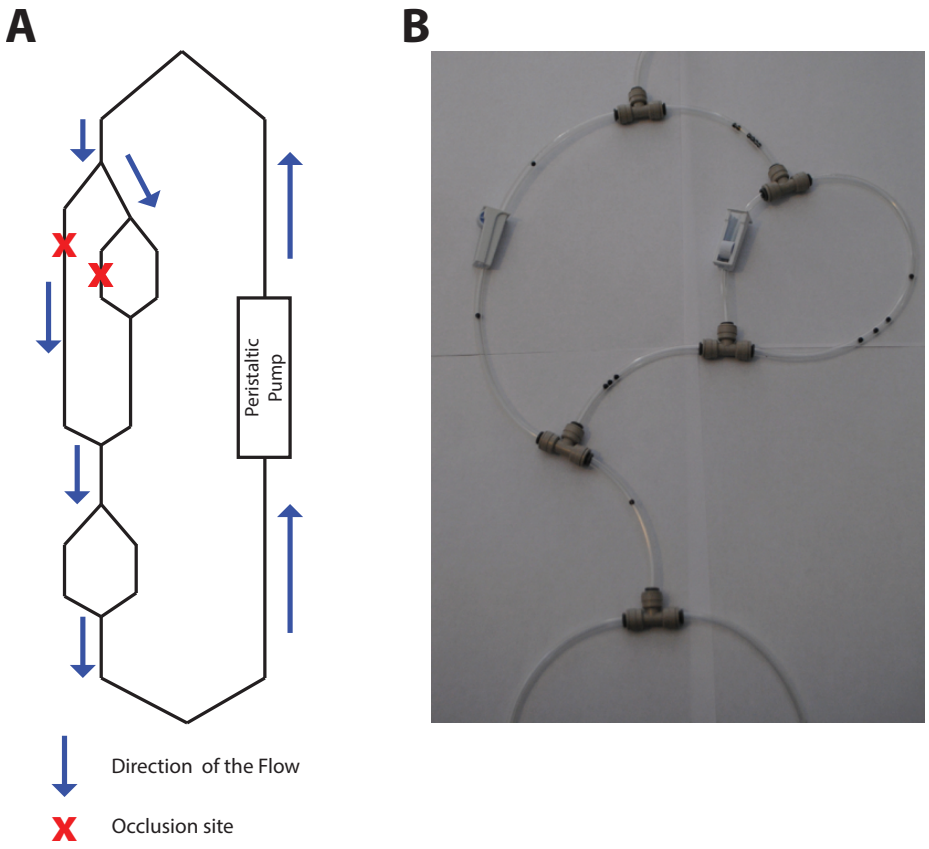

Figure 7.3 Schematic of vascular network. (A) Network design. (B) Pre-modeling system (tubing, connectors, clamps and beads).

7.5 MATERIALS AND METHODS

7.5.1 Materials:

- Flexible tygon tubing (Cat# EW-95665-09, Cole Parmer)
- Connectors (Cat# ZW-30726-01, Cole Parmer)
- Necklace spherical beads (local store)
- Roller clamps (Cat# LRC001, Europlaz)
- Peristaltic pump (Cat# 50220, Studica)

7.5.2 Procedure:

Students will design and assemble a simple network using Tygon tubing, connectors and roller clamp. They will predict the flow pattern/ direction of bead flow, and which channels have faster or slower beads. They should record their predictions. They will pump in a bead solution (beads + water + red colorant) at a constant flow rate and watch the flow profile in each tube "channel". This will verify their predictions.

They will then block a channel and predict a new flow profile and velocity of beads.

They will measure the velocity of the beads in the blocked network.

1. Draw a schematic of your network and hypothesize the network flow before and after a block in one of the channels.
2. Use the tubing, connectors and roller clamps and create your own network.
3. Connect your model to the peristaltic pump. Set the peristaltic pump to constant flow rate until the solution (water + red colorant) fills the entire network.

4. Fill the main channel of the system with bead solution. Seal your system and connect it to the peristaltic pump.
5. Connect the computer to the projector and put your system under the computer camera.
6. Look at the projection of the channels and make sure you can visualize the beads. If the beads are moving too fast, decrease the flow rate.
7. You are expected to measure the velocity of the beads in each channel; some channels may have similar velocities.
8. Measure velocity by counting the number of beads that pass through a channel over a given amount of time. Or the time it takes for 1 bead to pass through the channel. You will be expected to track more than 10 particles per channel type in order to get statistically relevant data.
9. When you have obtained the bead velocities for each channel, you will use the blocking tool to block 1 channel roller clamp). The purpose of the blockage is to see a redirection of flow e.g. redistribution of the flow and a change in velocity. Block the channel wait a minute until the network has reached a steady state.
10. Measure the velocity in each channel as well as note if there is redirection of flow.

7.5.3 Classroom Activity:

Engage (Time: 15 min)

Allow students to construct the microfluidic device using the flexible tube and valves before they conduct any mixing experiments. Encourage them to discuss and write down their observations of differences in the blood flow behavior under certain conditions.

Explore (Time: 40 min)

Exploration and explanation are concurrent in this lab, owing to its many parts. Move students through each section of the lab, encouraging them to stop and observe flows of a previous designed vascular network of the brain (healthy) before fully construct their different model of brain stroke. When doing the annular shear flow experiment, encourage students to draw a design of their choosing, and to look at the effect of distance from the stalling (occlusion) and the reduction in the blood flow down stream of the "stroke area."

Explain (Time: 25 min)

At each stage, ask directed questions about their observations (Are the flows the same? How are they different?) The students' observations will immediately help them learn many fundamental aspects of fluid mechanics. Guide these observations with additional explanations; in particular point out fluid deformation, shear stress, and increasing shear near the moving boundary. Also how the different modification in the vascular network affect the rate of blood flow.

7.6 EVALUATION OF THE CURRICULUM

Students were asked to complete a laboratory report on the network flow laboratory. The students were to answer a series of questions pertaining to the network they designed and to core concepts in flow and how it related to biology. The following questions were asked:

I. Observation

a. What does blood bring to cells?

_____

b. Why is proper blood flow critical in the brain?

_____

II. State the Question

(*Hint – What are you trying to find out through this experiment?)*

_____

III. Form a Hypothesis

a. Based on the question that your group will be investigating, what is the dependent variable?

_____

b. Based on the question that your group will be investigating, what is the independent variable?

_____

c. Write the hypothesis for your investigation - Remember that the formula for writing a hypothesis is "**If** (independent variable) **then** (dependent variable) **because** (logical explanation)"

_____

IV. Experiment

a. In our experiment, what do the tubes represent?

_____

b. What do the clamps represent?

_____

c. What does the pump represent?

_____

d. What do the beads represent?

_____

e. Why are we counting the number of beads that pass through?

IV. Record the Data

Baseline = No Clot

Branch	Trial 1	Trial 2	Trial 3	Average

With Clot

Branch	Trial 1	Trial 2	Trial 3	Average

V. Analyze the data

a. Calculating percent of Blood Flow

% Blood Flow Compared to Baseline = (BF in Branch with Clot / Baseline) x 100

Branch	% Blood flow compared to baseline calculations	Results

b. When you graph, remember you have a TASK ahead of you!

1. Give the graph a Title
2. Number the Axes
3. Check your Scale to plot points
4. Key – We will not need one today

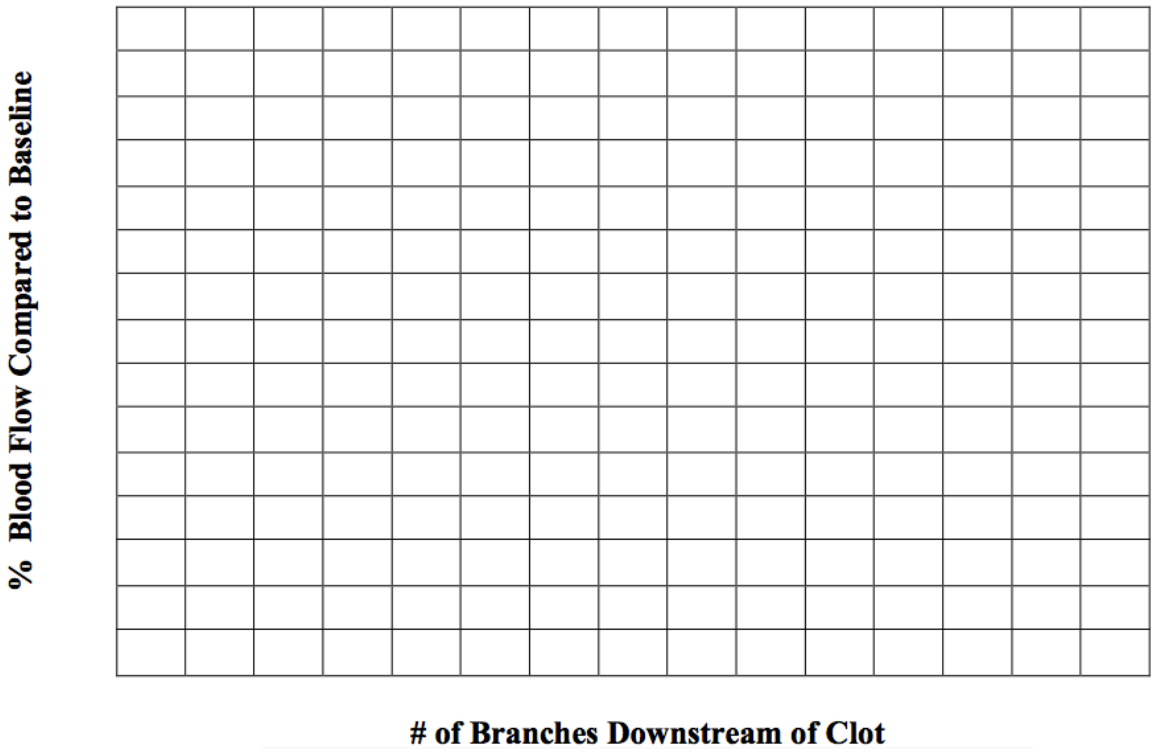

c. Did the "clots" reduce the blood flow in all parts of the brain? Why or why not?

VI. Form a conclusion

On the lines below, form a paragraph that answers the question you worked to answer in this lab. To write your conclusion, answer the following **in this order**:

- Restate the question
- Restate the hypothesis
- Restate the analysis
- State whether the data SUPPORT or DO NOT SUPPORT your hypothesis.
- Describe which sources of error may have affected ***your*** data

- Explain why you think this lab simulates what happens when a clot forms in the brain

7.7 CURRICULUM ASSESSMENT:

Students were asked to fill out a series of survey questions to evaluate the activity. The statements they were asked to evaluate were:

1. After conducting this experiment, I feel I understand how science can be applied to real-world applications
2. After conducting this experiment, I feel I understand how different science disciplines, such as physics, can be applied to other fields such as neuroscience.
3. I am more excited about science than before.
4. I enjoy this research experiments more than most labs.
5. After conducting this experiment, I feel I understand how scientists design their own experiments.
6. This experiment was more difficult than most labs.

   Students were to evaluate these statements based on a numerical score between 1 and 5, with 5 being that the student agreed strongly with the statement and 1 being that the student disagreed strongly with the statement.

7.8 CONCLUSIONS

This curriculum was designed to be very dynamic and cooperative, and as a consequence the students really appreciated it. We introduce the concept of using engineering and physics approaches to solve biological problems in a research setting. Students were provided with guidance from the teacher and graduate student in their laboratories and

were encouraged to use inquiry-based learning and rational thinking to solve the biological problems presented in the labs.

References

1. Robbins, Stanley L, Vinay Kumar, and Ramzi S. Cotran. Robbins and Cotran Pathologic Basis of Disease. Philadelphia, PA: Saunders/Elsevier, 2010. Print.
2. Schaffer CB, Friedman B, Nishimura N, Schroeder LF, Tsai PS, Ebner FF, Lyden PD, Kleinfeld D. Two-photon imaging of cortical surface microvessels reveals a robust redistribution in blood flow after vascular occlusion. Plos Biol 2006; 4(2):258-270.

PART II: FLUORESCENCE IN LEAF VEINS: AN INQUIRY MODULE

7.9 ABSTRACT

This hour-long activity introduces students to the concept of liquid flow through leaf veins, and explores what occurs when the leaf is damaged. This module is designed to allow students to openly explore the concept of network redundancy using inquiry methods similar to real research labs. Students damage the veins in tree leaves, make prediction about how this will affect transport, and then soak the stems in fluorescent dye. While the leaves are taking up dye, they explore the concept of fluorescence using lights and colored glass filters. They then use the lights and filters to view the pathway the dye traveled in the leaf, and thus to test their hypotheses on how leaf damage affects liquid flow. Students discover that small veins in the leaf allow the dye to travel around the points of damage, enabling un-interrupted flow. This concept of redundancy is critical in a variety of networks, ranging from biological networks like blood vessels to man-made networks like the electrical power grid.

7.10 INTRODUCTION

Blood travels through vessels in the body and provides oxygen and nutrients to surrounding cells. If blood flow is disrupted, catastrophic damage can occur. There is substantial redundancy in these blood flow networks in many organs, especially in the brain, resulting in alternate routes for blood to reach the tissue if one route is blocked or damaged. This module describes an ~1 hour long, inquiry-based learning activity where students discover the concept of redundancy by following the flow of fluorescent dye

through small vein networks in leaves. Students damage the vein networks in some leaves, make predictions about how this will impact transport, and then compare the transport of fluorescent dye through veins in damaged and undamaged leaves. While dye is being taken up by the leaves, students compare how similarly-colored fluorescent and non-fluorescent solutions interact with light. Through this, they discover the concept of fluorescence and then immediately appreciate why a fluorescent dye is being used as a tracer in the leaf vein networks. Students are then able to test their ideas about how vein damage will influence transport in the leaf and they find that redundancy in the leaf vein network ensures liquid from the stem can route around damaged pathways and reach the entire leaf. Emphasis is placed on student-lead inquiry, so students do not have a set series of steps to follow to reach a "correct" answer and rather are encouraged to explore with no written materials and only minimal verbal guidance. This module introduces inquiry-based learning to students in a short, manageable timeframe, allowing them to explore using the open-ended approach to scientific questions that is used in actual research labs.

7.11 ENGAGE

Begin with a brief introduction to leaf veins and the role they play in transporting liquid and nutrients to all cells of the leaf. Students should have freshly-collected leaves they can examine. Leaves with highly interconnected vein networks are necessary to illustrate the concept of network redundancy providing resilience to damage (we have found oak leaves work well). Because the concept of "networks" may be hard to grasp, relate the leaf vasculature to a set of water pipes. If water is flowing through pipes, and there's a

hole in a pipe, where does the water go? Ask students to predict what happens if an insect takes a bite out of a leaf and damages a vein. Does the whole leaf die? What happens to liquid transport? Tell the students that they can test their ideas by damaging leaves with a hole punch and using a colored dye to track liquid flow.

7.12 EXPLORE

Have students form small groups and task them with damaging the leaves using a hole punch or other tools (Figure 7.4A). Encourage them to keep some leaves intact so they can compare damaged leaves with normal ones. Make sure to provide enough leaves so students are willing to explore their own hypotheses, like ripping part of the leaf, scoring it, or other creative approaches. To keep track of expected results, have students trace the leaves they damaged as well as control leaves onto a sheet of paper and sketch out the pattern of large veins, marking where they made holes or otherwise damaged the leaf. Students should then trim the end of the leaf stem at an angle using a pair of scissors so that liquid easily absorbs into the stem and insert the stems of all leaves (including control leaves) into the 30 mL tube of Rhodamine B dye and allow them to soak (Figure 7.4B). Warn students that the dye can stain clothing and skin, to be careful inserting the leaves, and to wear gloves (lab coats and goggles are also recommended). While the leaves soak, ask students to predict where the dye will flow by tracing on their sketches of the leaf vein networks from damaged and undamaged leaves (Figure 7.4C, 7.4D, 7.4E)**.** Ask the student groups to generalize this prediction by writing down, in their own words, a hypothesis on how leaf vein disruption affects liquid flow.

While the students are conducting these tasks, the instructor should prepare extra damaged and control leaves to soak in the fluorescent solution and should also soak some control leaves in the non-fluorescent colored water to use as an example during the Extend and Elaborate phase.

While the leaves are soaking point out the two vials of dye; one holding Rhodamine B (fluorescent) and one holding colored water (non-fluorescent, should be mixed to roughly match the color of the Rhodamine B), unbeknownst to the students. The fluorescence is best seen in a dark room, so turn out the lights and close any shutters. Ask students to "tell you" what is different between the two dyes, and to work in groups to discover the differences. Inform them that they can use all the supplies on the table to explore the dyes and gather clues. When the green colored light source lights up the fluorescent dye, it will glow orange. Looking at the fluorescence through a red colored glass filter helps separate this "glow" from the color of the dye itself and the color of the light (Figure 7.5). Do not point out to the students that they need to use the light source and filters to view fluorescence, but rather, let them figure it out for themselves. If students feel frustrated, ask them about their approach and encourage them to use some of the supplies on the table. If one student in the group discovers the fluorescent "glow" first, encourage them to describe what they found to the rest of their group.

7.13 EXPLAIN

As each group begins to piece out the difference between the fluorescent and non-fluorescent solutions and identify one as "glowing," engage them in a discussion of what

they are observing. If the term “fluorescence” doesn’t come up, define the “glow” as fluorescence and explain that some molecules have this property. Ask students why they had to use the colored light and colored glass filter to see this effect. Piece together an explanation based on student words and terms. Explain that fluorophores (fluorescent molecules) absorb energy from a light source of one color and then release that energy as light of another color. The color of light emitted by the dye is redder or longer wavelength than the color of light absorbed by it. For example, in this experiment the fluorescent dye Rhodamine-B is excited with green light and emits orange light. In contrast, the colored water only absorbs the green light and does not glow or emit orange light. The instructor can then shine a green laser pointer through these fluorescent and non-fluorescent solutions to further illustrate the difference. After a student group has mastered this general concept of fluorescence, ask them “Why do you think your leaves are soaking in the fluorescent dye?” Students will typically immediately appreciate that they can use the colored light and colored glass filter to see where the dye has gone and thus test their original hypotheses about transport in the leaf vein networks.

7.14 EXTEND AND ELABORATE

After the exploration of fluorescence, the students will extend this concept and use it as a tool to explore liquid transport in their damaged and control leaves (Figure 7.6). Ask the students to test their hypothesis of how leaf damage changes liquid transport. Once students realize that the dye goes “around” the holes they made in the leaf veins, ask them to figure out how the dye got there. They will quickly realize that there are tiny veins all throughout the leaf that liquid travels through, bypassing the damage to the

larger veins. While students are exploring their hypotheses, circulate around the room and ask questions to guide their thinking. Ask them about their approach, or why they are making their conclusions. Avoid giving answers or encouraging a "right" answer. Rather, guide them through the exploratory process. If students are wondering why they cannot simply use a colored dye to see where the liquid travels, show them the leaf that was soaked in colored water to demonstrate that colored water alone is not sufficiently visible within the leaf network to discern transport pathways. Light must be generated through fluorescence and "detected" by their eye with the aid of a filter. Occasionally, dye will not be taken up into a leaf. Allow groups to share control and damaged leaves with other groups if necessary, or provide your own experimental and control leaves for substitution.

End the activity by asking the groups if anyone guessed the flow of dye correctly. If so, have them explain to the class why they made their initial prediction. Typically, most groups hypothesize that dye will stop at points of damage and not progress to downstream veins. Ask students to explain why they thought that, and why that differs from what actually happened. Because the leaf vasculature is a complex network composed of large veins and many interconnected small veins, liquid can travel through many routes to reach the same point. The dye travels *around* the damaged areas using smaller vein networks and continues to travel through the rest of the network. These smaller networks are actually visible with the fluorescent dye (Figure 7.6A), and are also visible to the naked eye when examined closely enough, depending on the leaf. Most seeding plants such as oak trees exhibit redundant vascular networks (reticulated venation) with a number of small interconnections between main veins (anastomosis).

Non-redundant leaves, such as ginkgo biloba, have a fan shape with veins extending radially from the leaf base, and do not exhibit vein interconnections (dichotomous venation) [1].

End the activity by asking students about other networks like this. Some possible ideas are blood vessels, electrical power networks, roads, etc. Conclude with a short presentation describing how these networks are "redundant". Redundancy is a key concept in many fields, ranging from biology to technology. In a complex network, repetition of certain components ensures that the whole system does not fail if one part fails. For example, if the power grid that supplies energy to every building does not contain redundancies, one fallen power line could result in widespread power outages (see the Wall Street Journal's, The Short Answer: How Does The U.S. Power Grid Work video from February 5th, 2014 for an introduction to this concept).

In biology, and specifically in this module, we examined redundancy in the circulatory system of leaves. If a portion of a leaf is damaged by weather or an insect, the rest of the leaf and the entire plant can bypass this damage and provide nutrients to cells in undamaged portions. The same is true in an animal or human circulatory system. If a small clot occurs in a tissue where the vasculature is redundant, blood can bypass the area and reach surrounding tissue.

As an analogy, the brain and the heart are the two organs in the human body with the highest energy (and thus blood) demands and their continued function is essential. If the

vascular network in these organs is disrupted, cells may become permanently damaged because they no longer have the oxygen and energy they require. Tor this reason, these organs have evolved a high degree of anastomosis (interconnections between different parts of the network) to reroute blood flow in the event of vascular damage. On the other hand, the digestive system does not exhibit significant anastomosis, as energy demands of the organ can be reduced by the brain to accommodate for damage and the resulting decrease in blood flow.

For example, if small vessels are damaged (like in a bruise), the tissue *after* that injury is not affected. However, areas of the body that are very sensitive to blood flow changes might be affected if blood vessel damage occurs there. One of the organs most sensitive to changes in blood flow is the brain. The cells of the brain, neurons, store very little energy and are highly dependent on blood flow for their nutrients. It is easy to see that blocking a blood vessel to the brain or in the brain could be disastrous. Redundancy in networks minimizes this effect, but even small disruptions in blood flow lead to damage in the brain. That is why strokes and hemorrhages can be so disastrous for patients.

7.15 EVALUATE

This activity serves as an excellent way to introduce inquiry, open-ended learning, to a class without the emphasis on a "right-answer" or correct protocol. However, evaluation for student participation and engagement can be included if needed (see Online Supplemental Materials). A generalized rubric emphasizing the content, process, and attitude of the students during this module may serve as a baseline.

7.16 CONCLUSIONS

This experiment incorporates inquiry learning, or learning through discovery, in a short, manageable time frame. It allows students to experience how science really takes place in research labs by generating hypotheses and using observations to test and form new hypotheses. This activity also connects multiple fields of study: plant biology, anatomy and physiology, and fluorescent imaging, mimicking the highly interdisciplinary approach to modern day science.

7.17 SAFETY CONCERNS

All materials for this experiment are relatively safe. The Rhodamine-B dye is not toxic, but should not be ingested. All dyes can stain clothing, so warn students not to spill. Warn students to be careful with the glass filters and immediately clean up the glass shards if a filter is dropped.

7.18 RESULTS

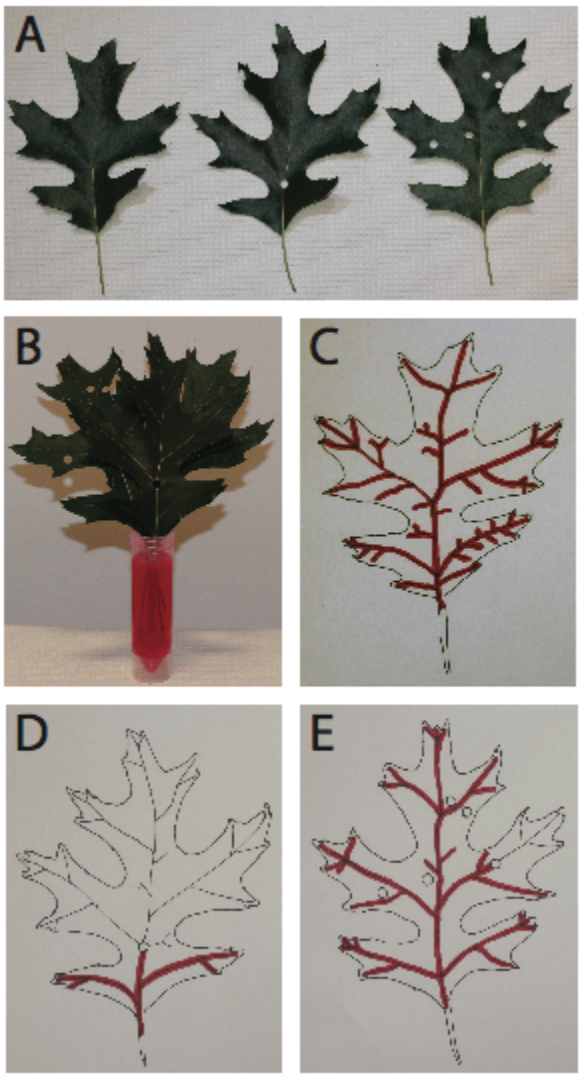

Figure 7.4. Leaf damage and dye flow predictions. (A) left: leaf without injury; center: leaf with an injury in a main vein; right: leaf with multiple injuries. (B) Leaves soaking in Rhodamine B solution. (C) Example prediction of dye flow in the control leaf (without injury). (D) Typical student prediction of flow distribution in a leaf with an injury in a main vein. (E) Typical student prediction of flow distribution in a leaf with multiple injuries.

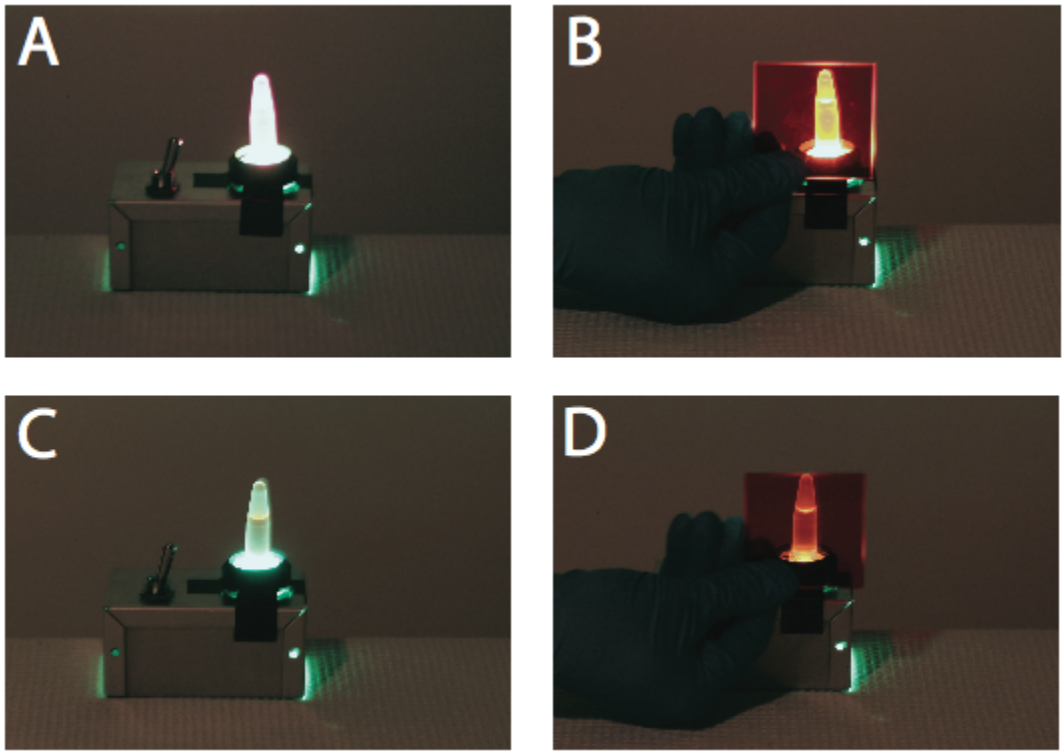

Figure 7.5. Fluorescent versus non-fluorescent dyes. (A) Rhodamine B sample on top of the green light source. (B) Orange emission from Rhodamine B solution viewed through the orange glass filter. (C) Red food coloring sample on top of the green light source. (D) Lack of emission from red food coloring sample viewed through the orange glass filter.

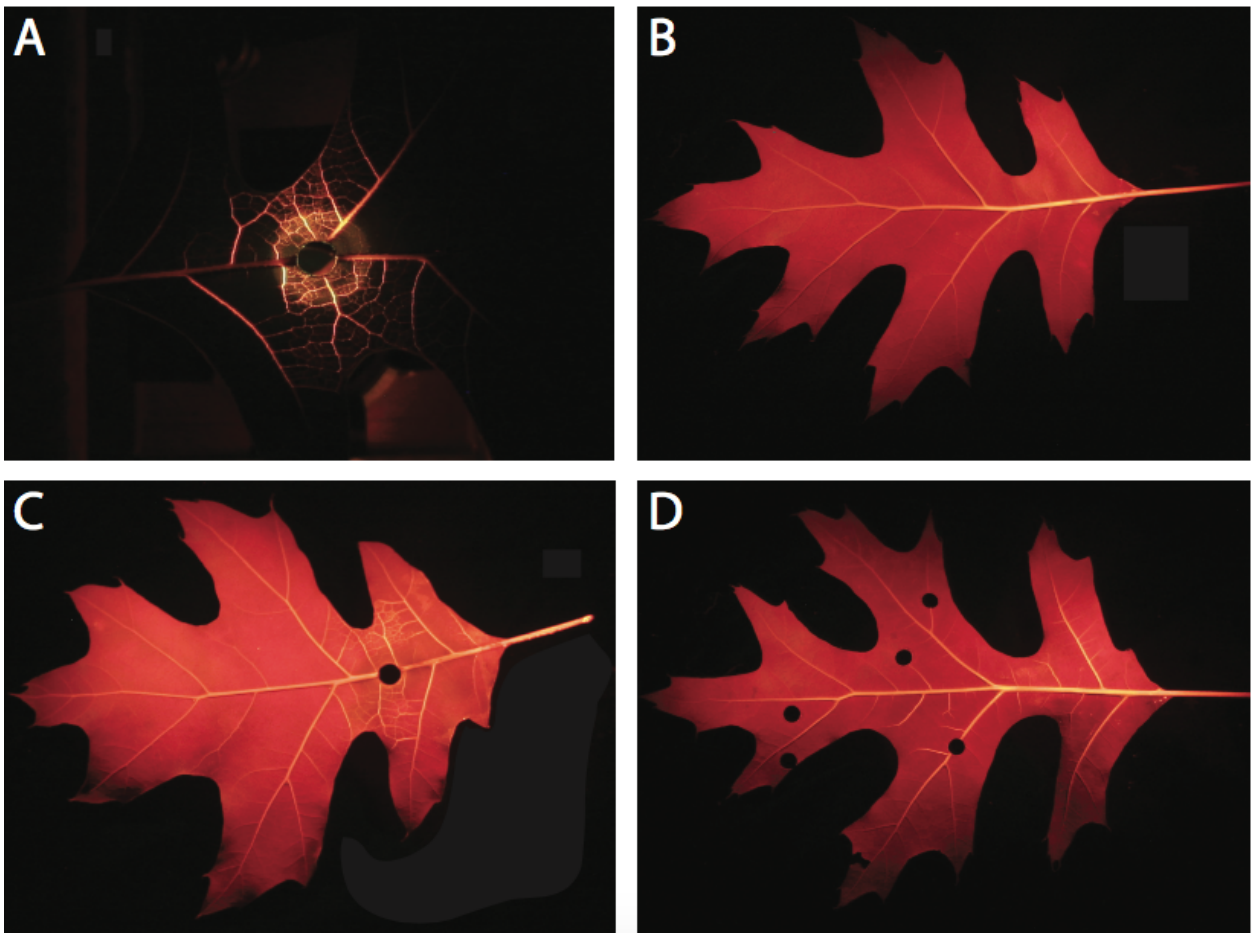

Figure 7.6. Visualization of Rhodamine B dye transport in the vein network of oak leaves. (A) Close-up view of the small veins near a hole in a main vein of a leaf. Distribution of Rhodamine B in a (B) control leaf, (C) leaf with an injury on the main vein, and (D) leaf with multiple injuries in various locations in the leaf.

7.19 ONLINE SUPPLEMENTAL MATERIAL

7.19.1 *Suppliers and cost information*

Dyes

- 25g of Rhodamine B (Cat# R6626-25G, Sigma-Aldrich) will cost approximately $20 and should last for more than five years in the freezer (the product is light sensitive).
- Food coloring (Cat# 5465 Red-Red; Amazon) will cost approximately $10 and can be kept on the shelf for many years.

Accessories

- 50 mL tubes (Cat# C001-50pk, Scientific Equipment of Houston) will cost $7 for a rack of 25 tubes.
- 30 mL tubes (Cat# 05-556-3, Fisher Scientific) will cost $56 for a bulk of 1000 tubes, but smaller bulk size could be obtained via Amazon.
- 1.5 mL tubes (Cat# L293251, Laboratory product sales) will cost $36 for a bag of 1000 tubes.

LED Light Box Components and Supplies

- Green LED (Cat#: RL5-G13008, Super Bright LEDs Inc.) will cost $0.74 each.
- Green LED Filters (Cat#: FES0550, Thorlabs) will cost $74.50 each.
- Switch (Cat#: 360-1896-ND, DigiKey) will cost approximately $5 each.
- 9V battery snap connector (Cat#: 36-232-ND, DigiKey) will cost $0.60 each.
- Enclosure “boxes” (Cat#: L101-ND, DigiKey) will cost approximately $6 each

- Grommet (Cat#: 4946A1, McMaster-Carr) will cost approximately $6 for a pack of 25 grommets. 0.5 inch hole in the enclosure, this holds the LED in place.
- 220 Ω resistors, 1 per light box (Cat#: 2711313, local Radio Shack) will cost $0.74 for a pack of 5.
- 9 V batteries, 1 per light box (Cat #: 2302211, local Radio Shack) will cost $7.69 for a pack of 2.
- Soldering iron, solder (Cat#: USAE1-VTDS010AH, Amazon) will cost $15.99
- 590nm long-pass color filter, Orange (Cat#: FGL590S, Thorlabs) will cost $71.50 each.

7.19.2 Materials per student group (max 5 students/group)

- 1 conical tube (30 mL) containing 25 mL Rhodamine-B dye (2%)
- 2 1.5-mL centrifuge tubes
    - One containing water with red food coloring
    - One containing Rhodamine-B dye
- 1 pair of scissors
- 1 hole punch
- Sheets of white paper
- Black and red markers
- 10 Oak leaves
- Orange glass filter
- LED light source box

7.19.3 Procedure:

1. Distribute all items listed above to each workstation.
2. Provide background on leaf networks.
3. Disrupt the vascular network of the leaves using the hole punch. Keep at least one leaf without holes as a control.
4. Use scissors to cut the leaf stem at an angle, keep at least two inches of the stem intact.
5. Place the leaf stems into the falcon tube with Rhodamine-B.
6. Let the leaves soak in the dye for at least 30 minutes.
7. While leaves are soaking, trace the outline of the leaves and their main veins onto sheets of paper. Sketch where holes were made.
8. Predict what will happen to the dye flowing through the leaf vessels, based on where the holes were made for each leaf, and mark this on the leaf drawings.
9. Write down hypothesis.
10. Explore the concept of fluorescence using food color and the Rhodamine-B dye vials.
11. Use the green light source and orange filter to see dye in the leaf veins for both the damaged and control leaves.
12. Compare the flow distribution from the leaves with injuries vs the control leaf, and compare with the hypotheses made beforehand.
13. Have students describe why the dye went around the holes.
14. Relate findings to the concept of redundancy and other redundant networks.

7.19.4 *Materials and teacher preparation*

An inventory of materials used for experiments are shown in Figure 7.7. For first time preparation, prepare the dye dilutions. It is recommended that a large stock solution be prepared and small amounts (aliquots) be removed from the stock for student activity use. For the Rhodamine B, dissolve 1 mg in 50 mL of water. Aliquot approximately 1.25 mL into the small centrifuge tubes and seal tightly. For a non-fluorescent control, dilute red and yellow food coloring into 50 mL of water until it's approximately the same color as the Rhodamine B. Aliquot approximately 1.25 mL into small centrifuge tubes and seal tightly. Keep the Rhodamine B aliquots in a dark location for long term storage, as it is light sensitive.

LED sources may be bought or built according to the schematic in Figure 7.8. To build the light sources, solder one end of the resistor to the positive end of the 9V battery clip (the red wire). Solder the other end of the resistor to the positive side of the LED (the longer wire lead). Solder the short wire lead of the LED to one of the switch contacts, and the other switch contact to the negative end of the 9V battery clip (the black wire). Drill two holes in the aluminum enclosure: one 0.5" hole to fit the grommet and LED through and another for the switch. Attach the 9V battery, test the circuit, and seal the aluminum box to prevent tampering. Tape the mounted green filter over the LED, limiting the amount of yellow light the LED emits so the students can clearly visualize the Rhodamine B fluorescence.

Before each time the activity is implemented, pick approximately ten oak leaves per

student group. Other leaf types are suitable, but test dye absorption before implementing the activity. Try to pick leaves that have minimal damage and have a healthy, dark green color distribution. Ensure the stems are at least two inches long. Leaves can be picked the day before and their stems submerged in water to keep them alive. Set up all supplies on separate tables, one set per team. Try and maintain group sizes between three and five students.

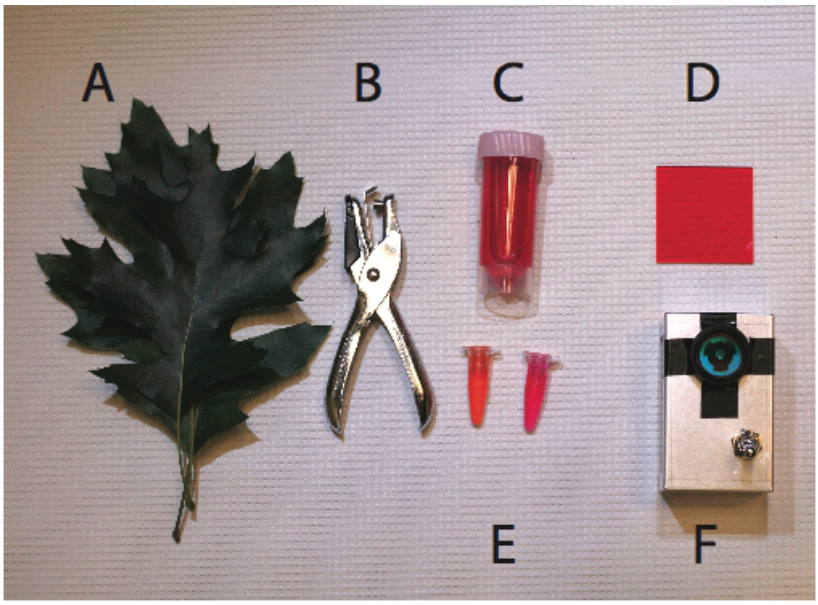

Figure 7.7. Layout of the material used for labeled the capillary network on oak leaves. (A) A set of ~6 oak leaves. (B) Hole punch. (C) 30 mL tubes with 25 mL of 2% Rhodamine B. (D) 590 nm long-pass filter (E) 2 (1.5 mL) tubes with Rhodamine B and food coloring, respectively. (F) Green colored light source.

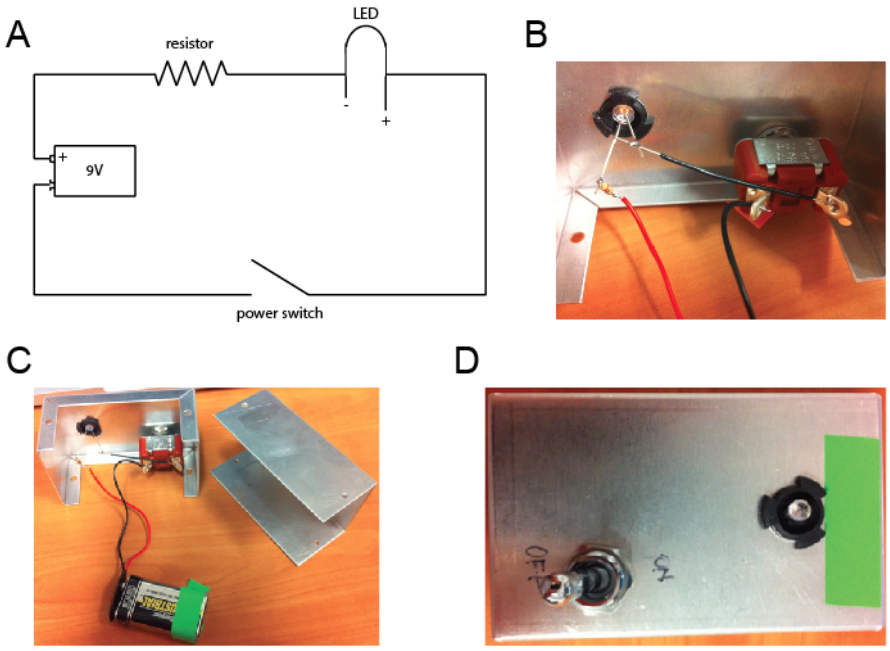

Figure 7.8. Layout of the LED circuit and construction. (A) Circuit diagram of the LED light source. (B) Assembly and connections between the LED and resistor. (C) Full enclosure and components of the LED power supply (D) LED power supply.

The following rubric can be used to assess students during each part of the activity. The term "expectations" here refers to the content, process and attitudinal goals for this activity. Evidence for understanding may be in the form of oral as well as written communication, both with the teacher as well as observed communication with other students. Specifics are listed in the table below.

1= exceeds expectations

2= meets expectations consistently

3= meets expectations occasionally

4= not meeting expectations

	Engage	Explore	Explain	Expand
1	Student demonstrates interest in the assignment and helps other group members to craft theories as to the aspects of imaging they will observe.	Student demonstrates interest in the experimentation, taking careful notes on the laboratory worksheet and completing the related calculations. Student was engaged with partners in conducting the measurements.	Student helps describe different effects in the optics module that were witnessed and proposes hypotheses on why various effects occurred.	Student is actively involved in summarizing the observations from the project. Student will ask questions about what they saw. Student will propose applications where various imaging systems can be used.
2	Student participates in filling out the objectives of the laboratory and making assumptions to the imaging they will observe.	Student shows interest in the laboratory, writes down findings on the laboratory worksheet, and conducts the experiments and calculations with partners.	Student participates in discussion of the effects that were witnessed.	Student participates in summarizing the project observations. Student discusses the imaging systems and their applications.
3	Student participates in the group discussion	Student demonstrates little interest in the	Student participates in discussion with	Student participates in the class discussion with little to no

	with little interest. Little effort is put into the answers for the objectives of the assignment.	experimentation. Measurements and calculations may be written down but without care. Student will assist partners but with little interest.	little to no interest.	interest. Answers from the student are simple direction observations with no thought behind them.
4	Student does not participate in the group discussion, and little to no effort is put into filling out the laboratory objectives.	Student shows no interest in the laboratory. Student fills in little to no information on the laboratory worksheet and does not assist with the experiments.	Student does not participate in the discussion.	Student does not participate in the class discussion.

References

1. Katifori, E., Szöllősi, G. J., and Magnasco, M. O. Damage and Fluctuations Induce Loops in Optimal Transport Networks. Phys. Rev. Lett. **104**. 2010.

CHAPTER 8

CONCLUSION AND FUTURE DIRECTIONS

8.1 Conclusion

The circulatory system and the neurovascular unit are crucial component for the function and homeostasis of the brain. While many neurodegenerative diseases have several "remarkable" pathological aspects such as amyloid plaques found in AD and proteinaceous inclusion “Lewy bodies” in the neurons of Parkinson and dementia patients, recent evidence suggests that these neurodegenerative disorders may all share a common pathology, namely vascular dysfunction. Obstructed microcirculation due to a loss or alteration of vascular cells, molecular changes within the vascular cells of the neurovascular unit, and/or environmental and genetic factors that may predispose individuals to cerebral vascular abnormalities may be subjacent causes of many neurological disorders.

Classically a "neuro-centric" view has suggested that the cause of AD must be something erratic with the neuronal network of the brain. However, this view fails to consider that the other essential cells of the neurovascular unit and the circulatory system are also involved during pathogenesis or maybe in the initiation of AD and other neurodegenerative diseases. Here we provide some of the first evidence that alteration of the circulatory system and the cerebral vasculature can indeed contribute to the symptoms of neurodegenerative diseases. Additionally, we have shown that cellular changes

specifically within brain vascular cells (leukocytes) may potentiate and/or initiate processes that exacerbate the progression of AD.

We demonstrated that cellular changes in the circulatory system and in the brain vascular network preceded the classical hallmarks of AD. This new mechanism maybe able to explain the hypoperfusion seen patients with AD and could bring new insight for new targets to ameliorate the progression of the disease.

I hope that the increasing number of studies focusing on neurovascular dysfunction will bridge the fields of neuroscience and vascular biology to further identify the specific roles of the cerebral vasculature components in maintaining a healthy central nervous system. Furthermore, research aiming to identify novel mechanisms to restore neurovascular dysfunction may have profound implications in the way patients get treated in the future for so many devastating neurodegenerative diseases, such as Alzheimer's.

8.2 Future directions

Although the findings reported here provide strong evidence for the functional significance of stalled neutrophils on brain hypoperfusion in AD, a number of important questions still remain open. Treatments with α-Ly6G significantly reduce the numbers of neutrophils stalls and improve cortical blood flow and cognitive performance (short-term and spatial memory) in APP/PS1 mice. However, similar improvements were not observed in tests for motor coordination or depression-like behavior other important

symptoms of patients with AD. As previously discussed the absence of a change in performance of these tests is likely the result of the short treatment period or suboptimal dosing in this study. Additional studies using different doses as well as a longer treatment period will be needed to assess the optimal dose needed to improve both rapid and constant effect during the desire time frame.

Based on the nature and mechanism of action of α-Ly6G (mouse only and depletion), it will be necessary to screen for new drugs (antibodies and/or small molecules) that interfere with neutrophil activation and/or adhesion to the endothelium without causing their depletion. Additional studies are necessary to fully characterize the biochemical pathways that trigger these cascade events. Directly blocking leukocyte adhesion in patients would likely lead to a number of unacceptable side effects, so our work to identify potential upstream pathways that cause the vascular inflammation that likely modulates these stalling will help to identify more viable therapeutic targets that could move forward to pre-clinical studies and trials in the future. One of the putative candidates is the Nox2 containing NADPH oxidase pathway responsible for the production of vascular reactive oxygen species (ROS). One of several Nox isoforms, Nox2 is found in neurons, neutrophils, and, interestingly, in brain endothelial cells, and is a major source of ROS in the brain endothelium. In transgenic AD mice, Nox2 knockout rescued Aβ associated dysfunction in neurovascular coupling [1]. In human AD patients, Nox2 is activated in brain vessels relative to healthy subjects [2]. There is also evidence that statins reduce AD risk, perhaps by a pleiotropic inhibition of Nox2 [3]. Tacking these findings in consideration we can assume that the inflammation triggered by the ROS,

might increase the binding receptors in the endothelium making this capillary segments more susceptible to stalling formation. Once the entire biochemical cascade has been elucidated and new drugs identified, additional studies will focus on changes in amyloid deposition or other effects on disease progression when these stalls are eliminated over time.

Finally, these findings reported here have potentially broader implications for other disorders and diseases that involve vascular dysfunction independent of the underlying mechanism of dysfunction. Preliminary experiments in our lab have shown that mouse models of Alzheimer's disease also have an increased level of stalls indicating that this could be a common feature shared between neurodegenerative diseases. These findings may provide an analog for similar conditions in humans such as Alzheimer's, vascular dementia, Parkinson's among others.

References

1. Park L., Zhou J., Zhou P., Pistick R., El Jamal S., Younkin L., Pierce J., Arreguin A., Anrather J., Younkin S.G., Carlson G.A., McEwen B.S., & Iadecola C. (2013). Innate immunity receptor CD36 promotes cerebral amyloid angiopathy. Proceedings of the National Academy of Sciences of the United States of America, 110, 3089–3094.

2. Montezano A. C., and Touyz R. M.. 2014. Reactive oxygen species, vascular Noxs, and hypertension: focus on translational and clinical research. Antioxid. Redox Signal. 20:164–182.

3. Shepardson NE, Shankar GM, Selkoe DJ. Cholesterol level and statin use in Alzheimer disease: II. Review of human trials and recommendations. Arch Neurol. 2011;68(11):1385–92. doi: 10.1001/archneurol.2011.242.